Utrecht University

MCC Materials Chemistry and Catalysis

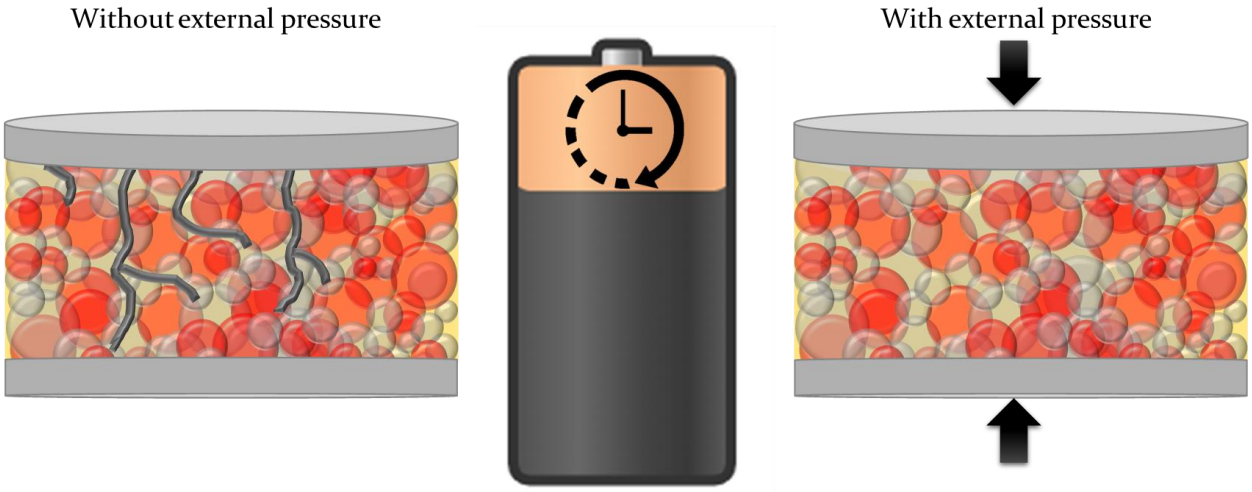

Effect of the (stack) pressure on the mechanical and electrochemical properties of solid-state electrolytes

Using complex hydride-oxide nanoparticle composite

Robert John Wolterbeek | Master thesis | 28 februari 2023

Master thesis

Utrecht University, Debye Institute for Nanomaterials Science, Material Chemistry and Catalysis group

Thesis Author: R.J. Wolterbeek, r.j.wolterbeek@students.uu.nl

Academic supervisors: Dr. Valerio Gulino, v.gulino@uu.nl

Dr. Peter Ngene, P.Ngene@uu.nl

Prof. Dr. Petra de Jongh, P.E.deJongh@uu.nl

Internship period: 07-06-2022 until 28-02-2023
Publish date: 28-02-2023

Version: 2

Abstract

The demand for batteries is significantly increasing due to the energy transition. All-solid-state batteries (ASSBs) are seen as a highly promising alternative to traditional batteries. ASSBs can use lithium metal (3862 mAh g^{-1}) as the anode, compared to the commonly used liquid Li-ion batteries that use graphite (372 mAh g^{-1}) as the anode, resulting in a much higher energy density. Additionally, ASSBs utilize solid-state electrolytes (SSEs), which eliminates the flammable liquid electrolytes and provides a safer battery. The main challenges for ASSBs are the low ion conductivity of SSEs at room temperature (values above 10^{-3} S cm^{-1} at room temperature (RT) are required) and their lack of flexibility, which can result in loss of contact with the anode after multiple charge/discharge cycles. One of the different classes of material used as SSEs are complex hydrides, with $LiBH_4$ being the most common used material. However, $LiBH_4$ has a low Li-ion conductivity of 10^{-8} S cm^{-1} at 30°C promising reports have been stated in literature to enhance this. In this study, a mixtures of $LiBH_4$ - Oxide (MgO or ZrO_2) were prepared through a mechanochemical synthesis method. This mixture was then pressed into an SSE through cold pressing. The results showed that a pore filling fraction of 80 to 100% increases the Li-ion conductivity by five orders of magnitude, which falls within the range to study ASSB cycling when applying a low currents. Furthermore, the assembly pressure during cold pressing also influenced the Li-ion conductivity with a positive trend by increasing pressure. The SSEs with Li-ion conductivity suitable for ASSB cycling were then studied using a so-called stack pressure cell. This stack pressure is an external pressure that forces the SSE and lithium anode to remain in contact avoiding the introduction of voids and dendrites. The results showed also that the stack pressure can be too high causing a mechanical induced short-circuit. Additionally, promising results were observed in maintaining contact during cycling of a symmetrical cell under constant current resulting in longer cycling life.

Layman Abstract

As is known, there is a transition towards renewable energy sources due to the greenhouse effect. These energy sources often have peak moments when energy is generated, causing the energy to be stored for later use. One way of storing energy is by using batteries. The expectation is that the demand for batteries will increase in the coming years, and the current method of battery production will not be able to meet this demand. A way to meet this demand is to design batteries that can store more energy. Batteries where the electrolyte (the component between the positive and negative sides) is made of a solid material instead of a liquid provide the opportunity for more energy storage. Furthermore, the batteries are also safer because the flammable liquid is removed. However, there are also problems with this type of solid electrolyte. The first problem is that they are less conductive. A promising solution for the conductivity is to mix certain solid materials to improve it. The second problem is that the electrolyte's contact with the positive and negative sides of the battery is not as good. An emerging idea is to exert external pressure on the battery to force the contact. These two problems are discussed in this thesis and show promising results.

List of abbreviations

ASR – Area-specific resistance
ASSB – All-solid-state Batteries
CPE - Constant phase element
EIS- Electrochemical Impedance spectroscopy
FLW - Finite length Warburg
FSW - Finite space Warburg
R_c – Contact resistance (Interfacial resistance)
R_{int} – interfacial resistance (Contact resistance)
RT – Room temperature
SSE – Solid-state electrolyte
XRD – X-ray diffraction

Table of Contents

1. Introduction

Globally, the demand for energy is continues growing, at the same time greenhouse gas emissions must be reduced. One way to partly solve this is to replace fossil fuels with renewable energy sources. However, this poses the problem that renewable energy has an intermittent production of energy, so it needs to be stored. Mechanical (compressed-air), chemical (hydrogen storage), and electrochemical (batteries) energy storage are different ways of storing renewable energy.[1]

Electrochemical systems have received a lot of attention in recent years as promising systems capable of storing energy efficiently. In the year 2018, the demand for batteries increased by 30% to 184 GWh compared to 2010. The World Economic Forum expects the demand for batteries to grow by a factor of 19 to 3562 GWh between the year 2018 and 2030. Besides the huge costs involved in this transition, geopolitical and capacity issues also play a role in the energy crisis. With the growing demand for batteries, more raw materials such as cobalt, lithium, nickel, and manganese also need to be obtained. 70% of today's mined cobalt originates from the Democratic Republic of the Congo. [2] With the expected growth and capacity of mines in the Democratic Republic of the Congo, there will already be a shortage of cobalt by the year 2025.[3]

To make global energy capacity less dependent on limited raw materials and respond to rapid growth, improving energy capacity in batteries is a way forward. Lithium-ion batteries have been the first step in the search of improving the energy storage. Although lead-acid batteries with an energy density between 20 and 40 $Whkg^{-1}$ still dominate the market, LIBs can have an energy density up to 250 $Whkg^{-1}$.[4]

1.1 Li-ion batteries

The reaction in a lithium-ion battery is based on the transfer of Li^+ between the cathode and anode. A typical cathode is a layered transition metal oxide, and the anode consists of graphite. The electrodes are separated with an electrolyte that inhibits the transfer of electrons and allows the transfer of ions such as Li^+. An insulator separator prevents the system from an electrical short-circuit, a schematic illustration of a lithium-ion battery is displayed in **figure 1**.[5]

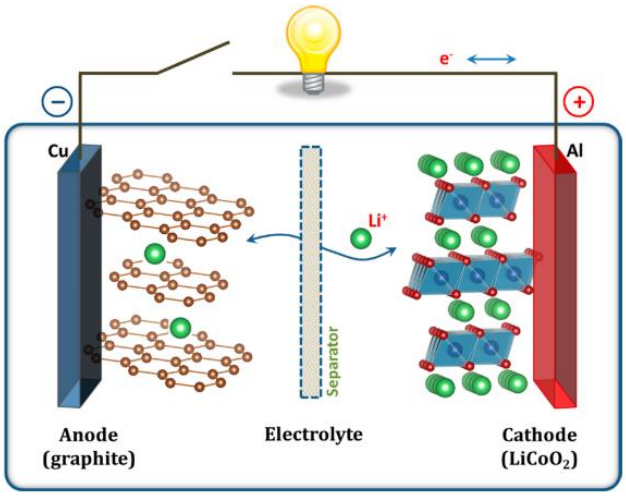

Figure 1. *Schematic illustration of a Li-ion battery (graphite| electrolyte | $LiCoO_2$).Taken from Goodenough et al. (2013)[5].*

Besides the limitation of cobalt, lithium, or other raw materials may occur, there also is a safety aspect with the batteries. Today's electrolytes typically consist of flammable organic solvents containing dissolved lithium salts.[6] This can cause problems in applications where batteries need to be fast charged. Research to optimise safety is therefore a hot topic, by making the electrolyte more thermally stable and less prone to decomposition, the risk of flammability can be resolved. A possible solution to this issue is the use of Solid-State Electrolytes (SSE). SSE may overcome the safety issue, due to the intrinsic not flammable nature of the solids used.

In addition, the use of a SSE makes it possible to replace the graphite anode with metallic lithium. Graphite possesses a lower theoretical specific capacity (372 mAh g^{-1}) with respect to lithium metal (3862 mAh g^{-1}).[7] This results in a substantial increase in the energy density, which can drastically reduce the mass and volume of a battery and still deliver the same amount of energy as depicted in **figure 2**.[8]

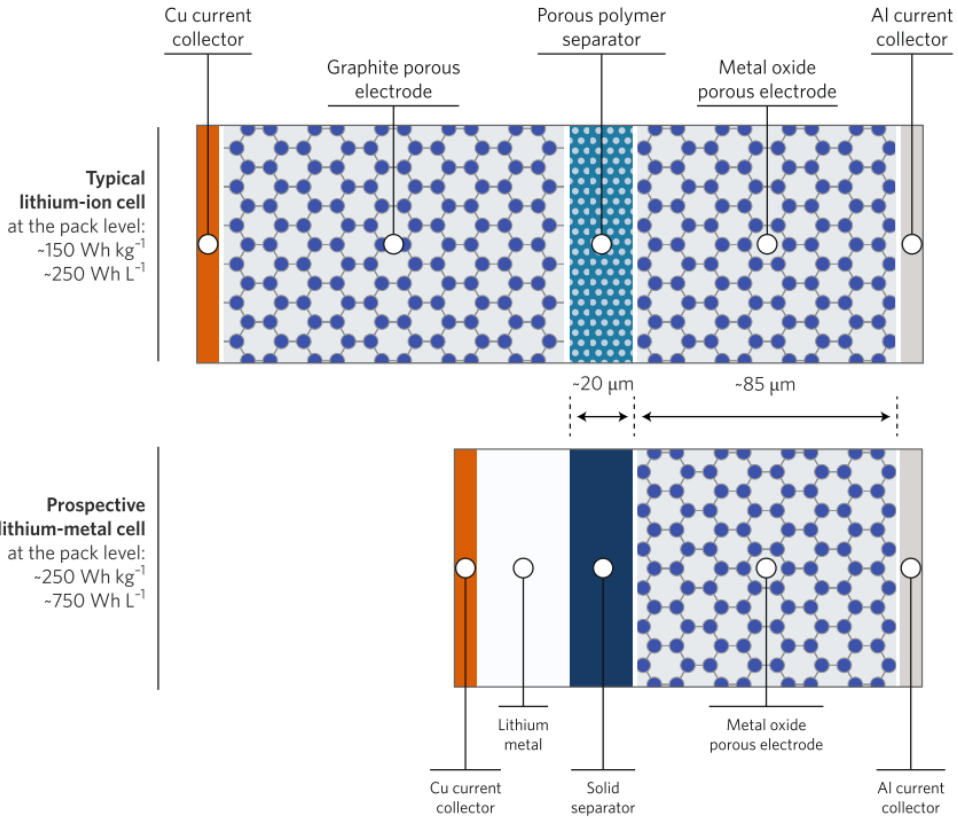

Figure 2. *(Top) A typical Li-ion cell and (bottom) a concept of a lithium metal cell, containing a Solid separator and a lithium metal electrode. The layer thickness of the graphite electrode and Lithium metal electrode are illustrated in scale possessing the same energy capacity. Here the reduction in volume and mass associated with replacing the graphite electrode with lithium metal is evident. Taken form Albertus et al. (2017)*[8].

When lithium metal is used as an anode, two main barriers occur. One barrier is the low coulombic efficiency, which can be compensated by adding excess lithium. The second problem is the nonuniform plating and stripping of the lithium at the anode. This causes porosity in the lithium anode and growth of lithium dendrites (needle-like structures).

These dendrites can penetration the electrolyte and separator, causing a short-circuit. This short-circuit would then cause a rapid failure of the battery, resulting in a possible safety hazard when using a flammable organic electrolyte.[6,7]

The use of a SSE seems to be the ideals candidate to increase safety and energy capacity simultaneously. Stable cycling of lithium metal does have requirements such as high coulombic efficiency, a low and stable resistance, and the capability to supress lithium dendrites formation within the system.[8]

1.2 Solid-state electrolytes

SSEs consist of six main groups, all with different properties as shown in **Figure 3**.[9] As described earlier, there are certain requirements when working with lithium metal as an electrode. The main required properties are: [9,10]

- Low ionic area-specific resistance
- High electronic area-specific resistance
- Wide electrochemical stability window
- Good chemical compatibility
- High thermal stability
- Stable mechanical properties
- High ionic selectivity
- Low electronic conductivity to prevent battery self-discharge (lower than 10^{-7} S cm^{-1}),
- High ionic conductivity (10^{-3} S cm^{-1} at RT).
- Low processing costs
- Easy device integration
- Environmental friendly

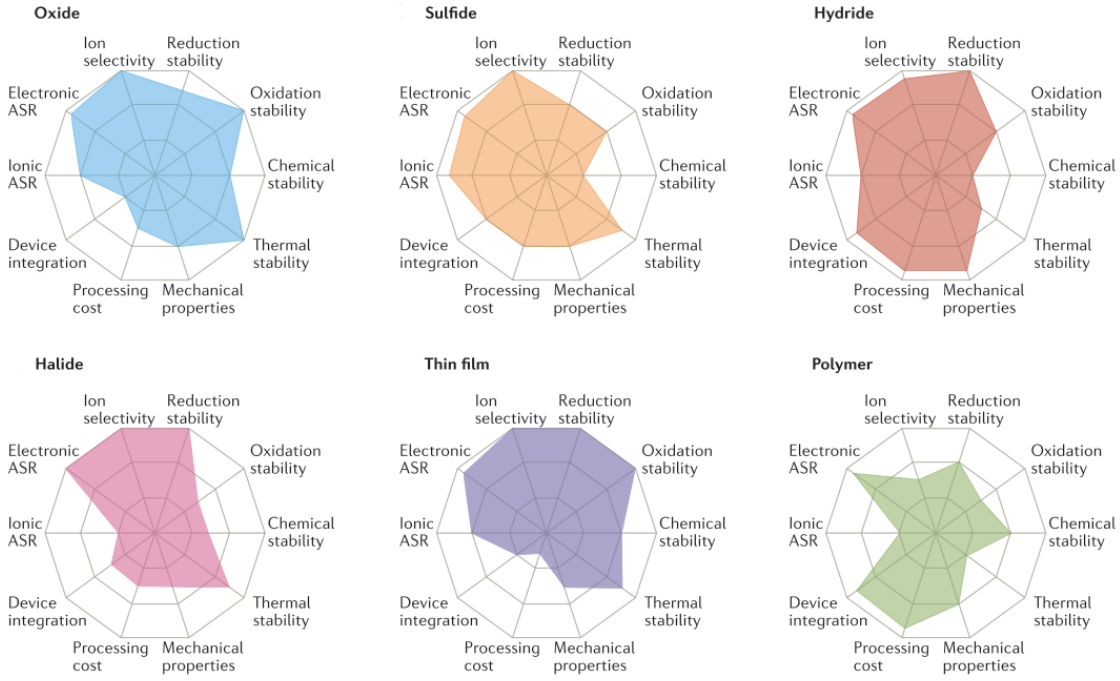

***Figure 3**. Performance of different solid electrolyte materials. ASR, area-specific resistance. Taken from Manthiram et al. (2017)[9].*

Among these six groups, the Oxides, Sulfides, and polymers are receiving a lot of attention to be used as SSEs in All-solid-state battery (ASSB).[10]

Oxides have high chemical and electrochemical stability, high mechanical strength, and high electrochemical oxidation voltage as advantages. However, they possess the properties of non-flexible and being expensive in large-scale production. In addition, the overall ionic conductivity is between 10^{-5} and 10^{-3} S cm^{-1} which still needs to be enhanced.

Sulfides have high ionic conductivity, good mechanical strength and mechanical flexibility, and low grain-boundary resistance. Yet they have low oxidation stability, are sensitive to moisture, and have poor compatibility with cathode materials.

Polymers are stabile with lithium metal, flexible, can easily produce a large-area membrane, and have a low share modulus. But have a low oxidation voltage and are not thermally stabile at higher temperature, and its ionic conductivity is low at room temperature (RT).[9,10]

This thesis will investigate complex hydrides as they have promising properties to serve as electrolytes in next-generation batteries. Besides the fact that complex hydrides have the advantage of low grain boundary resistance, stability with lithium metal, and good mechanical strength and mechanical flexibility. Whereas the disadvantages are sensitivity to moisture and poor compatibility with cathode materials.[9] Recent studies have shown that ionic conductivity can be significantly enhanced, when a mechanochemical treatment is applied or an additive is mixed with the complex hydride.[11] A common complex hydride used as SSE is Lithium borohydride ($LiBH_4$). $LiBH_4$ has the potential to be a candidate in ASSB as it is a lightweight compound and thus positively affects the energy density of the whole system. [11,12]

1.3 Lithium borohydride ($LiBH_4$)

$LiBH_4$, as described earlier, is a lightweight material (0.666 g/cm^3 at 25 °C) and is in the solid phase as a white powder. At low temperature, it has an orthorhombic symmetry (Pnma). Tetrahedral BH_4^- anion are aligned along two orthogonal directions. As the temperature increases, the structure undergoes a first-order transition into a hexagonal structure ($P6_3mc$), this polymorphic transition occurs above 110 ± 2°C. **Figure 4a** illustrates these different crystal structures of $LiBH_4$.The melting point of $LiBH_4$ is at 278 ± 5°C.[13,14]

In the study by **Matsuo et al. (2007)**[15], a relationship was observed between the ionic conductivity and the phase transition that takes place. **Figure 4b** shows this significant increase in ionic conductivity during the phase change. Where the orthorhombic structure has a Li-ion conductivity of only 10^{-8} S cm^{-1} at 30°C, the hexagonal structure achieves a Li-ion conductivity above 10^{-3} S cm^{-1} at 120°C.

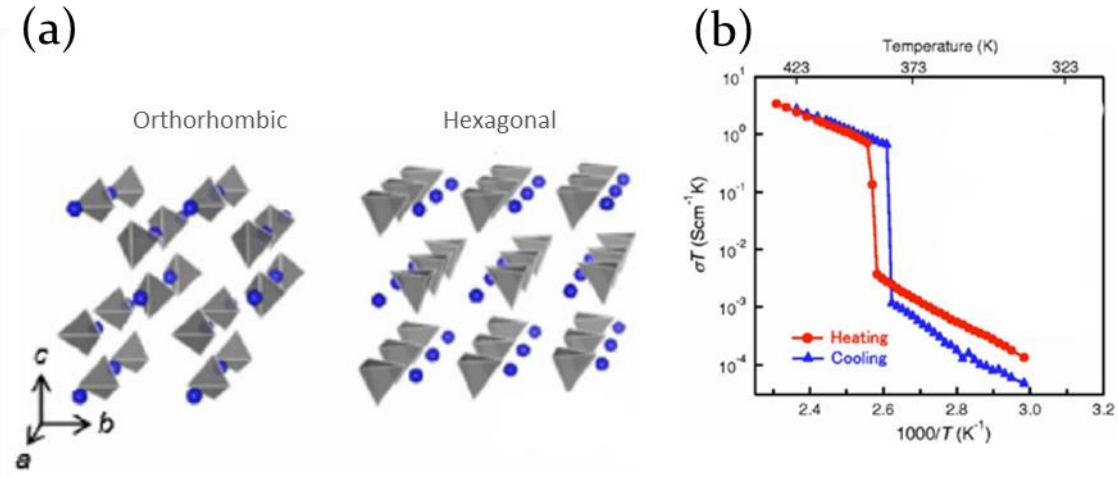

Figure 4. *(a) Crystal structures of $LiBH_4$ in (Left) orthorhombic and (right) hexagonal symmetry. The Blue spheres represent Li^+ and grey tetrahedrons BH_4^-. (B) Temperature dependence of the Li-ion conductivity of $LiBH_4$. Where red correspond to the heating ramp and blue tot de cooling ramp. Taken from Matsuo et al. (2007)*[15].

The enhanced Li-ion conductivity in the hexagonal structure is due to the stacking of Li atoms on B atoms and vice versa. This creates a metastable interstitial site centred among the three Li atoms and three BH_4 groups in the a-b plane and a connection path between two Li^+ sites in the a-c direction. This allows Li atoms to diffuse through the connection paths in three directions.[16] Another positive effect that increases conductivity is the higher frequency of rotational jumps of the BH_4^- anions in the hexagonal structure. The rotational freedom of BH_4^- is enhancing the Li-ion conductivity.[17]

However, the phase transition of $LiBH_4$ to the hexagonal structure occurs at elevated temperatures and at RT it has the orthorhombic structure with low ionic conductivity and does not meet the requirements of an ASSB. As previously discussed, there are studies that demonstrate increasing ionic conductivity at RT. Substitution of BH_4^- anions with complex anions or halides can either promote the formation of new compounds or stabilising the hexagonal structure.[18,19] **de Kort et al. (2022)**[20], explored the impact of $LiBF_4$ addition on the ionic transport in $LiBH_4$. After the synthesis, the $LiBH_4$-$LiBF_4$ sample contained amorphous lithium *closo*-borate and LiF, increasing the ionic conductivity over two orders of magnitude.

Blanchard et al (2015)[21], the addition of mesoporous SiO_2 (MCM-41) with $LiBH_4$ was studied and high ionic conductivities up to 0.1 S cm^{-1} at RT were reached. To explain the increased conductivity, the presence of two $LiBH_4$ fractions in the pores were used as a model. The first fraction was located in the centre of the pores, and when heated like bulk $LiBH_4$, a phase transition takes place (bulk fraction). The second fraction was associated with the significant increase of conductivity at RT. This fraction of $LiBH_4$ showed no phase transition, which was claimed to be caused by the interface between the $LiBH_4$ and SiO_2 pore walls and a high conductive pathway was maintained.[21] In other studies, ball-milling (mechanochemical treatment) $LiBH_4$ was performed and had a positive effect on

the conductivity but shows a decrease upon temperature cycling, as illustrated in **figure 5a.** Mixing oxides to this process increases the conductivity even more.[11,22–24] Besides mixing Oxides with $LiBH_4$ not only influences the conductivity, it also provides better thermal stability upon heating cycles.[11]

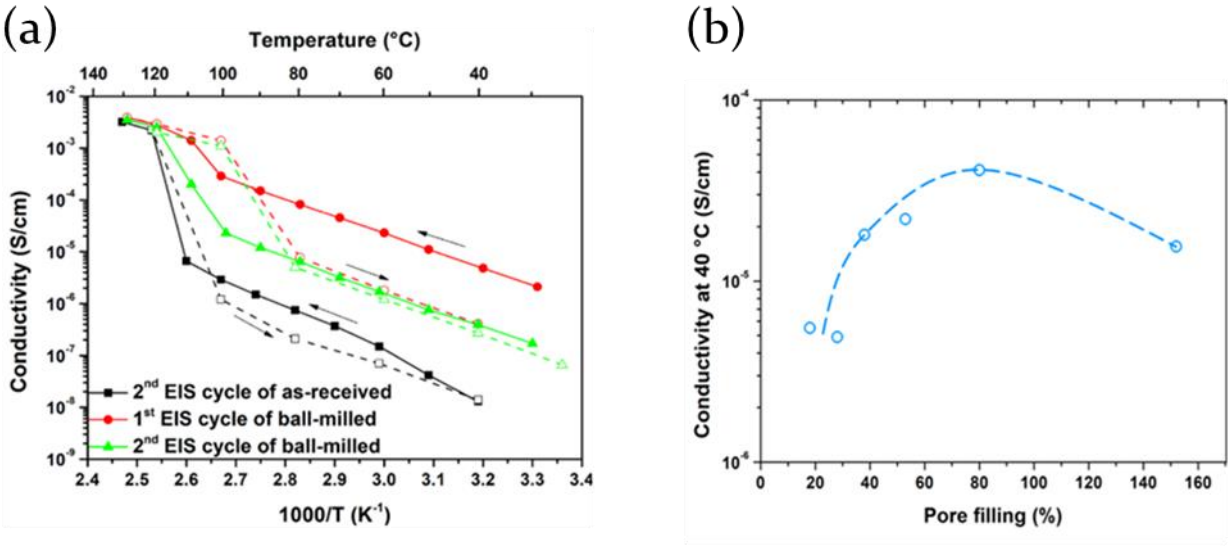

Figure 5. *(a) Li-ion conductivity of $LiBH_4$ as-received (black squares), and ball-milled $LiBH_4$ first cycle (red circles), and second cycle (green triangles). Closed symbols and lines correspond to heating, while open symbols and dashed lines correspond the cooling. (b) Li-ion conductivity of $LiBH_4$-SiO2 at 40 °C as function of the pore filling. Dashed lines are a guide for the eyes. Taken from Gulino et al. (2020)[11].*

Gulino et al. (2020)[11], reported the effect of different nanosized oxides, SiO_2, CaO, MgO, γ-Al_2O_3, TiO_2, and ZrO_2, to $LiBH_4$ by ball-milling at RT. In all cases the conductivity was enhanced where ZrO_2 and MgO increased even with 4 orders in magnitude at 40°C. All these nanosized oxides had a 25 v/v% oxide ratio to $LiBH_4$, except SiO_2. For SiO_2 different v/v% were investigated for SiO_2, and a correlation was found between the conductivity and fraction of pores filled of the oxide. The pore filling was calculated dividing the $LiBH_4$ occupied volume per gram of SiO_2 by the pore volume. By plotting the conductivity as a function of pore filling, it was observed that a pore filling of ~80% possesses the highest conductivity, as shown in **figure 5b.**

Gulino et al (2021)[24], investigated, fast ionic conductors in the solid state, based on the $LiBH_4$-MgO system. Here the pore filling approach was confirmed and shows that a similar trend occurs when working with MgO, reaching the highest conductivity (2.86×10^{-4} S cm^{-1} at 20°C) with a pore filling of 100%. The contribution of the $LiBH_4$ bulk fraction on the conductivity at higher temperatures is present. The sample with a pore filling of 323% possesses $LiBH_4$ bulk fraction, when the temperature increases, an enhanced contribution to the conductivity was observed. This is due the phase transition to the hexagonal structure that possesses a higher conductive properties as described earlier. The sample with 38% pore filling is lacking $LiBH_4$ which results in bulk fractions of MgO, these bulk fractions of MgO (oxides in general) act as an insulator and yields in significantly lower conductivity compared to the 100% and 323% pore filled samples that do not possess these MgO bulk fraction, as shown in **figure 6**.

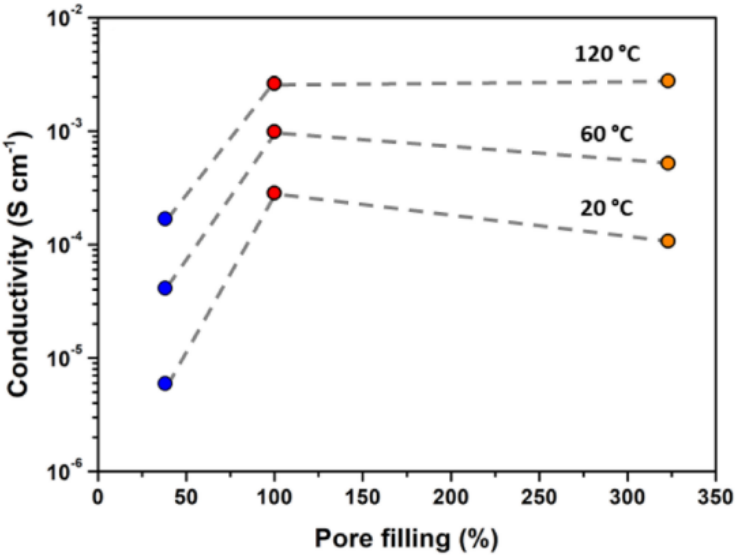

Figure 6. *Li-ion conductivity of $LiBH_4$-MgO at 20, 60, and 120 °C as function of the pore filling. Dashed lines are a guide for the eyes. Taken from Gulino et al. (2021)* [24]**.**

Several studies have shown that the Li-ion conductivity can be enhanced. The interface between the various compounds in the SSE play a significant role for this enhancement. Using the SSE in an ASSB creates two new interfaces with the SSE, at the cathode and anode. As mentioned earlier, $LiBH_4$ has poor compatibility with cathode materials.[9] TiS2 or sulphur are often used as cathode material in ASSB with $LiBH_4$. The working potential of both cathode materials is about 2 V vs Li^+/Li, which is around the oxidative limit of $LiBH_4$.[25,26]

At the anode, the continuous process of stripping and plating takes place. This process is of critical significance for the safety, high-energy density, and long lifespan of next-generation batteries. To prevent the formation of voids or dendrites, It has been reported that then interface between the SSE and lithium metal play a crucial role.[27] Understanding the stripping and plating process is importance to achieve long lifespan with next-generation batteries.[28–30]

1.4 Lithium metal Anode

There are two main issues that occur when using a lithium metal as an electrode in combination with an SSE. The first is the formation of dendrites that penetrate the SSE, causing a short circuit. The dendrites formation can be linked to the plating process (charging). The second problem occurs at the stripping process (discharge), Here contact loss occurs due to the formation of voids at the interface of the SSE and lithium metal.[31,32]

During stripping, the formation of voids will appear when the stripping current removes Li faster than it is replenished ($J_{Li\ diffusion} + J_{Li\ creep} < J_{Li+\ migration}$, where J is the flux). The amount of Li transported to the interface depends on the diffusion of Li within the lithium metal and lithium metal creep.[33,29] When the replenishment of Li to the interface of the lithium metal with the SSE is not faster than the current removing the Li, voids occur. By repeating the stripping process while constantly charging and discharging the

system, the void formation will increase significantly. The formation of these voids gives contact loss between the SSE and lithium metal, leading to increased polarisation.

Plating of Li at the interface with the SSE needs an equal supply of Li^+ ions and electrons. During plating, deposition of Li mainly takes place at two sites. The first site is the interface where there is contact between the lithium metal (electrode) and the SSE. The second site is where Li can grow unhindered; this point is introduced by voids. The formation of voids creates a so-called triple point, this is the point where lithium metal, SSE, and void come into contact resulting in a higher local current density. The increased current density at this point causes the Li to grow on the surface of the void and SSE, creating porous structures in the lithium metal. At the same time, the higher local current density induces faster growth of Li at that point, causing the Li to grow into the SSE (formation of dendrites). The dendrites formed will grow every plating round resulting in cell failure. A schematic example of the stripping and plating process is shown in **Figure 7.** During subsequent stripping, these voids are exposed at the SSE surface creating triple points resulting in nonuniform Li plating causing a rapid increase in polarisation.[30]

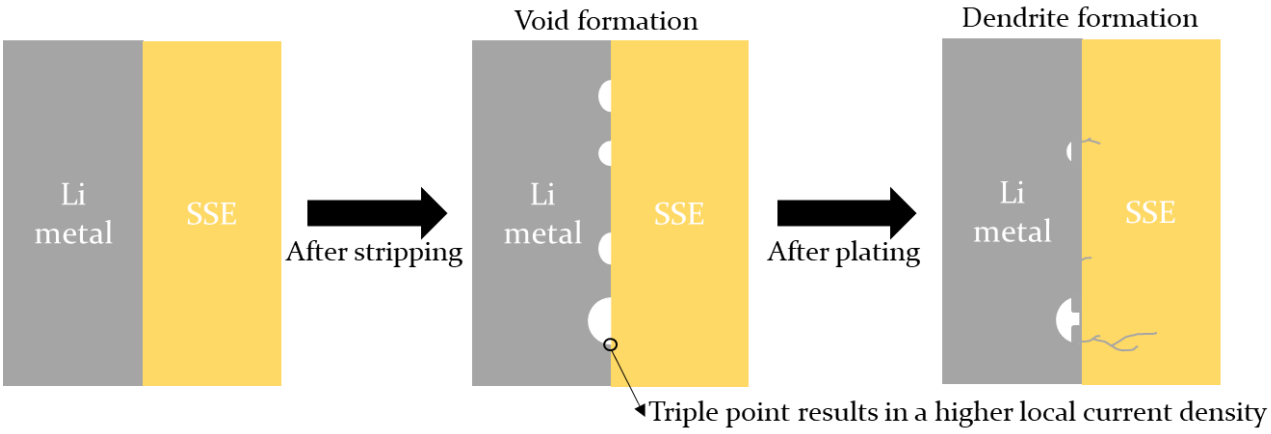

Figure 7. *Schematic of Lithium metal | SSE interface during stripping and plating. Stripping initiates voids introducing triple points. Triple points contain higher current density being a favourable deposition spot for Li.*

Kasemchainan et al (2019)[30], demonstrates that for both stripping and plating there is a specific critical current density above which dendrite formation and short-circuiting will occur. As more cycles of discharging and charging take place, the polarisation will increase as not all voids formed during stripping are removed up on plating. The accumulation of voids causes large differences in local plating current density duo to poor electrode SSE contact resulting in dendrites. This shows both critical current for stripping and critical current for plating, can play a role in dendrite formation. When the current density is above the critical current for stripping, it indicates that Li is stripped faster than it is plated. Therefore, when the current density is above the critical current for stripping, an increasing loss between the SSE and lithium metal will take place, leading to increasing local current density for the same overall current density. Due to this increased

local current density, the critical current for plating will be too high at certain location in the interface, causing dendrite formation.

One way of preventing the formation of voids and dendrites and maintaining constant contact between Li metal and SSE is to apply an external pressure (stack pressure) to the ASSB. Here the electrode and SSE are pressed against each other forcing contact, suppressing the formation of voids and dendrites. **Jow et al (1983)**[34], reported that an external pressure had a profound effect on the interface. However, only recently stack pressure has gained more attention for its importance during cycling behaviour among ASSBs.[35]

1.5 Stack pressure

Void formation is identified by several studies as a problem for cell polarisation, leading to cell failure.[27,30,36–38] **Lewis et al (2021)**[38], used X-ray tomography and contact area mapping of the interface to visualise contact loss and void formation. Here, it is confirmed that contact loss is a consequence of void formation during the stripping process and is the main cause of cell failures due to dendrites formation.

Koshikawa et al. (2019)[37], investigated the effect of plating and stripping on the so-called interfacial resistance (R_{int}). R_{int} (also called contact resistance (R_c)) is a quantity that can be associated with the gain or loss in contact area between the lithium metal and SSE when the current density remains the same. Here they found that R_c increases during stripping and decreases during plating, but over multiple cycles a gradual increase was observed, which indicates that Li stripping is responsible for an increased R_c through void formation.

Stack pressure can improve and maintain constant contact by suppressing the formation of voids. The yield strength of Li is 0.8 MPa, when exceeding this pressure, the Li surface can reform, increasing the contact area between the SSE and lithium metal, i.e. decreasing the R_c. This prevents the inhomogeneous current distribution during cycling, decreasing the formation of dendrites during plating.[39] Another great advantages of introducing stack pressure to the system is the increased self-diffusion rate of the Li metal.

Krauskopf et al. (2019)[27], discusses a kinetic model about the interface of the lithium metal and SSE, in which the influence of stack pressure is also presented. Each Li^+ ion that dissolves from the lithium metal to the SSE during the stripping process results in a vacant site formation. These vacancies can either diffuse from the interface or annihilate at a site of repeatable growth. The article identifies the diffusion of Li towards vacant sites at the interface as the main limiting factor. **Figure 8** shows a schematic, displaying difference mechanisms for a better understanding of the dynamic behaviour during the stripping process of the lithium metal. Three mechanisms are discussed at the interface, each with a different effect on R_c.

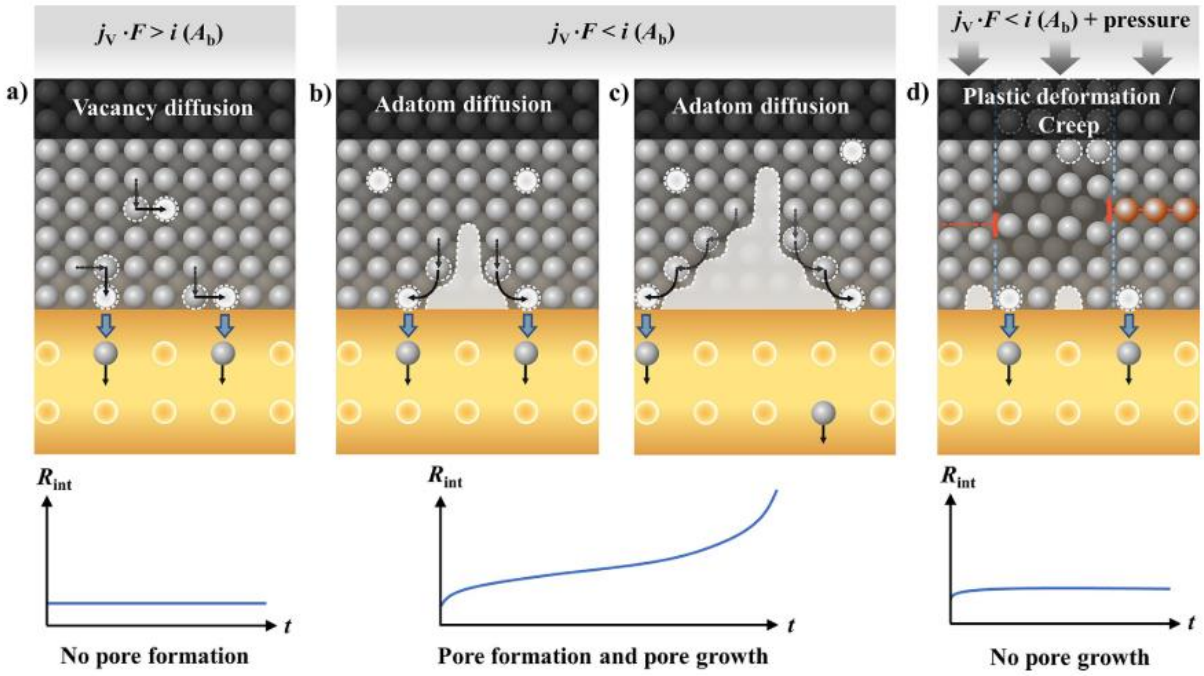

Figure 8. *Schematic of the different mechanisms at the lithium metal anode under anodic load: (a) if the local current density does not exceed the vacancy diffusion limit in the. (b,c) If the externally applied local current density exceeds the diffusion. (d) If external pressure is applied, pores will be annihilated because of plastic deformation of the lithium metal and contact loss is restricted. Taken from Krauskopf et al. (2019)[27].*

Figure 8a shows that the applied current density ($i(A_b)$) is not higher than the vacancy diffusion (J_v). This means the vacancy diffusion can keep up with the number of Li being dissolved into the SSE, keeping the interface stable resulting in no change of the contact area and a constant R_c. **Figure 8b** shows that the applied current density is higher than the vacancy diffusion, resulting in contact loss. According to the terrace-ledge-kink model for diffusion, the Li adatoms where there is no contact with the SSE will be dominate the diffusion process duo to lower activation energy. Which results in more contact loss in that area as shown in **Figure 8c**. The contact loss results in an increase of R_c. When the applied current density is greater than the vacancy diffusion and a high enough stack pressure is applied to the system, the pressure will compensate the limiting factor as shown in **Figure 8d**. Plastic deformation and Li creep will be introduced to the system, which will suppress contact loss and give a stable R_c. Making it possible to overcome the limiting factor and so, higher current densities can be introduced and simultaneously achieving longer lifespan in ASSBs.

Wang et al. (2019)[36], uses a symmetrical cell (lithium on both sides of the SSE) and applies different current densities during cycling. Starting with a stack pressure of 3.2 MPa during cycling, every 5 hours the stack pressure is decreased with 0.4 MPa. Here it was observed that when going below a certain stack pressure, a polarisation in the cell takes place in terms of a significant voltage increase. This point is called the critical stack pressure, and when applying higher current density also a higher critical stack pressure was observed to prevent cell polarisation.

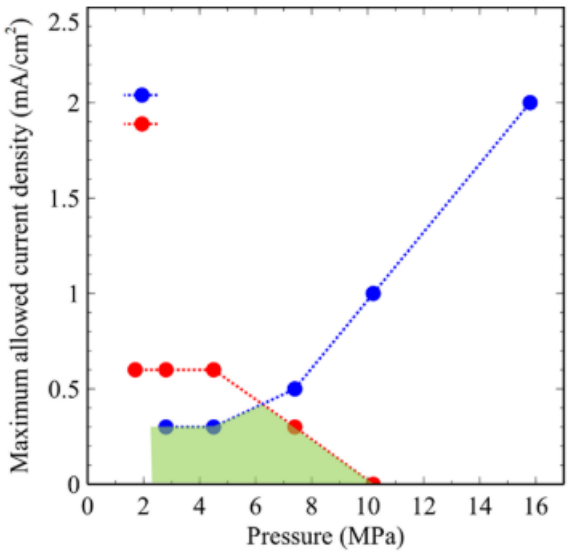

Figure 9. *Maximum allowed current density as a function of external pressure on a symmetric cell with LPSBI Solid-state electrolyte.Taken from Wang et al. (2020)[40].*

Wang et al. (2020)[40], describes that the plating and stripping process react differently with a change in stack pressure. As shown in **Figure 9**, during the stripping process, the critical current for stripping can be increased with increasing stack pressure. This is in line with what was discussed earlier, where the contact loss is suppressed and R_c remains constant. In the plating process, a negative effect takes place at the critical current for plating with increasing stack pressure. This leads to inhomogeneous deposition of Li at the interface resulting in dendrite formation and volume expansion. The volume expansion can affect the internal pressure of the system by increasing it, resulting in even higher rates of inhomogeneous deposition. A different stack pressure during plating and stripping is therefore ideal but not feasible. A balance like the green area in **Figure 9** must be found to obtain the longest cycling life with ASSBs.

Doux et al. (2020)[39], studied the shorting behaviour of a symmetric cell with constant current and stack pressure during cycling. Besides that, too high stack pressure has a bad influence on the Critical current for plating as discussed above. The article discusses that too high stack pressure makes the creeping of Li through the SSE possible. **Figure 10** shows that too high stack pressure of 75 MPa can result in a mechanical short duo to immediately creep of Li through the SSE, leading to more direct cell failure. It is therefore expected that creep through the SSE will occur at stack pressures above the yield strength of lithium. The lithium that then penetrates the SSE will be a preferential site of plating resulting in cell-shorting.

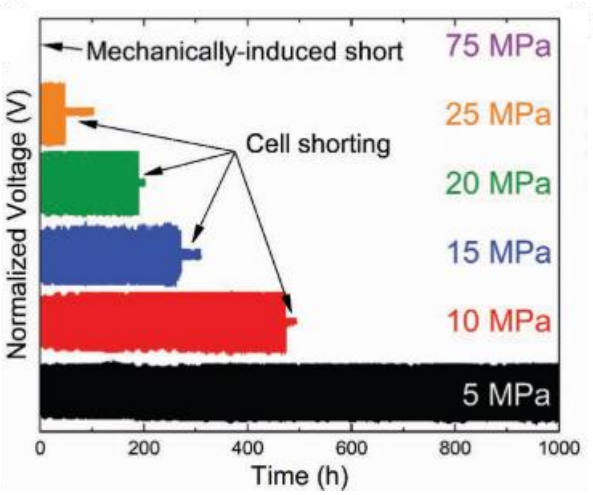

Figure 10. *Normalized voltage of Li symmetric cells as a function of time during plating and stripping at different stack pressures. At 75 MPa, the cell already mechanically shorts before cycling begins. At 5 MPa, no short was observed for over 1000 h. Taken from Doux et al. (2020)[39].*

It is therefore important to study the mechanical properties of the SSE. **Barai et al. (2017)**[41], concludes that a high shear modules and yield strength can reduce the formation of dendrites. In **Doux et al. (2020)**[42], the assembly pressure applied to the SSE was varied. When using different pressures (50, 150, 250, and 370 MPa) during assembly of the SSE, the conductivity and density of the SSE increased at higher assembly pressures and therefore can play an important part within ASSBs.

1.6 Pressure effect on solids

Cold pressing can be used to obtain an SSE pellet. A (usually) powder is compressed with an assembly pressure to obtain a pellet. The pressure used to obtain the pellet varies in literature due to the use of different materials. **Sakuda et al (2013)**[43], studied the densification under high pressure of sulfide SSE. **Figure 11** shows the relationships between assembly pressure and conductivity. With Raman spectroscopy almost no change in the local environment was measured and X-ray diffraction (XRD) showed almost no changes before and after pressing. SEM images reveal that increasing the pressure increases particle size and decreases the presence of grain boundaries. This corresponds to the change in conductivity, the decrease in grain boundaries resistance has a positive effect on conductivity. **Doux et al. (2020)**[42], discusses that the effect of assembly pressure will work even better for SSE containing oxides. This duo to the higher number of grain boundaries in oxides and so, have a strong influence on the conductivity of oxides. The quantity of grain boundaries will decrease when the total surface area also decreases, by reducing porosity or increasing size of particles.

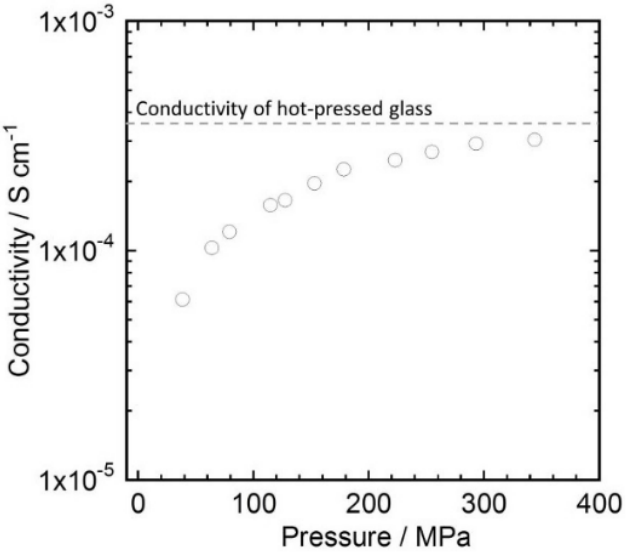

Figure 11. *Relationship between assembly pressure and ionic conductivity of $75Li_2S\ 25P_2S_5$. Dashed line indicates the conductivity of $75Li_2S\ 25P_2S_5$ bulk glass. Taken from Sakuda et al. (2013)[43].*

In this thesis, $LIBH_4$ is used in combination with an MgO or ZrO_2. In **Richard et al (2000)**[44], Investigates the decreases in porosity depending on pressure within MgO nanocrystals. Upon increasing the pressure, it has been observed that the pore size and volume can be reduced in a controlled manner. With the effect described earlier, this could a positive trend for the conductivity for the materials that will be used. **Talyzin et al (2007)**[45], Shows that $LiBH_4$ with a pressure of 0.5 to 1.4 GPa at RT undergoes the phase transition from orthorhombic structure to the hexagonal structure (as previously described the more conductive form). The combination of the reduction in grain boundaries in oxides and the more conductive hexagonal $LiBH_4$ caused by increasing pressure is a utopia for increasing the conductivity.

As shown by **Gulino et al (2021)**[24], the combination of MgO and $LiBH_4$ has a strong effect on conductivity. To amplify this effect with increasing the assembly pressure may increase it further. Combined with the correct stack pressure, this could lead to an optimal candidate for a long lifespan with an ASSB.

2. Aim of the thesis

The aim of this thesis is to gain knowledge about the influence of stack pressure on complex hydrides solid-state electrolyte performances in all-solid-state batteries. To achieve this goal, $LiBH_4$ will be combined with MgO or ZrO_2 as the solid-state electrolyte.

First, the mechanochemical treatment of $LiBH_4$ with different volume ratios of oxides (MgO and ZrO_2) were analysed with the aim of reaching Li-ion conductivity above the 10^{-3} cm^{-1} for enabling battery cycling.

Subsequently, the effect of the pressure applied during cold pressing on the Li-ion conductivity within the $LiBH_4$-oxide composites has been explored.

Using the volume ratio and assembly pressure with the highest Li-ion conductivity for a solid-state electrolyte. The electrochemical stability was studied with the addition of lithium electrodes to form a symmetric cell, here the amount of stack pressure required to induce a mechanical short-circuit was implemented. Followed by improving the interfacial contact between the lithium metal and solid-state electrolyte with stack pressure.

With the improved interfacial contact, galvanostatic stripping and plating measurements were performed, applying different stack pressures aiming to improve the cycling life of the solid-state systems at room temperature.

3. Techniques and Characterization

This chapter explains the techniques and characterisation methods used in this thesis. A brief introduction is provided after which the equipment as well as the parameters are discussed. A more detailed outline of how the experiment was prepared and implemented can be found in **Chapter 4.**

3.1 Ball-Milling

Ball-milling (mechanochemical treatment) is used for sintering composite materials and is often used in the field of chemistry to synthesize new solid-state materials such as complex hydrides. This is a process in which the alternation of stress and relaxation introduces resulting in the constant regeneration of the surface, the formation of plastic strain, crystal defects introduction, deep structural changes and amorphism. It is considered a green synthesis route as it does not use solvents. In this work, the use was made of Fritsch Pulverisette 6 planetary mill. Where the rotation plate rotates in the opposite direction compared to the jar. This rotation creates a planetary motion for the balls which gives an orbit through the centre of the jar, Which leads to sintering of composite materials.[46] Parameters such as speed of rotation, jar dimension, ball dimension, and ratio of the balls and precursors are of importance for the energy impact of the synthesis. In this work a ratio of 30: 1 ball: precursor was used in 80 ml tungsten carbide jar. The jar contained 30 tungsten carbide balls with a diameter of 10 mm. The jar was sealed in an Ar glovebox to maintain inert Ar atmosphere. All samples were ball-milled three times for 10 min at 300 r.p.m. with a break of 1 min each time, to minimise heating effects. The ball-milling was done in collaboration with the research group of Prof. Marcello Baricco of University of Torino.

3.2 Powder X-Ray Diffraction

Powder XRD was used as a characterisation technique to establish the prepared compounds identity or to determine decomposition after ball-milling. The XRD patterns after the synthesis of the different samples were obtained at RT (ex situ) using a Panalytical X-pert Pro MPD (Cu Kα1 = 1.54059 Å, Kα2 = 1.54446 Å) in Debye–Scherer configuration. Patterns were made from 10 to 80° 2θ range, with a time step of 160 s. Glass capillaries of 0.8 mm were used as sample holders and sealed under Ar atmosphere inside the glove box. The XRD measurements were performed in collaboration with the research group of Prof. Marcello Baricco of the University of Torino.

The possible change in identity or the decomposition after cold pressing was also measured by XRD. Different samples were cold pressed to pellet at RT with different assembly pressures. The XRD patterns were obtained at RT with the use of BRUKER 2D PHASER 2G, Lynxeye (1D mode) detector, and a TubeKFLCo2K x-ray (Co tube with 1.79026 Å). The patterns were made from 10° to 80° 2θ range with an increment of 0.043°, a time step of 1 s for a total of 1646 steps. A custom-made XRD sample holder was used and sealed under Ar atmosphere inside the glovebox.

3.3 Physisorption

Physisorption was used to calculate the specific surface area (S_{BET}) by fitting with a Brunauer-emmett-teller isotherm and subsequently deriving the total pore volume (V_p) by the absorbed volume of N2 at p/po = 0.95.1 The data was obtained by N2 adsorption at 77 K in a Micromeritics, TriStar II plus.

3.4 Potential stat

In this thesis, the AMETEK PARSTAT MC with both the PMC-1000 and PMC-200 channels were used for various electrochemical techniques such as Electrochemical impedance spectroscopy (EIS), Cyclic voltammetry, and Galvanostatic cycling to gain knowledge about the electrochemical properties of different samples. The data was provided and analysed using VERSASTUDIO (software supplied with the AMETEK PARSTAT MC). The different electrochemical measurements were performed with a two electrode custom-made cell in which the SSE pellet, symmetric cell, or battery systems were prepared, this cell was coupled to the potential stat using banana plugs. The custom-made cell houses the sample between two stainless steel current collectors, compacted into a cylindrical shape with a diameter of 10 mm. The thickness depends on the type of system, amount weighed, and the assembly pressure applied, more explanation about the costume made cell and sample preparation can be found in **chapter 4**.

In this thesis electrochemical understanding is of great importance and the techniques that were used to analyse these properties will be explained in more detail below.

Electrochemical Impedance Spectroscopy

EIS is a technique used to study the electrical behaviour of electrochemical systems, such as batteries and fuel cells. It is a powerful tool for understanding the fundamental processes taking place in these systems, such as charge transfer, mass transport and electrolyte conduction. EIS is based on the concept of impedance, which is a measure of the resistance to the flow of an electric current in a circuit. Impedance is a complex quantity, with both a real and an imaginary component. The real component, called resistance, represents the resistance to the flow of direct current, while the imaginary component, called reactance, represents the resistance to the flow of alternating current. In EIS, an alternating current is applied to the electrochemical system and the reaction of the system is measured. The reaction is a complex impedance, which can be represented as a vector in the complex plane. The size of the impedance vector is a measure of the overall opposition to the flow of current, while the phase angle of the vector is a measure of the phase shift between the applied signal and the response. One of the main advantages of EIS is that it can be used to study the different components of impedance separately. For example, the charge transfer resistance, which is related to the rate at which electrons are transferred between the electrodes and the electrolyte, can be separated from the mass transport resistance, which is related to the rate at which ions move through the electrolyte.

The Nyquist plot is a graph where the reality of the impedance is depicted on the x-axis and the imaginary component on the y-axis, a typical impedance spectrum is illustrated in **figure 12.**

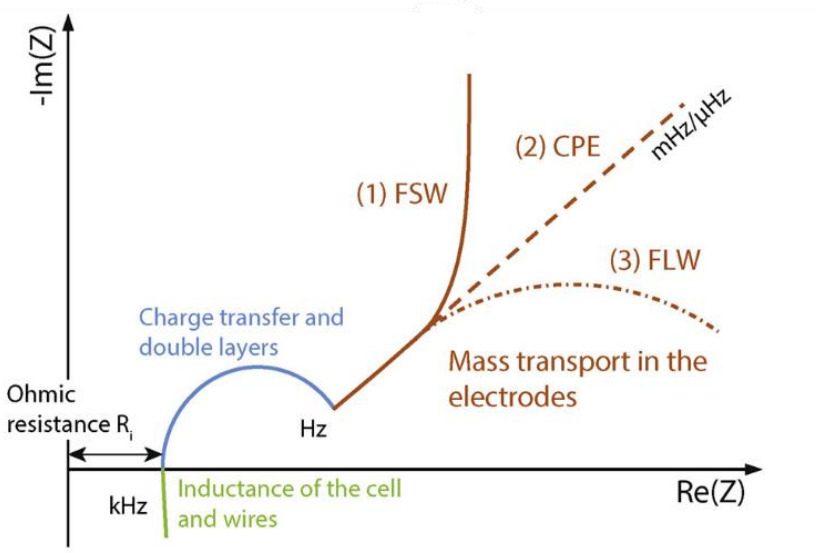

Figure 12. *Typical Impedance spectrum of a Li-ion system with four different processes. The low frequency diffusion behaviour is typically modelled by (1) a finite space Warburg (FSW): limited diffusion layer and limited electroactive substance, (2) constant phase element (CPE): semi-infinite diffusion layer, and (3) a finite length Warburg (FLW): limited diffusion layer and ideal reservoir at the boundary. Taken from Oldenburger et al. (2019)*[47].

The different components of the Nyquist plot can be interpreted as follows:

The semi-circular structures in the plot are related to the Warburg impedance, which is caused by mass transport problems in the electrolyte. The size of the semi-circle indicates the size of the mass transport problem and the position of the semi-circle on the plot indicates where the problem occurs (at the anode or cathode). This may indicate, for example, problems with the conductivity of the electrolyte or limited transport of ions to the electrodes.

The straight line running to the origin of the plot is related to the charge transfer impedance. This resistance is caused by the limited rate at which electrons can be transferred between the electrodes and the electrolyte. The stiffness of the line indicates the extent of this limitation. This may indicate a problem with the interfacial resistance between the electrode and electrolyte or a limitation of electronic conduction within the electrode.

A high frequency where the reactance (X) decreases, is related to the electronic conductivity of the electrode material. This may be an indicative of the low-quality of the electrode and the conduction of electrons within the electrode.

The intersection of the semi-circle with the straight line is the electrolyte resistance. This is the resistance created by the combination of mass transport and charge transfer.

The interpretation of the Nyquist plot is very important to understand the battery performance and identify any problems. For example, a larger Warburg impedance may indicate a problem with the conductivity of the electrolyte, while a larger charge transfer impedance may indicate a problem with the interfacial resistance between the electrode and electrolyte.

In the study of ASSB, EIS can be used to study the interface between the SSE and the electrodes. For example, it can be used to study the ionic conductivity of the solid electrolyte, the electronic conductivity of the electrodes and the interfacial resistance at the electrode-electrolyte interface. This information is crucial for understanding the performance of ASSB and for developing new materials that can improve their performance.[47–50]

The EIS measurements performed in this thesis implemented a frequency range between 1 HZ and 1 MHZ with an applied voltage of 20 mV to the system. The impedance data were analysed using VERSASTUDIO and DECIM custom-made software designed by H.P. Rodenburg, Utrecht University. Several samples and experiments were done with EIS and will be explained in detail in **chapter 4.1.**

Cyclic voltammetry

Cyclic voltammetry is a powerful technique that can be used to understand the electrochemical stability of SSE. When a SSE is subjected to a voltage sweep, it undergoes a series of electrochemical reactions that expresses the stability of the electrolyte. During the voltage sweep, the SSE can undergo different types of reactions, including oxidation and reduction reactions. Oxidation reactions take place at the positive potential limitation of the voltage sweep, where electrons are removed from the SSE. Reduction reactions take place at the negative potential limitation, where electrons are added to the SSE. The stability of a SSE can be determined by analysing the peak current and peak potential of the oxidation and reduction reactions. For a stable SSE, the peak current and peak potential should remain constant during multiple voltage sweeps. In contrast, if the peak current or peak potential varies significantly, this may indicate that the solid-state electrolyte is not stable and may degrade over time. In addition, the stability of SSE can be determined by analysing the voltammogram shape and its symmetry. A symmetric voltammogram indicates good stability and reproduction of the process, while an asymmetric voltammogram indicates poor stability or poor reproducibility.[50,51]

The cyclic voltammetry measurements in this thesis were made using the addition of carbon black to the working electrode in order to increase the surface area under investigation, resulting in a better analyse of the probed reaction. In addition, the carbon black provides a better discharge of electrons towards the electrode duo to its higher electron conductive (compared to the SSE used in this thesis).[52] The pellets obtained (SSE) were tested using a lithium disk as the counter electrode and reference electrode and a stainless steel current collector as the working electrode. The measurement was performed within a voltage range of $1 < V < 5$ vs Li^+/Li at a scan rate of 100 $\mu V\ S^{-1}$. The sample preparation with carbon black, SSE, and lithium electrode are discussed in more detail in **Chapter 4.**

Galvanostatic stripping and plating of a symmetric cell.

Galvanostatic cycling is the process of applying a constant current during both the stripping and plating cycles of an electrochemical cell. In the case of a symmetric cell the SSE is placed between two alkali metal electrodes, this technique can be used to understand the stability of the electrolyte material and its interface between the electrodes during cycling. During the stripping cycle, ions are transferred from the anode to the electrolyte, while during the plating cycle, ions are transferred from the electrolyte to the cathode. By maintaining a constant current during both cycles for the same time, the amount of material that is added or removed from the electrodes can be precisely controlled. The stability of the solid electrolyte is determined by its ability to maintain its structural integrity and chemical composition over multiple cycling cycles. A stable electrolyte will show minimal changes in its electrochemical properties, such as its ionic conductivity and transference number, over time, while an unstable electrolyte will show significant changes in these properties. The Galvanostatic cycling can provide information on the ionic conductivity, the rate of degradation and the mechanical stability of the SSE. This can help to determine which materials are suitable for use and identify areas where further research is needed to improve the stability. An inconsistency between the electrolyte and electrode, such as a change in interface, will be highlighted by a change in resistance. A rising overpotential indicates growth of a resistive layer as the electrolyte breaks down into compounds that are poorly ionic but conductive. A stable potential on the other hand may indicate that there is no reaction taking place in the electrolyte or that an initial formation of a protective layer does not grow further.[24,50,53,54]

During this thesis, different orders of stack pressure were applied while measuring galvanostatic cycling of a symmetric cell. The obtained pellet (SSE) was placed between two Lithium disk, giving a symmetrical electrode configuration. A constant current of 25 µA was applied for 3600 seconds with subsequent constant current of -25 µA for 3600 seconds on the cell. An EIS was taken between each transition to obtain interface information. The application of stack pressure and preparation of the symmetric cell can be found in **Chapter 4**.

Galvanostatic cycling with potential limitations

Galvanostatic cycling with potential limitation (battery cycling) is a routine technique used to study the performance of ASSB. It involves applying a constant current to the battery while measuring the voltage response of the system as long the voltage remains within a specific range. The current is typically set at a value equal to the maximum capacity (C) of the battery divided by a factor (n), which is chosen based on the desired test duration and magnitude of the electrochemical environment for the system. by subjecting the battery to a constant current over a period of time, the battery's behaviour under different conditions such as charge and discharge rates, temperature, and cycling life can be studied. The data collected from galvanostatic cycling can be used to identify any potential issues with the battery's performance, such as degradation or loss of capacity. [24,50,53,54]

The battery cycles in this thesis were performed by using a SSE with a lithium disk as counter electrode and reference electrode and a cathode mixture (with a ratio 4:6 of cathode material: same material as the SSE) as working electrode. The constant current applied to the system was calculated using the maximum capacity C divided by a factor n=20 providing a C-rate of 0.05. The measurement was performed with a cut-off potential of $1.5 < V < 2.6$ vs Li^+/Li. The sample preparation of the SSE, cathode material and lithium electrode as well as the calculation for the maximum capacitance are discussed in more detail in **Chapter 4**.

4. Experimental section

This chapter describes the samples preparation and what materials were used during this thesis before analysing. All samples used during this thesis are reactive at ambient conditions and decompose when moisture comes into contact. All sample preparations were performed in an argon-filled glove box of MBRAUN, LABmaster dp, with a purifier maintaining O_2 and H_2O values of < 0.1 ppm. The argon used in the glove box was pure 5.5 grade argon.

4.1 Sample preparation

Synthesis SSE mixtures

First, $LiBH_4$ (purity > 95% from Alfa Aesar) as-received was ball-milled for 2 hours at 500 r.p.m, The obtained $LiBH_4$ powder ($LiBH_4$-Ball Milled) was then used as the material to mix with MgO (Steam Chemicals) and ZrO_2 (type 1: Daiichi Kikenso RC-100, Gimex ; type 2: Daiichi Kikenso DK-1 ,Gimex). The powders were then mixed as the ratios presented in **Table 1** and then dried at 300 °C in a furnace, under dynamic vacuum, for 6 hours. After drying, the powders were ball-milled as described in **chapter 3.1** and XRD measurements were obtained, the mixtures were then stored inside the glovebox. The S_{BET} and V_p of the oxides used in **table 1** were obtained by physisorption experiments according to the parameters described in **chapter 3.3**.

Table 1. *Composition of $LiBH_4$-oxide mixtures used in this thesis. The fraction of pore filled was calculated by dividing the $LiBH_4$ volume by the pore volume (V_p). The thickness of $LiBH_4$ was calculated considering the BET surface area (S_{BET}) of the oxide with the assumption it's a flat geometry.*

Name Sample	Oxide	Oxide (wt. %)	Oxide (v/v %)	S_{BET} (m^2/g)	V_p (cm^3/g)	Fraction of pore filled	Thickness of $LiBH_4$ (nm)
MgO 26	MgO	65.0	26	215	0.25	323	3,8
MgO 53	MgO	85.7	53	215	0.25	100	1.2
MgO 74	MgO	94.0	74	215	0.25	38	0.4
RC 1	ZrO_2 RC-100	72.1	23	99	0.29	200	5.9
RC 2	ZrO_2 RC-100	86.6	42	99	0.29	80	2,3
RC 3	ZrO_2 RC-100	94.5	66	99	0.29	30	0.9
RC 4	ZrO_2 RC-100	63.3	16	99	0.29	300	8.8
RC 5	ZrO_2 RC-100	83.8	37	99	0.29	100	2.9
RC 6	ZrO_2 RC-100	87.8	45	99	0.29	72	2.1
Ox 1	ZrO_2 Dk-1	74.7	25	74	0.26	196	6.9
Ox 2	ZrO_2 DK-1	94.3	65	74	0.26	35	1.2
Ox 3	ZrO_2 DK-1	89.8	50	74	0.26	66	2.3

SSE pellet Sample preparation

The SSE pellet were made by weighing into the sample holder (see **chapter 4.2 figure 13**) an amount of sample equivalent to a theoretical volume (V_t) (calculation is shown in **chapter 4.3**) between 30 and 33 mm^3. The same range of V_t was used to compare the different samples under different assembly pressures. After transferring the sample in the sample holder, the holder was placed under a hydraulic press for cold pressing. Here, an assembly pressure with a maximum of 2 tonnes (for a 10 mm diameter pellet ~250 MPa) can be reached and applied to the system to form a SSE pellet. The sample holder was then closed using the standard method as described in **chapter 4.2**.

Different assembly pressures (62, 87, 112, 137, 162, 187, 212, and 250 MPa) were applied to all samples to investigate the influence on the Li-ion conductivity by measuring EIS, densification, and compressibility by measuring the thickness and volume. From this data, it was decided to prepare the SSE pellet with an assembly pressure of 250 MPa for the further experiments.

Following up, for each sample an SSE pellet was prepared with an assembly pressure of 250 MPa and EIS measurements were performed at different temperatures. The first measurement was at RT, followed by a measurement at 40°C. At 40°C, an heating ramp was introduced increasing the temperature with 10°C between each EIS measurement until it reaches 140°C (heating cycle). At 140°C, the temperature decreased with 20°C after each EIS measurement until it reaches 40°C (cooling cycle). These cycles were repeated two times, followed by a final RT measurement (RT-[40°C-140°C-40°C]^{x3}-RT) to investigate the thermal stability of the SSE.

Symmetric cell preparation

The symmetrical cells were used for the experiments where the R_c was minimised with stack pressure, followed by a galvanostatic stripping and plating measurement under a specific stack pressure ($0 < P < 25$ MPa). To prepare a symmetrical cell, an SSE pellet was produced as described above. Then, on either side of the SSE, a 10 mm Lithium disk was attached (Li | SSE | Li), The disk was prepared using a hollow punching tool (diameter 10 mm) pressing a disk out of a Lithium ribbon (thickness x W 0.38 mm x 23 mm, 99.9% trace metal base from Aldrich). A Cu disk of 10 mm were placed between the stainless steel current collectors and the Lithium disk to ensure easy removal of the symmetrical cell from the sample holder after the experiment. The screws of the sample holder were then gently tightened and not according to the standard procedure, to insure the poor contact of the Lithium disk and SSE for the study of R_c at low pressure.

The mechanical induced-short and R_c were studied with the use of the pressure setup shown in **chapter 4.2**. EIS measurements were taken when the wanted stack pressure was applied to the sample holder. The same cell with the improved R_c was used for galvanostatic stripping and plating under a given stack pressure.

Cell Preparation for Cyclic voltammetry

Preparing a cyclic voltammetry sample, the SSE was prepared with a different approach. Instead of using 250 MPa as the assembly pressure to compress the SSE, a pressure of 125

MPa was used. Then a mixture of the same material as the SSE along with carbon black (type 1: Ketjenblack EC600JD from Akzo Nobel Chemicals; type 2: GMP-500 H2-treated from) with a ratio of 1:1 in weight was prepared by mixing it for 5 minutes in a mortar. As described earlier, this effectively increases the active area where the electrochemical reactions can take place, with an increased oxidation peak in the case of the electrolyte used. The SSE+ carbon black mixture was added in small amounts to the stainless steel working electrode side and spread evenly over the pellet surface. Once the entire SSE pellet was covered with the SSE+ carbon black mixture, the entire system was compressed under an assembly pressure of 250 MPa. A lithium disc was then added and used as counter and reference electrode. The sample holder was tightened until there was sufficient contact, shown on the potential stat by reaching a potential between 2.3 / 2.4 V vs Li^+/Li. The cell was subsequently placed in an oven with a temperature of 60°C for 20 min to improve the contact, the cyclic voltammetry measurements were then performed under RT.

Cell Preparation for battery cycling

The battery cell samples were prepared in a similar method to the cyclic voltammetry samples. The only change in the method was that the SSE+ carbon black mixture at the working electrode was replaced with a cathode material. The cathode material was prepared by a mixture of TiS_2 (purity 99.9% from Aldrich) with SSE material 4:6 ratio by weight. The amount of TiS_2 determined the C-rate what was applied to the system during the measurement, using the maximum capacity calculated according to the calculation in **chapter 4.3**. The batteries were cycled with 60°C and RT.

4.2 The Sample holder and pressure setup

Figure 13 shows a schematic of the pressure setup with sample holder attached used during this thesis. These are custom-made setups made by the workshop within Utrecht University, where all the grey parts in the picture are made of RVS 304 and the yellow parts of polyether ether ketone (PEEK).

The Sample holder (A) consists of two current collector parts (G) and a PEEK housing (H). The current collectors have a piston part of 10 mm that fit into the PEEK housing, on the pistons are two positions where O-rings can be placed to make it airtight (black rings). In this thesis, FKM O-rings (ERIKS O-ring FKM 75, 8x1 mm) were used to withstand elevated temperatures up to about 190°C. Banana plug input (F) are available at the side of the current collectors to provide excellent connection with the potential stat. The samples were placed between the current collectors. To close the sample holder, there are three screw positioned in each current collector part, with which the current

collector parts can be attached to each other securing the PEEK housing in between. The three screws are tightened with a constant force of 2.5 N/mm2 unless stated otherwise.

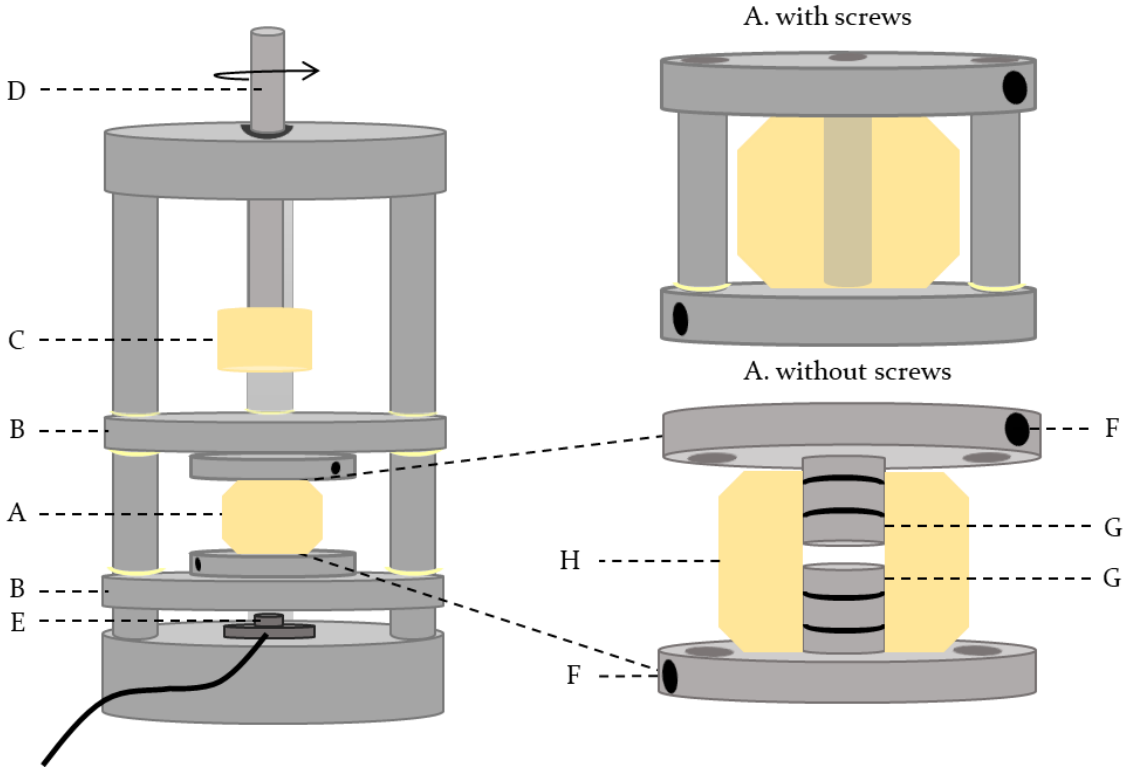

A: Custom-made cell / sample holder
B: Movable plates
C: PEEK head attached to the screw
D: Screw
E: Mechanical pressure cell reader
G: Current collectors with two O-ring spots
F: Banana plug input
H: PEEK housing for sample

F and (right) sample holder. All the grey parts are made of stainless steel 304, where the yellow parts are made of low electron conductive polyether ether ketone (PEEK).

The pressure setup consists of three main parts, the movable plates (B), the part that applies mechanical pressure (C,D), and the part that measures the pressure (E). When stack pressure is applied to the sample holder, the three screws that secure the current collectors must be removed. The sample holder was clamped between the movable plates, which are sealed off from the electrical circuit by PEEK rings. The movable plates together with the sample holder rest on the pressure cell reader, which was taken as the zero point for the stack pressure (0 MPa). A screw (D) can then be tightened until the PEEK head (C) at the end of this screw contacts the upper movable plate and exerts mechanical pressure on the sample holder. The harder the screw was tightened, the more stack pressure was exerted on the system. The pressure cell reader can measure to a maximum of 2 kN, using the calculation in **Chapter 4.3** the applied pressure was calculated into MPa.

4.3 Calculation used for sample preparation and parameter settings

This chapter presents formulae that were used to obtain certain parameter settings, sample preparations, or results presented in **chapter 5**.

Assembly pressure

The commonly used unit for Assembly pressure is MPa, the hydraulic press used during this thesis has a indicator in tons. Using the sample holders diameter the assembly pressure was converted to MPa using the formulae below.

Gravity (*g (9.81 N kg^{-1})),*weight in tons (m(1 ton = 1000 kg)), diameter of pellet *(d)*

$$\boldsymbol{m} * \boldsymbol{g} = \boldsymbol{N}$$

$$\boldsymbol{\pi} * \boldsymbol{r}^2 = \boldsymbol{mm}^2$$

$$\mathbf{1}\,\boldsymbol{MPa} = \mathbf{1}\frac{\boldsymbol{N}}{\boldsymbol{mm}^2}$$

Theoretical values (Volume, thickness, and empty space)

To calculate the Empty space, the V_t and real Volume (V_r) were used with the calculations described below. The theoretical thickness was calculated by entering V_t as V_r.

Density (*p)*, v/v%, weight (m), radius (r), thickness (t)

Theoretical volume:

$$\boldsymbol{V_t} = \frac{\boldsymbol{m}}{\boldsymbol{p}}$$

Real volume:

$$\boldsymbol{V_r} = \boldsymbol{\pi r^2 t}$$

Empty space:

$$\%\ \boldsymbol{empty\ space\ in\ SSE} = \left(\frac{\boldsymbol{V_r}}{\boldsymbol{V_t}} * \mathbf{100}\right) - \mathbf{100}$$

Mechanical pressure cell reader

The force measuring load cell is from the company ME-Meßsysteme, type KM10a 2kN. This load cell can measure pressure by applying compressive force to it. The company performed a calibration resulting in a signal of 1.78194 mv V-1 at a force of 2 kN, with a maximum signal of 2 mV V-1. The formula below was used to convert the unit to force in MPa.

Area of applied pressure (A (m^2)), 2 kN = 1.78194 mV V^{-1}, x = 2 mV V^{-1}

$$\frac{\boldsymbol{kN}}{\boldsymbol{A}} = \boldsymbol{MPa}$$

$$\frac{\left(\frac{2kN * 2\ mV\ V^{-1}}{1.78194\ mV\ V^{-1}}\right)}{A} = factor\ for\ MPa$$

Activation energy

To calculate the activation energy, the results of the temperature dependent conductivity were used according to the steps described below.

Boltzmann constant (kb), Temperature (T in kelvin), Conductivity (σ)

Plot: 1 / T (x-axis) against ln(σ,T) (y-axis) ($R^2 > 0.99$)

$$\sigma = \frac{\sigma_0}{T}\ e^{\left(\frac{-Ea}{kb\,T}\right)}$$

$$ln(\sigma, T) = ln\,\sigma_0 - \frac{1}{T}\frac{Ea}{kb}$$

$$Intercept = ln\,\sigma_0$$

$$Slope = \frac{Ea}{kb}$$

$$Ea = \frac{slope}{kb}$$

Contact resistance

The R_c (R_{int}) described in the results were calculated using the following formula.

Area of the pellet(A), Resistance of the pellet (R_{SSE}), Resistance of the pellet and interface system (R_{total})

$$R_c = \frac{R_{total} - R_{SSE}}{2} A$$

Capacity of battery

The maximum capacity was calculated by using the following formula.

Capacity of cathode material (TiS_2 = 239 mAh g^{-1})[24], weight cathode material (g)

$$C = \frac{capacity\ cahode\ material\ per\ gram\ (mAh\ g^{-1})}{weight\ cathode\ material\ (g)}$$

5. Results

This chapter discusses the results. First, the samples after the mechanochemical synthesis are characterized using XRD and N_2 physisorption, discussing which effect the addition of the oxide have on the structure. Next, all samples were processed into an SSE pellet and tested for the mechanical and electrochemical properties depends on assembly pressure and temperature. Then the optimized assembly pressure was used to prepare the SSEs for the study on the effect of stack pressure at the interface with lithium.

5.1 Sample characterization

The effect of the ball-milling synthesis method on $LiBH_4$ and the different $LiBH_4$ - oxide composites was monitored by XRD analysis at RT. **Figure 14** shows the XRD pattern of ball-milled $LiBH_4$. Showing the main diffraction pattern corresponds to the orthorhombic structure. The orthorhombic structure is retained after ball-milling as reported in literature. [11,23]

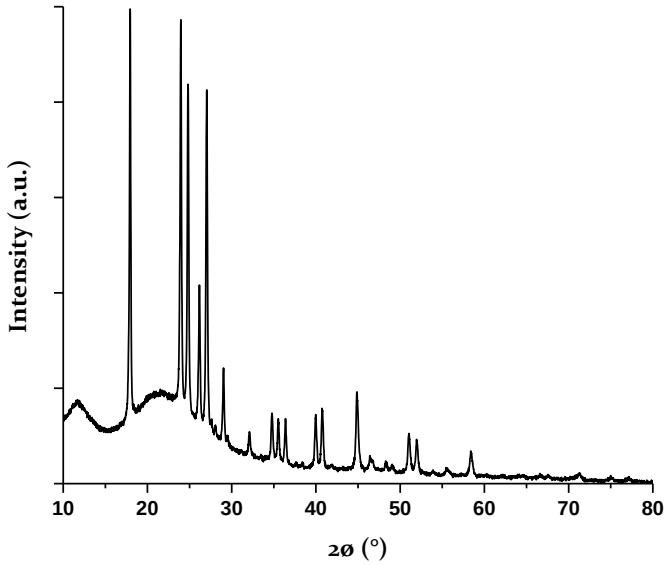

Figure 14. *XRD patterns of ball-milled $LiBH_4$*

The XRD patterns of $LiBH_4$ - ZrO_2 samples with the two different types of ZrO_2 (RC-100, DK-1) are displayed in **Figure 15**. The pattens show mainly the diffraction peaks of the ZrO_2 phase. Some of the peak of the orthorhombic $LiBH_4$ are visible for samples with a low amount of oxide. Increasing the volume of ZrO_2 in the mixture shows a decrease in intensity of the orthorhombic $LiBH_4$ phase. This can be explained by the fact that ZrO_2 overlaps the peaks of $LiBH_4$ due to the higher scattering power of the heavier atoms. No information of the highly conductive interface fraction between $LiBH_4$ and the oxide could be observed.[21] The $LiBH_4$ - MgO samples used in this thesis are the same from the

study by **Gulino et al (2021)**[24], and their XRD patterns can be found in **Figure A1 of the appendix**.

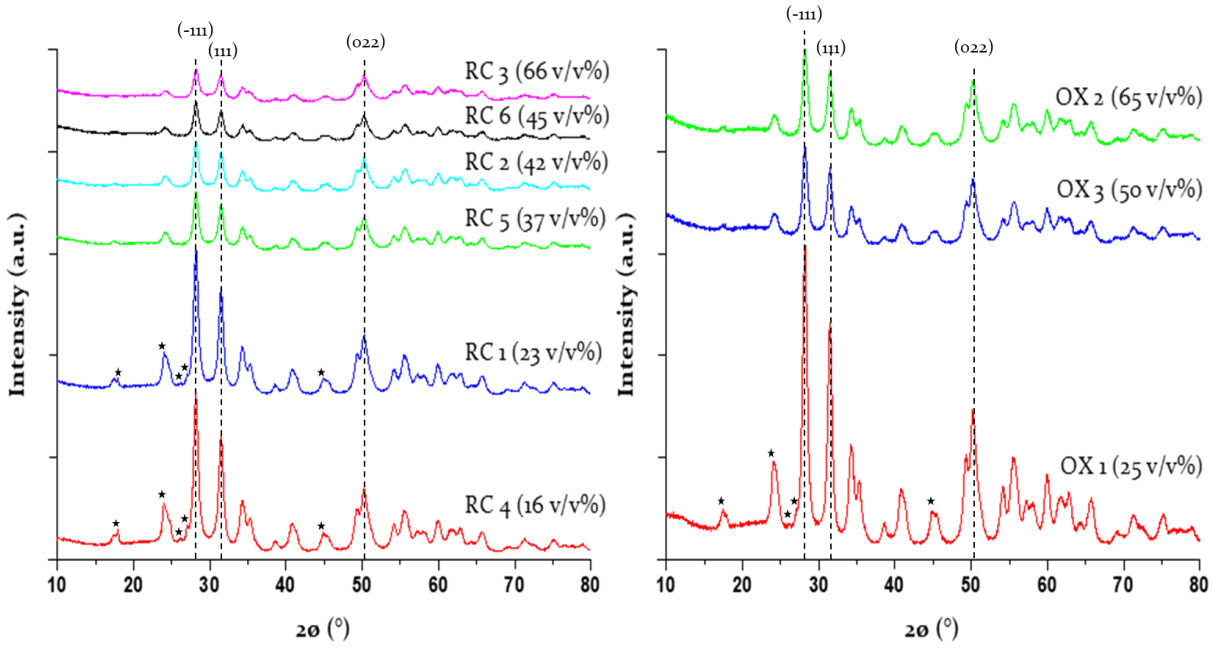

Figure 15. *XRD patterns of ball-milled $LiBH_4$-ZrO_2 samples for different v/v% ratios, with on the left RC-100 ZrO_2 samples and right DK-1 ZrO_2 samples. Dashed line indicated a specific facet of monoclinic-ZrO_2. ★ mark diffraction peak of orthorhombic $LiBH_4$.*

Besides the powder being analysed, XRD patterns were constructed of samples RC 3 (high oxide volume) and RC 4 (low oxide volume) when pressed to a pellet at different assembly pressures (63, 162, and 250 MPa). Here, no changes are observed in the diffraction patterns and the main ZrO_2 diffraction peaks are displayed, see **Figure A2 of the appendix**. This was expected since the higher intensity of the ZrO_2 diffraction pattern overlaps the $LiBH_4$ patterns. Also no changes in $LiBH_4$ structure were expected, $LiBH_4$ undergoes a phase transition at higher pressures between 0.5 and 1.4 GPa at RT as described in the introduction.[45]

To investigate the effect of different pore filling fractions of the oxide with $LiBH_4$, three different possibilities were studied using N2 physisorption.

The first possibility has a low volume of $LiBH_4$ compared to the oxide, which introduces bulk fractions of oxide into the system. This indicates that the surface of the oxide is not fully saturated with $LiBH_4$ (pf < 100%). This means oxide bulk mainly influencing the Li-ion conductivity of the system.

The second possibility is an equilibrium in the volume of $LiBH_4$ and the oxide, resulting in complete saturation of the oxide surface with no bulk fractions (pf~100%). This creates highly Li-ion conductive $LiBH_4$ - oxide interface layers. It is mentioned in literature that the highly Li-ion conductive interface layer can have a thickness of $LiBH_4$ up to 2 nm.[55,56]

The third possibility has a high volume of $LiBH_4$ compared to the oxide, which introduces bulk fractions of $LiBH_4$ into the system. This also has a full saturation of the oxide surface (pf>100%). However, the bulk fractions of $LiBH_4$ in contact with the oxide are thicker than 2 nm. Resulting in fractions showing normal Li-ion conductivity behaviour of $LiBH_4$ and suppressing the highly conductive fraction.

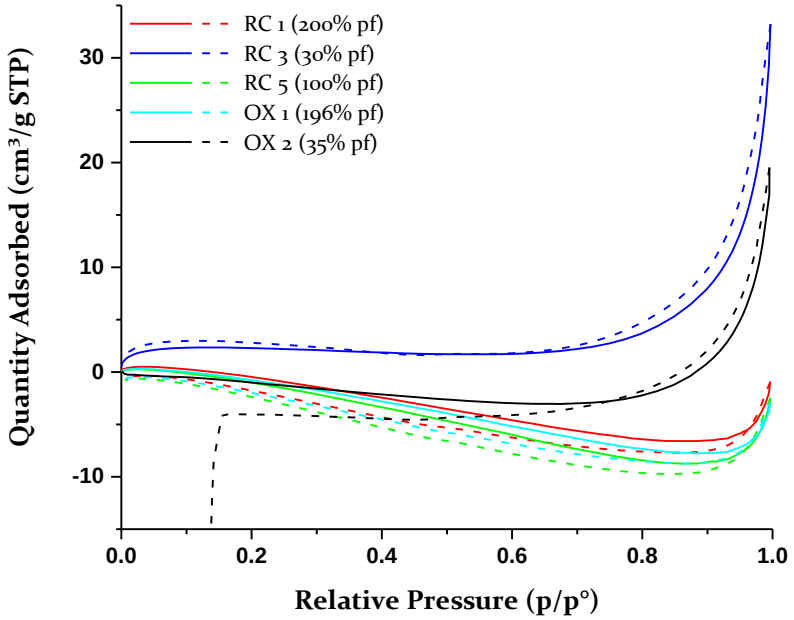

Figure 16. *N2 physisorption of $LiBH_4$ – ZrO_2 composites with pore filling of 30, 35, 100, 196, and 200%.*

Figure 16 shows the N_2 physisorption of five samples with different pore filling percentages. A negative slope is observed which is not common in a typical physisorption measurement. In a typical physisorption measurement, the sample volume is expected not to change with changing pressure. The negative slope can be linked to the compressibility of $LiBH_4$, where $LiBH_4$ shrinks when the pressure is increased and expands with decreasing pressure. What explains the trend that when the $LiBH_4$ ratio increases with increasing pore filling, the negativity of the slope increases. However, this effect appears to become constant when 100% pore filling is reached, which can be explained by the dominant presence of $LiBH_4$ (more than 60 % of the volume). From this data, nothing can be concluded with certainty for the surface area or pore volume of the different mixtures.[57–59]

5.2 Electrolyte

Pore filling

As described above, there are several studies using different approaches to increase the Li-ion conductivity of $LiBH_4$. In this thesis, the strategy described in **Blanchard et al (2015)[21],** and **Gulino et al (2020)[11]** will be used, i.e. the mixing of $LiBH_4$ with oxide, specifically via ball milling. The Arrhenius plots of the Li-ion conductivity as a function of the temperature of all the different samples synthesised in this thesis are shown in **Figure A3 in the appendix**.

To obtain the Li-ion conductivity, the Resistance of the SSE was determined by fitting the impedance data. The impedance data is displayed in a Nyquist plot and are then fitted with an electrical circuit equal to the circuit shown in **Figure 17** (electrical circuit: LR(RQ)Q). **Figure 17** shows an example of an impedance spectra of RC 5 at 40°C and 100°C displayed as a Nyquist plot. Here it is demonstrated how the data points are fitted and their values can be found in **Table 2**. With these values, the SSE resistance can be determined, and the Li-ion conductivity calculated using the formula: $\sigma = \frac{t}{AR}$

t is the thickness of the pellet, R is the resistance of the SSE, A the surface area of the pellet, and σ the Li-ion conductivity of the SSE.

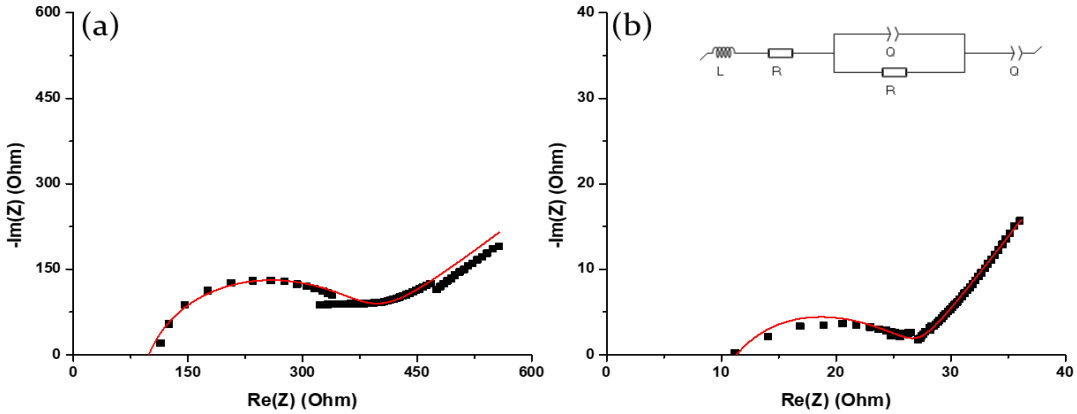

Figure 17. *Impedance spectra until 10 kHz shown on the Nyquist plot for RC 5 at (a) 40°C and (b) 100°C. The insert shows the electrical circuit LR(RQ)Q used to fit the data. The Red lines correspond to the result of the fits, Table 2 lists the parameters obtained by the fits.*

Table 2. *EIS fitted values of RC 5 at 40°C and 100°C shown in Figure 17. The equivalent circuit adopted for the fit is LR(RQ)Q.*

Temperature Measurement	L	R_1	R_2	Q_1	n_1	Q_2	n_2
40°C	4.57 e^{-06}	63.09	288.40	2.86 e^{-09}	0.92	1.72 e^{-05}	0.51
100°C	2.58 e^{-07}	1	26.30	6.37 e^{-06}	0.54	06.43 e^{-04}	0.67

The Li-ion conductivity of $LiBH_4$ as-received (8.63×10^{-9} S cm^{-1} at RT) was increased by two orders of magnitude after ball-milling (5.31×10^{-7} S cm^{-1} at RT). Adding MgO or ZrO_2 further increases the Li-ion conductivity with two till three orders of magnitude, the composites of the different oxides showing the highest Li-ion conductive are displayed in **Figure 18** together with $LiBH_4$ as-received and ball-milled. For the data points, only the first heating cycle is mentioned to keep the data well-organised. In **Figure A4 of the appendix**, all three cycles of a MgO and ZRO_2 SSE pellet are shown, showing stability during cooling and heating ramps.

The composite MgO 53 shows the highest conductivity at RT (2.36×10^{-4} S cm^{-1} at RT) which is in agreement with what is reported in litterateur (2.86×10^{-4} S cm^{-1} at 20°C).[24] This is about 5 orders of magnitude higher than the $LiBH_4$ as-received used in all samples. The highest Li-ion conductivity at RT of the different ZrO_2 composites were found in the samples RC 2 (7.72×10^{-5} S cm^{-1} at RT) and OX 3 (1.15×10^{-4} S cm^{-1} at RT). Together with the increased stability during heating and cooling and the significant increase in Li-ion conductivity, it was observed that the activation energy (Ea) was decreased when ball-milling and adding oxides. All the activation energies of the different samples prepared during this thesis are reported in **Table 3.**

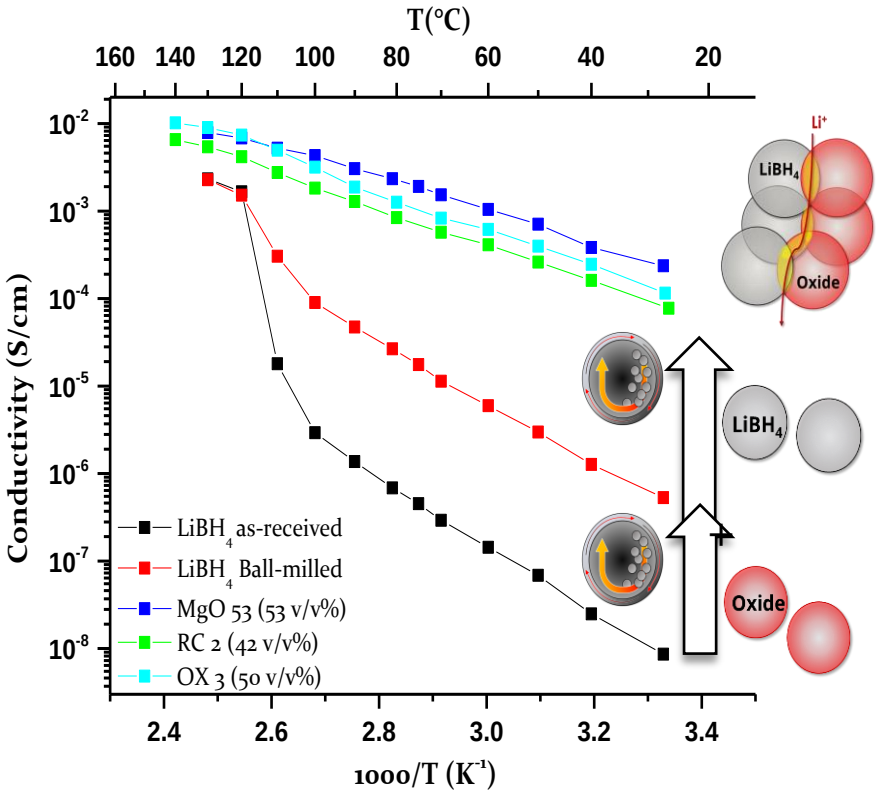

***Figure 18**. Li-ion conductivity of the first heating temperature-dependent EIS cycle of $LiBH_4$ and LiBH4 – oxide composites with the highest conductivity.*

***Table 3.** The activation energy of all solid-state electrolyte samples prepared in this thesis.*

Sample	E_a (eV)
$LiBH_4$	0.78
$LiBH_4$-BM	0.69
MgO 26	0.49
MgO 53	0.43
MgO 74	0.51
RC 1	0.49
RC 2	0.43
RC 3	0.54
RC 4	0.54
RC 5	0.46
RC 6	0.44
OX 1	0.50
OX 2	0.45
OX3	0.44

The E_a was calculated by linearly fitting the data points below 80°C of the Arrhenius plots in **Figure A3 in the appendix** using the activation energy formula: $\boldsymbol{\sigma = \frac{\sigma_0}{T}\, e^{\left(\frac{-Ea}{kb\,T}\right)}}$ (as

described in **chapter 4.2**). The E_a calculated at $LiBH_4$ as-received is determined to be 0.78 eV which is in agreement with the values in literature (0.75 ± 0.07 eV).[60] After ball-milling and adding oxide, it is noticed that all the E_a are decreased. The $LiBH_4$ activation energy after ball-milling is reduced by 0.9 eV, this can be explained by the increase in defects caused by the mechanochemical treatment on the structure. E_a consists of two energy parts, the energy for defect formation and the energy of migration.

After adding the oxides, the E_a decreases by another ~0.2 eV, this behaviour cannot be attributed to the defects formation alone. The reduction in E_a is therefore also attributed to a change in the energy of migration. The energy of migration remains similar in $LiBH_4$ even if there is a phase transition taking place ($LiBH_4$ migration energy of structure Pnma 0.30 eV and P63mc 0.31 eV).[16,61] As previously mentioned, a highly Li-ion conductive interface layer between $LiBH_4$ and the oxide is described in literature. This is considered to be the cause in reduction of the energy of migration within the structure.[55]

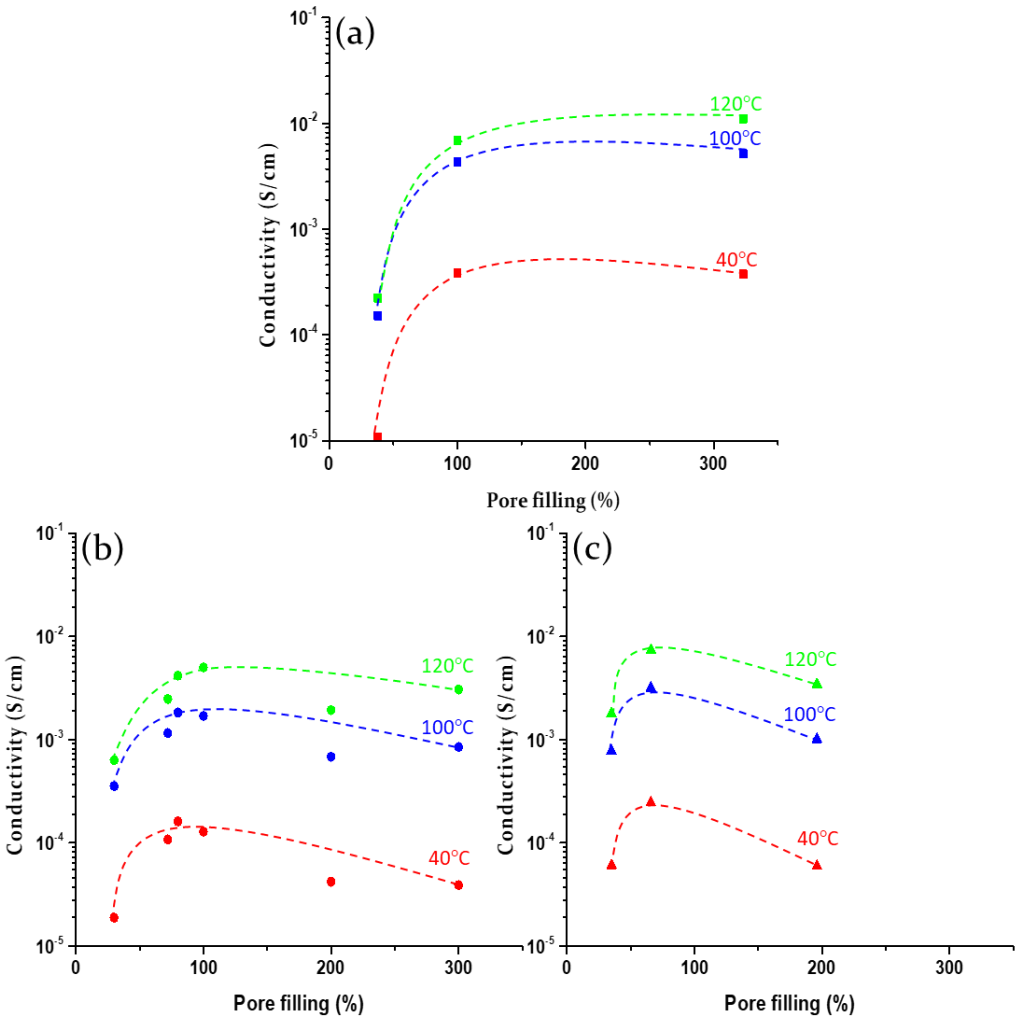

Figure 19. *Li-ion conductivity of (a) $LiBH_4$-MgO, (b) $LiBH_4$- ZrO_2(RC), and (c) $LiBH_4$-ZrO_2 (OX) at 40, 100, and 120 °C as a function of the pore filling. Dashed lines are a guide for the eyes.*

The dependence of pore filling at different temperatures for MgO and ZrO_2 are shown in **Figure 19**. As described in the introduction, it has been described in literature that the right pore filling percentage can give the highest Li-ion conductivity. It is reported that 80% pore filling gives the highest Li-ion conductivity (4.1×10^{-5} S cm^{-1} at 40°C) for composite of $LiBH_4$ - SiO_2.[11] The trend with the highest Li-ion conductivity at a pore filling between 80-100% pore filling is in line with the results found in this thesis. In the case of MgO, it has already been reported in literature that a pore filling of 100% has the highest Li-ion conductivity, and these results are reproduced shown in **Figure 19a**.[24]

Figure 19b shows the $LiBH_4$ - ZrO_2 samples with the RC-100 oxide, here the composite with 80% pore filling shows the highest Li-ion conductivity at low temperatures (RC 2). When the temperature is increased this shifts to the 100% pore filling sample RC 5 (5.89×10^{-5} S cm^{-1} at RT) which has a similar conductivity at RT temperatures as RC 2. This can be explained with the thickness of the $LiBH_4$ fractions. RC 5 contains a 2.9 nm $LiBH_4$ layer, when this layer is above the 2 nm as described before it possesses a $LiBH_4$ bulk fraction. This fraction does not form a highly conductive interface with the oxide and undergoes a phase transition to the hexagonal structure upon heating, contributing to the Li-ion conductivity at higher temperatures. RC 2 has a thickness of 2.3 and thus has less $LiBH_4$ bulk which contributes to the Li-ion conductivity at higher temperatures.

Figure 19c shows $LiBH_4$ - ZrO_2 samples with the DK-1 oxide. The samples with the Dk-1 oxide exhibit higher Li-ion conductivity than the RC-100 oxide. The OX 3 sample shows the highest Li-ion conductivity under the ZrO_2 composites and possesses a pore filling of 66% which is closest to the 80-100% pore filling range compared to the other DK-1 oxide samples (35 and 196 pore filling).

The higher Li-ion conductivity of DK-1 oxide composites compared to the RC-100 can be linked to the lower S_{BET} and V_p (see **Table 1**). Literature describes that the quantity of the grain boundaries will decrease when the total surface area is smaller, the lower quantity of grain boundaries have a positive effect on the Li-ion conductivity.[43,42] The difference in Li-ion conductivity may therefore be due to the fact that RC 2 and OX 3 both possess a $LiBH_4$ thickness of 2.3 nm but OX 3 possesses less grain boundaries effecting the Li-ion conductivity positively.

After showing the highest Li-ion conductivity for the first time with $LiBH_4$- ZrO_2 composites. It is confirmed that the pore filling method can predict the highest Li-ion conductivity for $LiBH_4$ – oxide composites showing the optimal v/v% ratio. The effect of assembly pressure (also called fabrication pressure) also effects the Li-ion conductivity and will therefore be investigated using different v/v% ratios.

Assembly pressure

During all pore filling and assembly pressure experiments, the amount of sample being weight was taken into account. The amount of sample was calculated to obtain a theoretical volume between 30 and 33 mm^3. This was done to compare changes in volume and thickness. The sample holder had a diameter of 10 mm so the maximum achievable assembly pressure during cold pressing was 250 MPa when applying a force of 2 tons. In the XRD data, it was found that no changes could be observed when the mixtures were

cold pressed with the maximum assembly pressure as described earlier (see **Figure A2 of the appendix**).

When increasing assembly pressure is applied to the SSE pellets, two main effects take place. Besides the pellet decreasing in thickness with increasing assembly pressure, a change in Li-ion conductivity was observed by performing EIS measurements at each assembly pressure for all SSE. Examining the formula for calculating Li-ion conductivity ($\sigma = \frac{t}{AR}$), one would expect lower Li-ion conductivity when the thickness decreases and the area remains constant, but in contrast, the Li-ion conductivity increases due to a greater decrease in resistance within the system. **Figure 20** shows the Li-ion conductivity of as-received and ball-milled $LiBH_4$ as a function of the assembly pressure applied to form the pellet. The decrease in thickness of the $LiBH_4$ SSE pellet can be found in **Figure 6A of the appendix**.

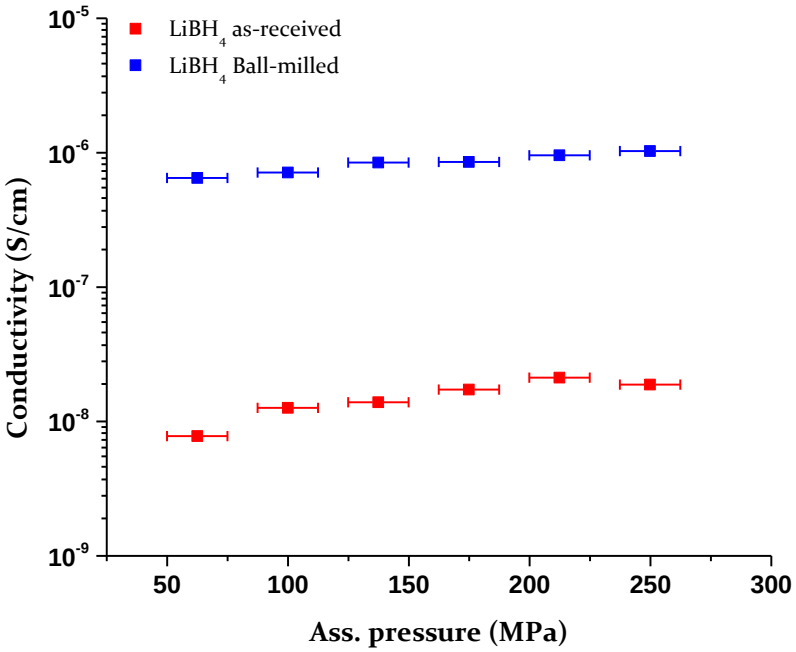

Figure 20. *Li-ion conductivity as a function of the assembly pressure of $LiBH_4$ as-received and ball-milled.*

$LiBH_4$ as-received and ball-milled are shown where the Li-ion conductivity increases with increasing assembly pressure. Both as-received and ball-milled $LiBH_4$ have increased Li-ion conductivity of 244% (7.7×10^{-9} S cm^{-1} with 63 MPa to 1.88×10^{-8} S cm^{-1} with 250 MPa at RT) and 157% (6.49×10^{-7} S cm^{-1} with 63 MPa to 1.02×10^{-6} S cm^{-1} with 250 MPa at RT) respectively. This increase in Li-ion conductivity may have several causes. Reported in literature a possible explanation can be assigned to the densification of the samples, allowing the Li^+ ions to diffuse readily inducing rearrangement of the ions. This rearrangement results in a densification of the structure creating more free volumes, which facilitates ionic diffusion.[62] In other literature it is described that a phase transition of $LiBH_4$ from orthorhombic to hexagonal can take place at high pressures and RT, and

that until a pressure of 1.4 GPa is reached the orthorhombic and hexagonal coexist. The possibility exists that a small fraction of hexagonal $LiBH_4$ is present, resulting in higher Li-ion conductivity within the structure.[45,63] Another factor that could increase the Li-ion conductivity can be linked to the decreasing quantity of grain boundaries and pore volume described earlier. But this effect is mainly associated with oxides where grain boundaries have a great influence on the conductivity.[42,43,62]

Increasing the assembly pressure shows a increasing effect on the conductivity up to 400 MPa for some SSE in literature.[43,62] **Figure 21** shows that this is not the case for a part of the $LiBH_4$ - oxides composites prepared in this study.

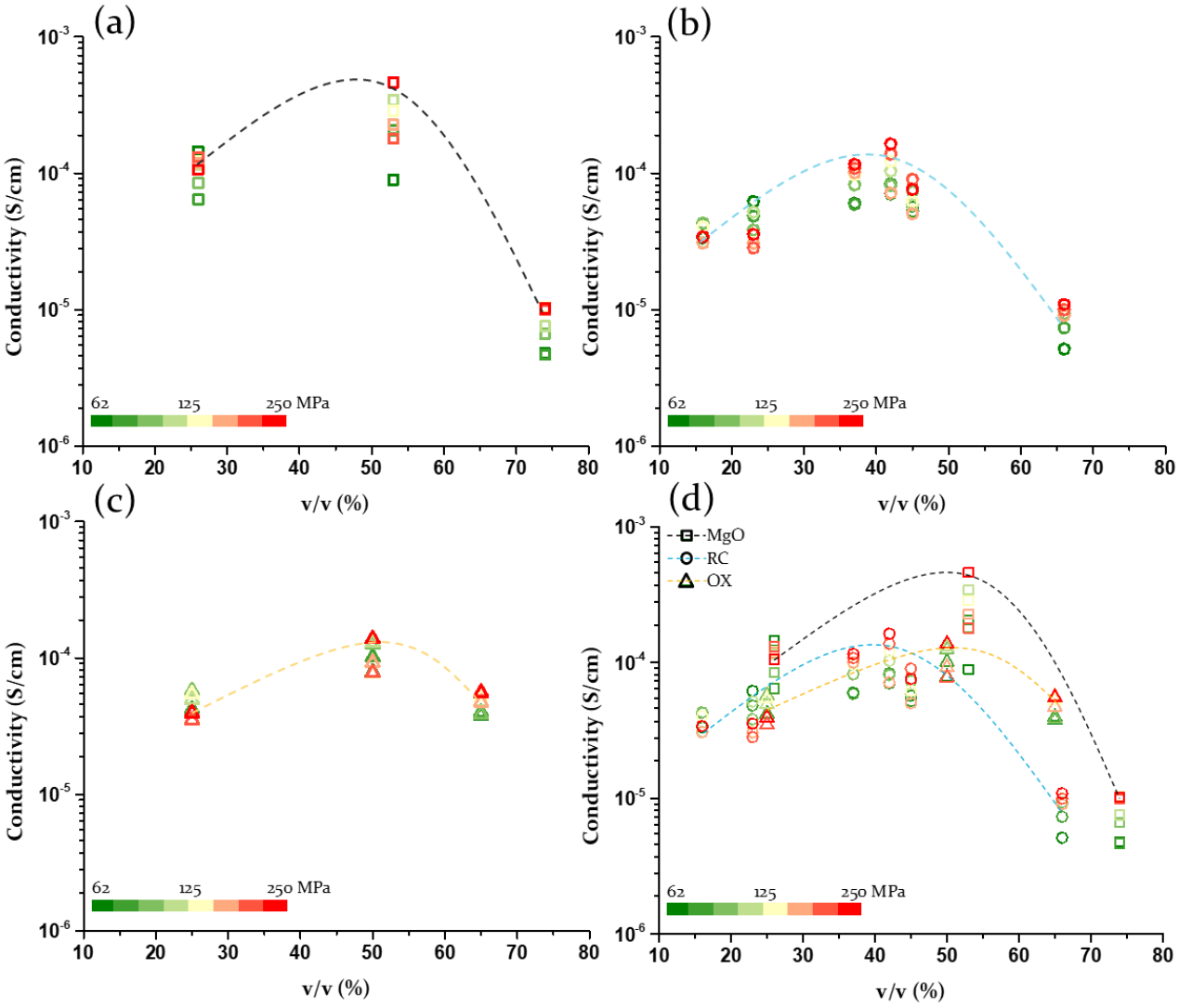

Figure 21. *Li-ion conductivity as a function of oxide volume ratio and assembly pressure of (a) $LiBH_4$ –MgO, (b) $LiBH_4$ – ZRO_2 (RC), (c) $LiBH_4$ – ZrO_2 (OX), and (d) all $LiBH_4$ – oxide composites. Dashed lines are a guide for the eyes.*

The increasing Li-ion conductivity effect caused by increasing assembly pressure seems only to occur at v/v% above 30% for the three different oxides. Below 30%, the increasing

assembly pressure shows no trend for the Li-ion conductivity. Above 30 v/v%, it is observed that the Li-ion conductivity shows an increasing trend from low to high assembly pressures. This trend can be explained by the hardness of the oxides and the amount that is mixed with the $LiBH_4$ to form specific composition and influence the mechanical properties.

The hardness depends on the Bulk modulus (B) representing the resistance to fracture a material and shear modulus (G) represents the resistance of plastic deformation for a material. $LiBH_4$ (B = 52 GPa; G = 44 GPa)[63] exhibits lower B and G values compared to MgO (B = 163 GPa; G = 127 GPa)[64] and ZrO_2 (B = 188 GPa; G = 86 GPa)[65] at RT according to the generalised gradient approximation, making $LiBH_4$ a softer material than the oxides.[63,66]

With the presence of the harder oxides, the mechanical properties of the composites such as hardness end flexibility change. This change makes it more difficult for the $LiBH_4$ to undergo rearrangement and densification which, in the case of $LiBH_4$, may be a consequence of increasing Li-ion conductivities as earlier described. With low quantities of oxide in the composite, the assembly pressure will still cause an increasing effect on the Li-ion conductivity, but not significantly as shown with pure $LiBH_4$. Simultaneously, by increasing the assembly pressure there is loss in pore volume and so surface area from the oxide. The loss in surface area of the oxide decreases the amount of oxide - $LiBH_4$ interface which is highly conductive. Since the oxide is present in low quantities and $LiBH_4$ dominates the volume the decrease in this interface will have a negative influence on the Li-ion conductivity. Due to these two situations occur simultaneously, the random trend of Li-ion conductivity can be described when low oxide quantities below the 30% are present in the composites.[43,44]

However, when the oxide quantity increases, the positive effect of increasing the assembly pressure on the Li-ion conductivity seem to be present. At the higher v/v%, the presence of the oxide is in larger quantities, leaving enough surface area for $LiBH_4$ to form the highly conductive interface. When the assembly pressure increases, $LiBH_4$ is forced to form an interface with the oxide due to the decreases in empty space within the sample (explained below). In addition, the pore volume and grain boundaries of the oxide decreases which can also give additional Li-ion conductivity within the structure.[43,44]

The decreases in thickness (volume) as a function of the assembly pressure for all SSE sample are shown in **Figure A5 till A7 of the appendix**, **Figure 22** shows an example of RC 5 SSE. With the thickness, the real volume (V_r) can be calculated and the weight weighed during sample preparation can be used to calculate the theoretical volume (V_t) of the SSE (see formula **chapter 4.2**). With the theoretical and real Volume, the empty space between the grains can be determined with the following formula: $\%\ \boldsymbol{empty\ space\ in\ SSE} = \left(\frac{V_r}{V_t} * \mathbf{100}\right) - \mathbf{100}$

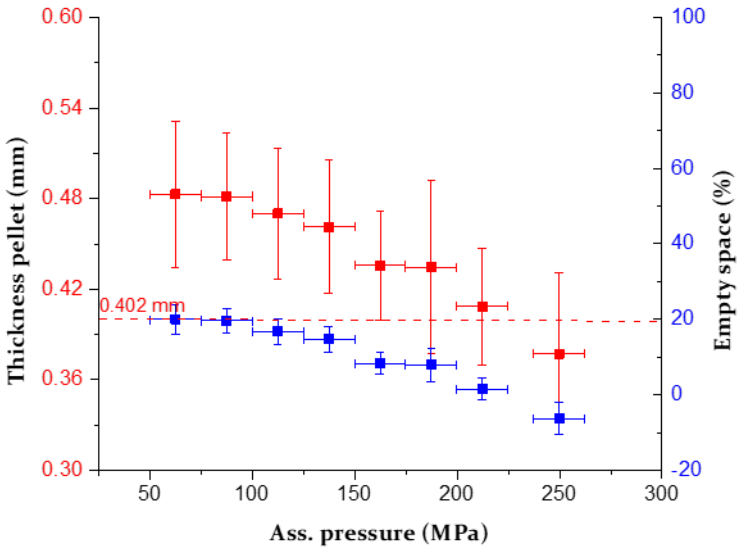

Figure 22 *Thickness and empty space as a function of assembly pressure with RC 5 SSE. dashed line is the theoretical thickness of the SSE pellet.*

The empty space can be translated into the void space between the grains (particles $LiBH_4$ and oxide) in the mixtures. A schematic example is shown in **Figure 23**, which shows that at low pressure, the grains are not yet in complete contact with each other, giving a higher real volume compared to the theoretical volume of the sample. With increasing pressure, eventually the point is reached where there is no more space for the grains ($V_r = V_t$), introducing the principle of bulk modulus. At this point the grains can no longer fill the empty space with increasing pressure but are compressed resulting in the shrinking of the grains.[63–68]

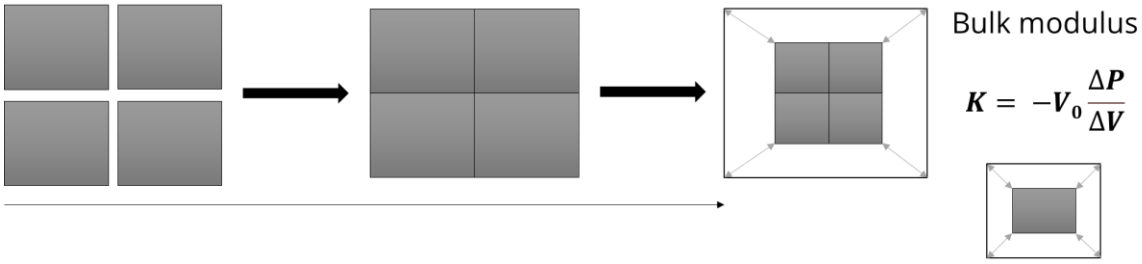

Figure 23. *Schematic illustration of decreasing the empty space with increasing pressure (first two images), followed by the principal of the Bulk modulus of shrinking grains (last images).*

In **Figure 24a**, RC 6 is taken as an example of the correlation between assembly pressure and empty space. The data point that lies closest to 0% empty space with a given assembly pressure is then plotted against the v/v% that the sample exhibits. In **Figure 24b**, this is done for all samples prepared during this study.

The ZrO_2 samples seem to need less pressure to remove the empty space from the sample compared to MgO. A trend is observed where ZrO_2 runs steeper upwards which implies

that the 0% empty space can be achieved at lower assembly pressure. But also that the pressure needed to reach empty space 0% increases increasing the amount of oxide particles.

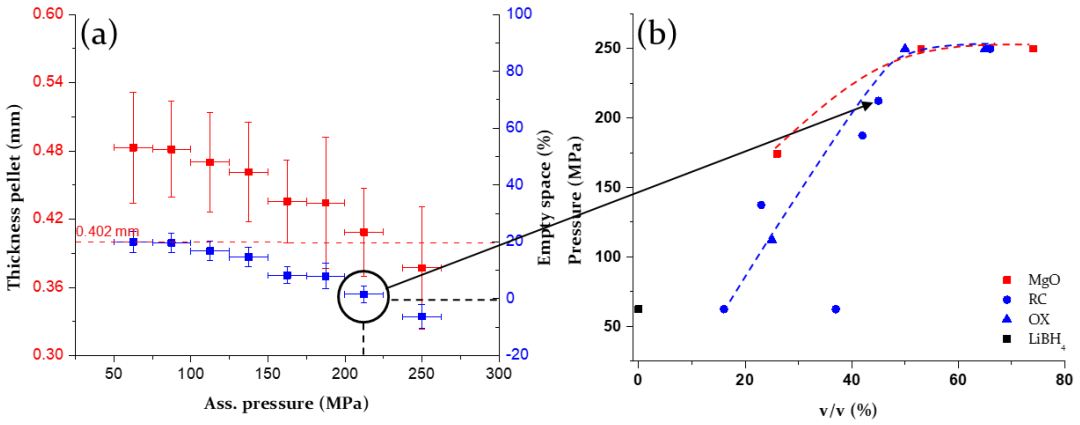

Figure 24. *a) Thickness and empty space as a function of assembly pressure with RC 5 SSE. dashed line is the theoretical thickness of the SSE pellet. b) assembly pressure related to 0% empty space as a function of volume ratio of the oxide. Dashed line is a guide for the eyes.*

Using the Bulk and Shear modulus B/G can be calculated, this values can provide information about the ductility and brittle behaviour of materials. If B/G > 1.75, the material behaves in a ductile manner, when B/G < 1.75 the material behaves in a brittle manner.[63,66] For MgO, B/G gives a value of 1.15 which claims brittle properties and ZrO_2, a B/G value of 2.18 which suggests that the properties are more ductile. The ductile properties of ZrO_2 therefore give more flexibility, which means that less high pressure is needed to remove the empty space and confirming the assumption made before. Using this knowledge, it can be concluded that for ZrO_2 lower assembly pressure is needed to achieve maximum Li-ion conductivity.

The SSE conductive and mechanical properties with addition of oxide and different assembly pressures were studied. Showing that the Li-ion conductivity is increased reaching a maximum when the pore filling is within a range of 80 till 100%. The positive effect on the Li-ion conductivity with increasing assembly pressure has been demonstrated when there are v/v% above 30%. For both MgO and ZrO_2, the samples with pore filling between the range of 80 and 100% possess a v/v% above the 30%. Now that the conductive and mechanical properties of the different SSEs have been optimised, the electrochemical stability can be examined.

5.3 Electrochemical stability

To evaluate the electrochemical stability window of the SSE, cyclic voltammetry measurements at RT were performed on MgO 53 and RC 5 each possessing a pore filling of 100 %, carbon black: GMP-500 was used to increase the signal during the measurement (explained in **chapter 3**). In **Figure 25a**, it is observed that two cathodic peaks (reduction peaks) and one anodic peak (oxidation peak) are present both MgO and ZrO_2 sample during the first cycle. **Gulino et al (2021)**[24], does not describe such an effect when using the same MgO 53. Here it was found that MgO does not affect the electrochemical stability of $LiBH_4$ and the oxidative limit was found at 2.3 V vs. Li^+/Li as described in other literature.[69]

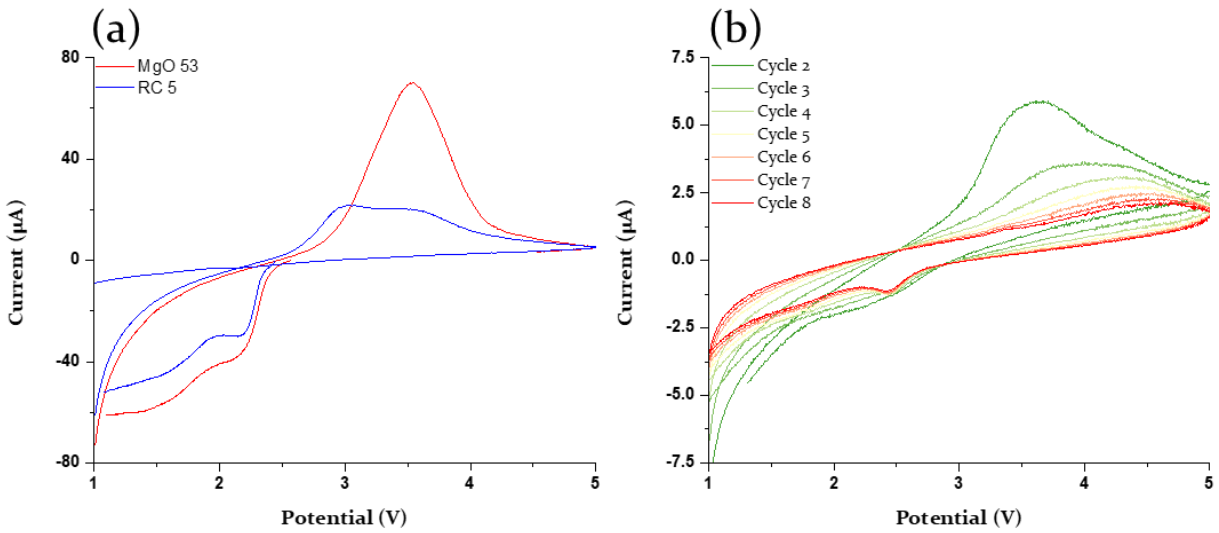

Figure 25. *a) Linear sweep voltammograms of the first cycle with Li | SSE | MgO: GMP-500 | stainless steel cells at scan rates of 100 µV s^{-1} from 1 to 5 V vs. Li^+/Li at RT. b)) Linear sweep voltammograms of cycle 2 till 8 with Li | RC 5 | MgO : GMP-500 | stainless steel cells at scan rates of 100 µV s^{-1} from 1 to 5 V vs. Li^+/Li at RT.*

To ensure that the reduction peaks did not come from the copper or carbon black used in the system, an additional cyclic voltammetry was performed with a different carbon black (KJB-600) was used at the working electrode sides and no copper was used (see **Figure A9 of the appendix** for the cyclic voltammetry). Again, the reduction peaks were observed and indicates that the peaks come from contamination within the system. Literature describes that stainless steel 304 is prone to oxidation when in contact with a salt environment. Especially aggressive species such as Cl^- and H^+ can affect the passivation film and thus introduce corrosion to the surface of the stainless steel. The sample holders is made out of this stainless steel 304, and after use, is quenched in water that has been in contact with different substances that can introduce Cl^- and H^+ ions. The reduction peaks of corroded/oxidised stainless steel 304 have been reported in literature at 1.5 and 2 V vs. Li^+/Li, assigned to the reduction of the air-formed Fe-oxide and/or Cr-oxide and other pitting corrosion products.[70–72] After multiple cycles shown in **Figure 25b** for ZrO_2, the contamination peaks are gone. At this point the oxidative limit was determined at ~2.4 V vs Li^+/Li which is slightly above values of $LiBH_4$ in literature. This suggest that the addition of ZrO_2 slightly effects the electrochemical stability window and

can cause side reactions during galvanostatic cycling, influencing the performance of the system. As described in literature MgO shows no influence on the electrochemical stability.[24,69]

5.4 Stack pressure

Mechanical short-circuit

With the help of stack pressure, chemical compatibility towards lithium metal is evaluated below. The limits of the stack pressure are explored by inducing a mechanical short on different Li| MgO |Li symmetric cell at RT. By increasing the stack pressure and performing EIS measurements in between, the resistance can be monitored at specific stack pressures. When the stack pressure has reached the limit of the system, Li-creep occurs through the SSE causing a short circuit. **Table 4** shows the properties of the SSE with the range where the mechanical short occurred (for the data points see **Figure A9 of the appendix**). For MgO 26 and MgO 53, a 4 mm cell (max. stack pressure 178 MPa) was used to reach higher stack pressures compared to the 10 mm cell (max. stack pressure 25 MPa).

Table 4. *Mechanical induced short-circuit data for MgO samples.*

Sample	Theoretical volume (mm^3)	Pressure range short (MPa)
MgO 26*	6.43	78 – 88
MgO 53*	7.54	111 – 140
MgO 74	25.36	5.3 – 6.4
MgO 74	34.49	8.1 – 10.3

*4mm diameter sample holder used to reach higher stack pressures

The mechanical induced short of MgO 53 was observed between 111-140 MPa and MgO 26 shorts at a range between 78 - 88 MPa stack pressure, both above the maximum stack pressure (25 MPa) of the 10 mm cell used in the galvanostatic stripping and plating study. It is found that increasing the amount of nanoparticles (from 26 to 53 v/v%) in the system. has a positive effect on the mechanical properties of the system.

MgO 74 has a higher oxide content which means it is a harder material, however, the short already occurs at much lower values between 5 and 10 MPa. The cause of the earlier short can be linked to the brittle structure of MgO as described earlier. If the sample consists largely of MgO, the SSE pellet is brittle and can therefore break easily when pressure is applied. The mechanical short and thus the breaking of the system occurs at the same time that the yield strength of MgO is reached (yield strength of MgO is between 6 and 9 MPa).[73] This means that the dominant volume of MgO cannot deform elastically to repair the cracks in the system. These cracks allow the Li to creep through when it exceeds its own yield strength (0.8 MPa)[39], resulting in rapid short-circuiting. This shows that when high v/v% oxides are added to $LiBH_4$ not only the Li-ion conductivity decrease again (compared to lower v/v%), it also reduces the positive effects of the mechanical properties.

The low Li-ion conductivity and poor mechanical properties of MgO 74 give reason to not further study this composite in galvanostatic experiments. The other MgO samples have high Li-ion conductivity and possess the mechanical strength to withstand high stack pressures. Together with RC 5, these three samples are further evaluated on the chemical compatibility with lithium metal using stack pressure.

Contact resistance

Using the same method used for the mechanical induced short experiment, the Li|SSE|Li symmetric cells with MgO 26, MgO 53, and RC 5 were exposed to a stack pressure up to 25 MPa. **Figure 26** shows two samples MgO 26 (**Figure 26a**) and RC 5 (**Figure 26b**) with an example of the contact resistance ($R_c = R_{int}$) gradient when applying increasing stack pressure, R_c is calculated using: $\boldsymbol{R_c} = \frac{R_{total} - R_{SSE}}{2} \boldsymbol{A}$. The R_c indicates the order of contact between the SSE and the lithium metal interface. When contact is lost this will cause the total resistance (R_{total}) of the system to increase, better contact along the interface will result in a decrease in R_{total}. It is assumed that the resistance of the pellet (R_{SSE}) remains the constant.

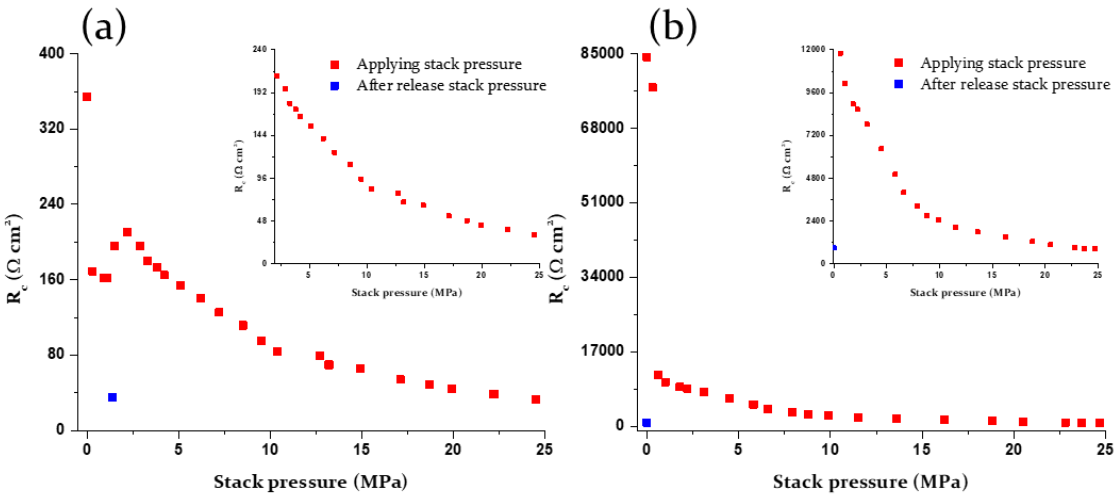

Figure 26. *Contact resistance as a function of stack pressure of (a) Li | MgO 26 | Li, and (b) Li | RC 5 | Li at RT.*

During measurement, it was found that the zero value where no stack pressure is yet applied to the system (0 MPa) is affected in the way the sample holder is closed. For example, MgO 26 gives an R_c of 354 Ω cm² at 0 MPa and RC 5 at 0 MPa has an R_c of 84265 Ω cm². These large differences at the zero value are caused by carefully closing the sample holder, trying to avoid applying a compressive force to the lithium metal and SSE.

When a stack pressure is applied to the system and the pressure reaches or exceeds 0.8 MPa (the yield strength of Li)[39], a significant improvement in contact is observed (see **Figure A10 of the appendix** for other samples). As the stack pressure increases further up to the maximum pressure of 25 MPa, the R_c continues to decrease for both the MgO samples and RC 5. However, it is observed that the samples with MgO achieve a lower R_c compared to the ZrO_2 samples. A possible explanation for the different R_c values can be

identified with the EIS. An example of EIS measurements using different stack pressures for the MgO and ZrO_2 samples are shown in **Figure 27**.

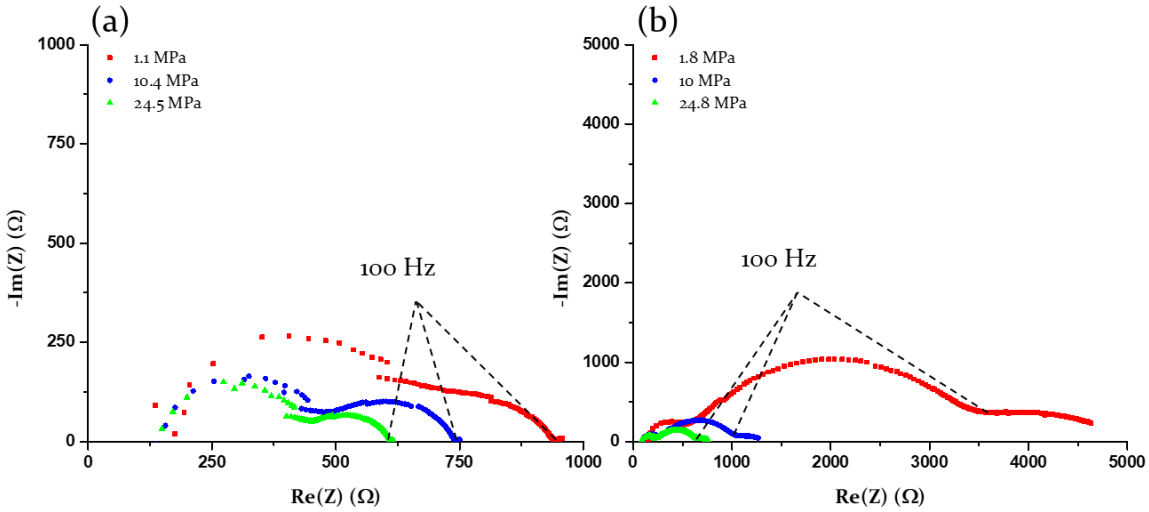

Figure 27. *Impedance spectra shown on the Nyquist plot for (a) Li | MgO 26 | Li and (b) Li | RC 5 | Li at RT under different stack pressures. The dashed line marks the data point obtained at 100 Hz.*

The EIS data shown in **Figure 27a** is related to the MgO 26 and **Figure 27b** is the RC 5 sample. A different Warburg impedance effect in the lower frequency area after 100 Hz was observed from the obtained EIS measurements. Whereas the MgO has a constant slope indicating a semi-infinite diffusion layer trend and showing the data points in a much smaller area after the 100 Hz. The ZrO_2 EIS shows a much large semi-circular trend after the 100 Hz, indicating a limited diffusion layer as shown in **Figure 12** in **chapter 3.4**.

The semi-infinite diffusion layer trend with MgO shows that diffusion in one dimension takes place at the electrodes and thus allows a reversible electrochemical reaction to take place. However, ZrO_2 shows finite diffusion behaviour in the EIS which means that the diffusion is limited. This response can be associated with diffusion through a layer with finite length. This means that mass transport limitations occur between the lithium metal and RC 5 SSE which implies results in more resistance in the system.[47,48,50]

Concluding, It was shown that the contact resistance could be reduced to a minimum value at 25 MPa and that after release of the stack pressure this low R_c is maintained (see **Figure 26** blue data points). The same symmetrical cells with reduced R_c were used in the galvanostatic stripping and plating study.

Galvanostatic stripping and plating

Four experiments are shown below where galvanostatic stripping and plating was performed on different Li|SSE|Li cells: MgO 26 (**Figure 28**), MgO 53 (**Figure 29**), and RC 5 (**Figures 30 and 31**). During stripping and plating, a stack pressure was applied to the system and then held constant for 3600 seconds. Between each stripping and plating sweep, an EIS was measured to observe the R_c at that time. At the same time, the mechanical pressure applied was monitored every second to see if change in pressure affects the stripping/plating process and vice versa. In **Figures 28 to 30**, the stack

pressure was increased each time after 20 stripping and plating cycles (40 hours), with an exception of 1.4 MPa which underwent 32 cycles (64 hours). This was repeated until the symmetrical cell suffered a short-circuit or the maximum stack pressure of 25 MPa was reached. In the experiment in **Figure 31**, the stack pressure was kept constant until a short-circuit was encountered. The stack pressure was chosen at 6 MPa following the data obtained from **Figures 28 to 30**. **Table 5** shows some properties and date of the following measurements.

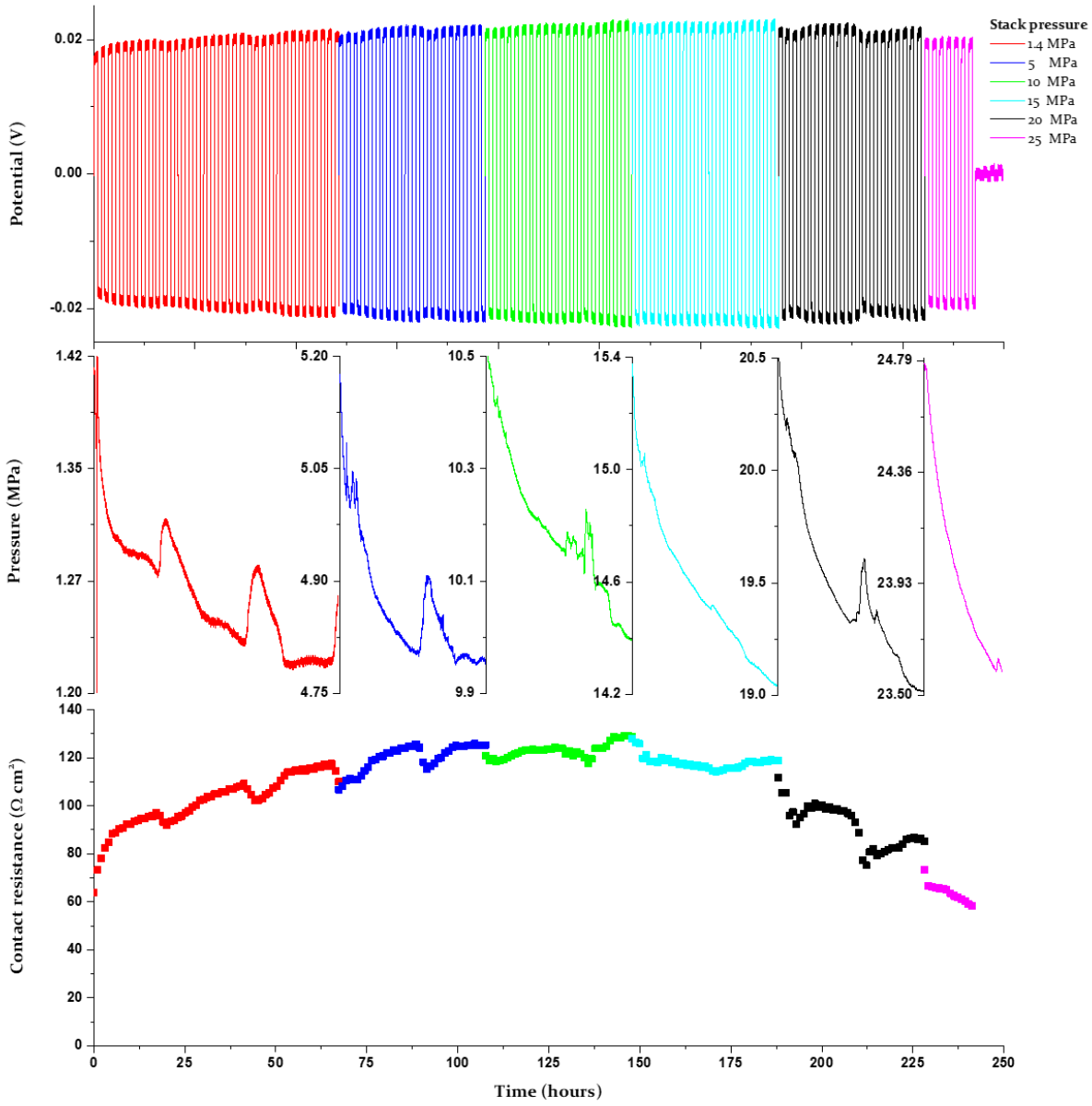

Figure 28. *Galvanostatic cycling profiles of a symmetric Li | MgO 26 | Li cell at RT with a constant current density of 25 μA cm⁻² for 60 min sweeps, applying a stack pressure between the 0 and 25 MPa.*

Galvanic cycling in a Li|MgO26|Li symmetric cell at RT shows reversible lithium stripping and plating at the SSE surface for more than 200 hours under different stack pressures up to 25 MPa. The cell polarization slight increases over this period of time from 17 mV to 20

at a stack pressure of 1.4 MPa. When a stack pressure between 5 and 15 MPa is applied, the cell polarization seems to remain rather stabile in the range of 20 mV. This trend also seems to occur with the R_c, where the R_c increases at 1.4 MPa it seems to be constant between 5 and 15 MPa stack pressure. The cell polarisation seems to become less stable when stack pressures of 20 MPa and higher are applied resulting in a short-circuit during the 25 MPa. During stripping and plating, occasional pressure peaks appear in the pressure monitoring. At the same time, an improvement in contact between the SSE and lithium metal (reduction of the R_c) is observed and a drop / increase in the cell polarisation during positive/negative applied current. This is in agreement with ohm's law (decrease in R gives a decrease in potential with a constate current A). The cause of the pressure peaks remains unclear and are likely caused by void formation and replenishment of the voids. The formation of voids brings a higher volume to the system resulting in increasing pressure, replenishing these voids will lower the volume of the system duo to filling of empty space with lithium resulting in lower pressure.

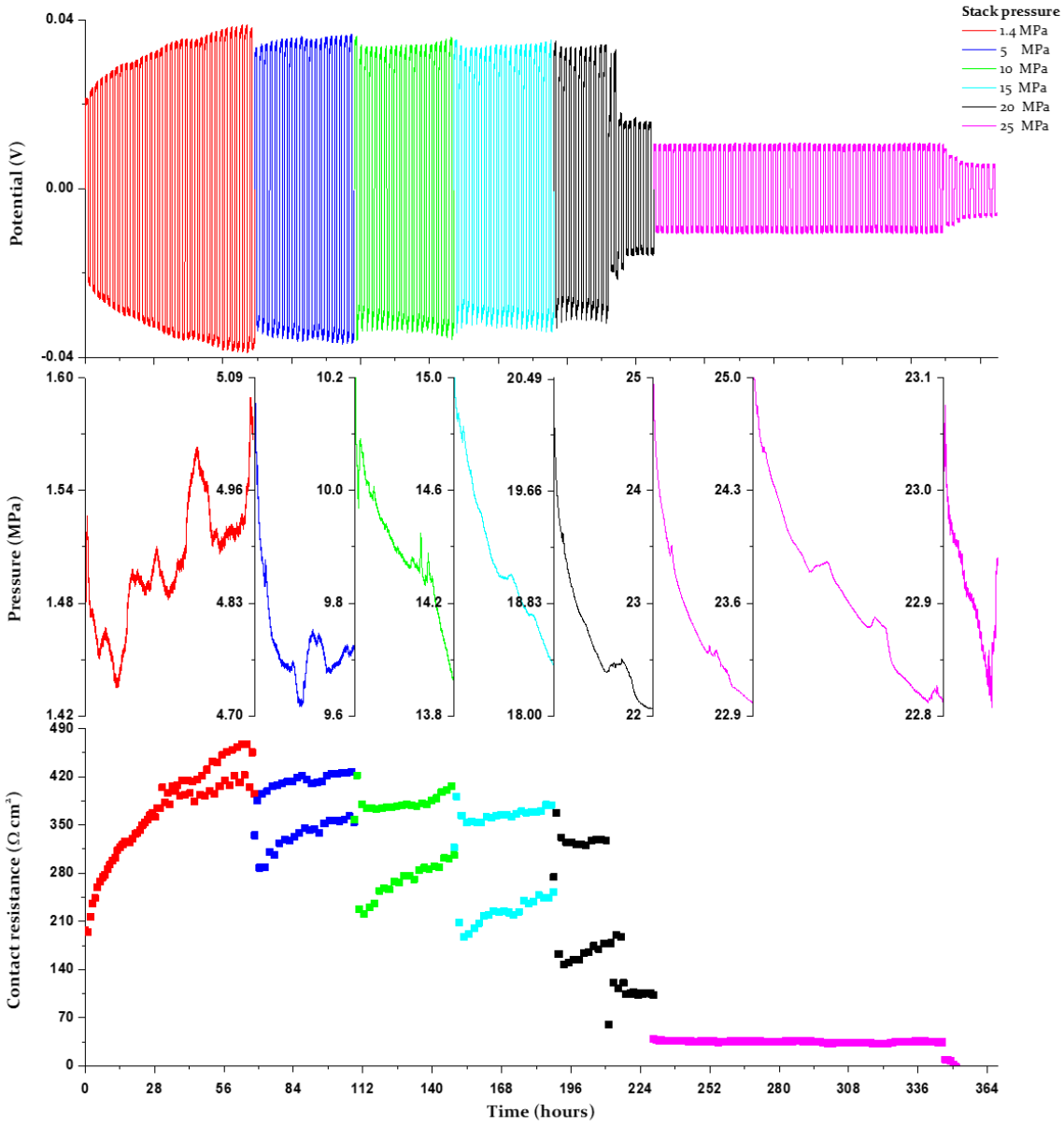

Figure 29. *Galvanostatic cycling profiles of a symmetric Li | MgO 53 | Li cell at RT with a constant current density of 25 μA cm⁻² for 60 min sweeps, applying a stack pressure between the 0 and 25 MPa.*

The Galvanic cycling of Li| MgO 53 |Li symmetric cell at RT shows a widening polarisation within the system during lithium stripping and plating behaviour. During the positive current sweep the potential increases to a higher potential over time (pointy profile). During the negative current sweep the potential starts more negative than at the end of the sweep. This continues for 220 hours until a significant change occurs when applying a stack pressure of 20 MPa. Resulting in a stable lithium stripping and plating profile with a flat potential during the sweep. This stable profile is maintained for 160 hours until a short-circuit appears within the system. Simultaneously, the cell polarisation continuously increases to about 36 mV at 1.4 MPa stack pressure, after which the polarisation decreases when a change in stack pressure takes place and repeats until a stack pressure of 20 MPa was applied. At this point the stable profile was reached and a

stable polarisation of 10 mV is present (**Figure A11 of the appendix** shows the different profiles). The R_c shows a large difference between the positive and negative current sweeps, before the stable profile occurs. At the stack pressure of 5, 10 and 15 MPa the constant trend of R_c was observed only during the positive currents sweeps. During negative current sweeps, the R_c increases at these stack pressures indicating that there is a difference between the two lithium sides of the symmetric cell. This difference in R_c disappears when after 160 hours the stable potential emerges. Which shows that the system recovers during stripping and plating when applying a stack pressure.

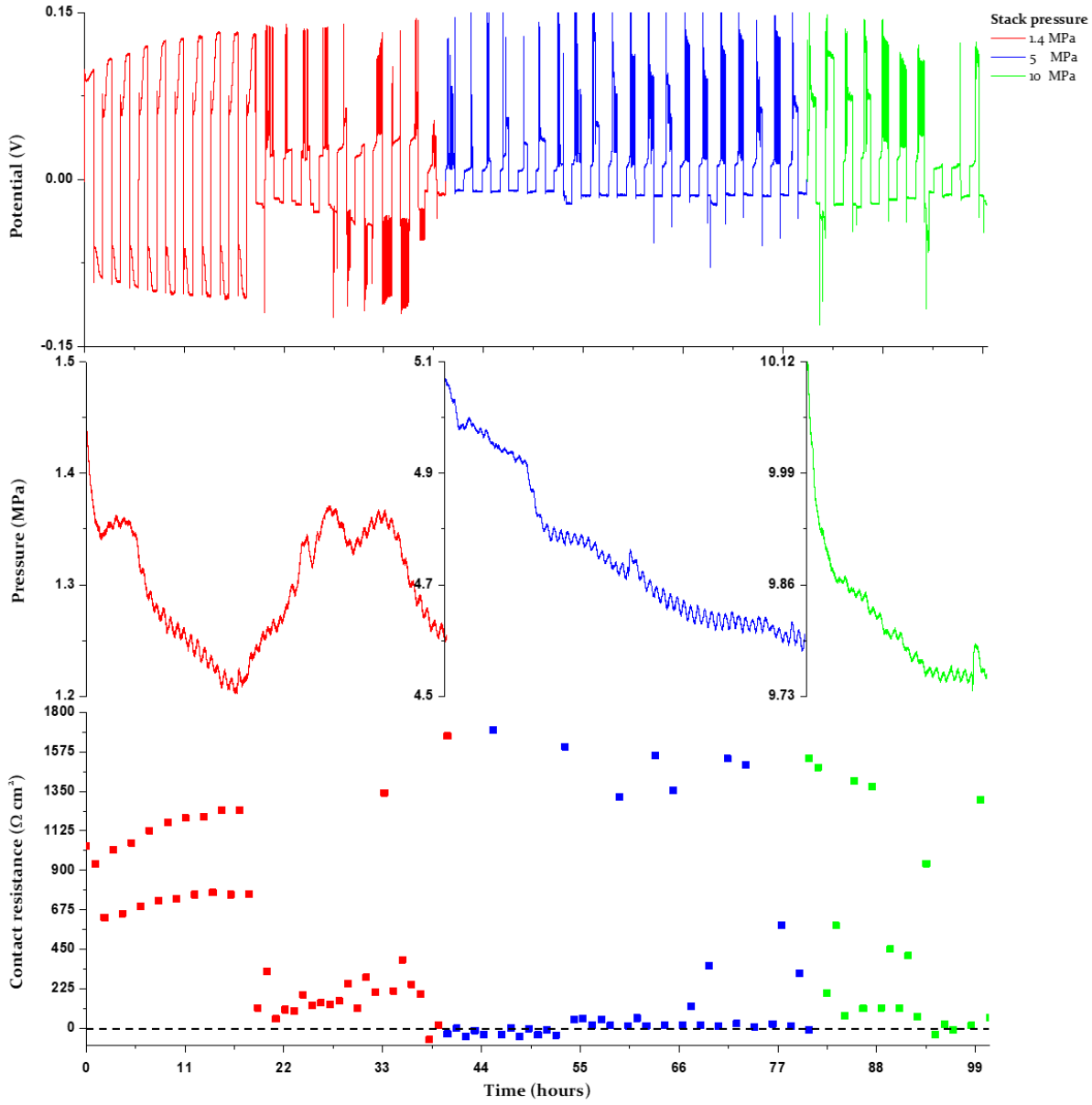

Figure 30. *Galvanostatic cycling profiles of a symmetric Li | RC 5 | Li cell at RT with a constant current density of 25 μA cm⁻² for 60 min sweeps, applying a stack pressure between the 0 and 25 MPa.*

The galvanic cycling of Li| RC 5 |Li shows unstable stripping and plating with polarisation spikes up to 150 mV. The unstable cycling quickly results in a R_c below zero after 5 hours. An R_c below zero indicates that the resistance of the system is lower than the resistance of the SSE pellet obtained before the measurement in contact with the lithium electrodes. The cause of this can be assigned to the penetration of lithium through the SSE causing dendrites penetration. The finite diffusion behaviour of ZrO_2 with the lithium metal previously observed in the contact resistance study could be the cause of the poor polarisation within the system. A stack pressure of 5 MPa does seem to provide more stability. However, Over the whole measurement the pressure profile appeared to be very unstable decreasing and increasing between every sweep. A possible explanation for the

origin of these differences during sweeps could be the diffusion limit. This causes mass-transfer problems resulting in voids and thus expanding the volume of the system increasing and decreasing the pressure in subsequent sweeps.

In general, the three symmetric cells described above show a stable impression at a stack pressure range between 5 and 10 MPa when searching for a constant R_c. Keeping the stack pressure constant at this range may guarantee a constant and improved contact between the SSE and lithium. To evaluate a constant pressure in this range a second Li| RC 5 |Li symmetric cell measurement with a constant stack pressure of 6 MPa was performed.

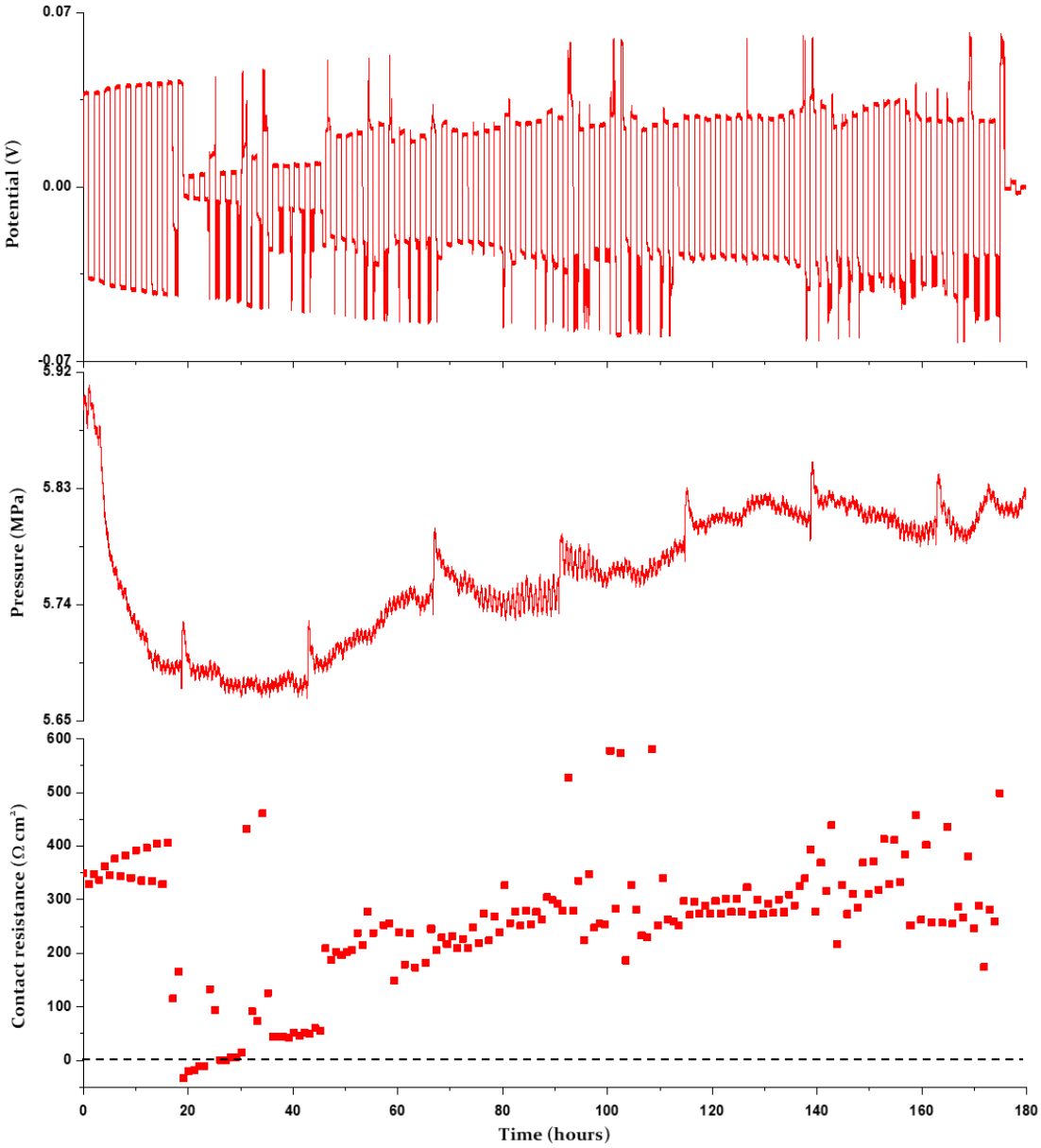

Figure 31. *Galvanostatic cycling profiles of a symmetric Li | RC 5 | Li cell at RT with a constant current density of 25 μA cm⁻² for 60 min sweeps, with a starting stack pressure of 6 MPa.*

The constant stack pressure of 6 MPa shows a more stable polarisation compared to the Li| RC 5 |Li symmetric cell shown in **Figure 30,** still showing spikes in the polarisation. After 20 hours, the R_c drops below zero with the lowest point of the polarisation 5 mV. Subsequently, the R_c gains a positive value and the polarisation shows a broadening increasing trend. Both the polarisation and R_c continue to increase in a constant trend for 175 hours when the short-circuit is detected. During this measurement instable pressure profile after every sweep was observed. This means the ZrO_2 introduces some limitations to the system and needs further investigation in future studies.

***Table 5**. Properties and data of the symmetric cells used in Figure 28 till 31.*

SSE	Volume (mm^3)	Thickness (mm)	Max. stack pressure (MPa)	Polarisation range (mV)	Total duration cycling
MgO 26	36.13 (Vt= 37.97)	0.460	25	18 - 22	241 hours
MgO 53	44.17 (Vt= 43.67)	0.562	25	10 - 36	368 hours
RC 5	24.01 (Vt= 28.44)	0.305	10	11 – 128 (spikes up to 150)	101 hours
RC 5	13.46 (Vt= 26.14)	0.171	Constant pressure 5-6	5 – 43 (spikes up to 60)	175 hours

Galvanostatic cycling with potential limitations

The electrochemical properties of the RC 5 SSE were assessed in an ASSB. TiS2 was used as the cathodic electrode and lithium metal as the anode. The Li-ion conductivities of RC 5 (5. 89 × 10-5 S cm-1 at RT) is high enough to investigate an ASSB cycling at RT by applying a low current.[74] A Li | RC 5 |TiS_2 : RC 5 cell (maximum current density C = 0.611 mAh) using a current of 30.5 µA (C/20) was measured during charging and discharging. The experiment had potential limitation boundaries of 1.5 and 2.6 V. **Figure 32** shows the Galvanostatic Cycling with Potential Limitation of this cell.

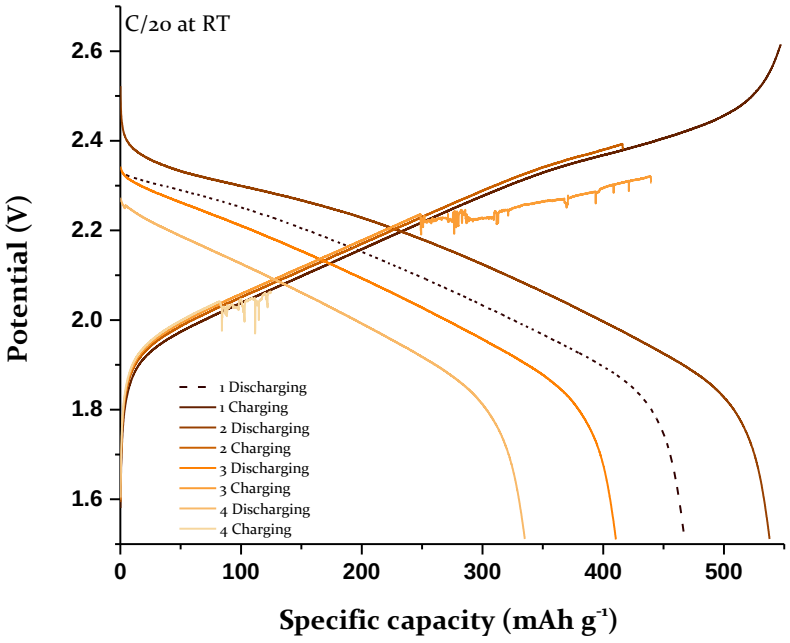

Figure 32. *Voltage profiles of Li | RC 5 | TiS_2: RC 5 cell for a rate of C/20 (30.5 µA) at RT.*

At the second and third charging cycle, the potential limitation was reached switching to the discharge cycle. From here, several spikes can be seen in the charging ramps, resulting in cell failure during cycle four. The maximum charge capacity seems to be reached in cycle two and three at 400 to 450 mAh g^{-1} causing the potential limitation switch. This maximum charge capacity is much lower than the first charging cycle, which is above 540 mAh g^{-1}. What was noticed is that the spikes were not present during discharging, which is also observed in **Gulino et al (2021)**[24]. In this study, measurements were performed using an MgO 53 SSE in an ASSB, with the same TiS_2 cathode (Li | MgO 53 |TiS_2). Here it is suggested that it was inhomogeneous Li-plating caused by the current density exceeding the critical current density, in this case the critical current for plating. As described in the introduction, this critical current for plating can be influenced by the stack pressure. The discharge capacity of the second discharge cycle is 538 mAh g^{-1} which is significantly higher than the first discharging cycle 467 mAh g^{-1}. A similar effect is observed in **Gulino et al (2021)**[24], with a Li | MgO 53 |TiS_2 cell at RT and **Unemoto et al (2015)**[25], with a Li | $LiBH_4$ |TiS_2 cell at 120°C. Here, this effect is linked to a partial

instability of the $LiBH_4$ - TiS_2 interface. This interface causes the formation of H_2 and Li , due to the possible formation of $Li_2B_{12}H_{12}$-based solid electrolyte interface layer. This layer is poor conductive at temperatures below 60°C (lower than 10^{-6} S cm^{-1}), resulting in self-discharging from the battery by self-diffusion of these formed components.

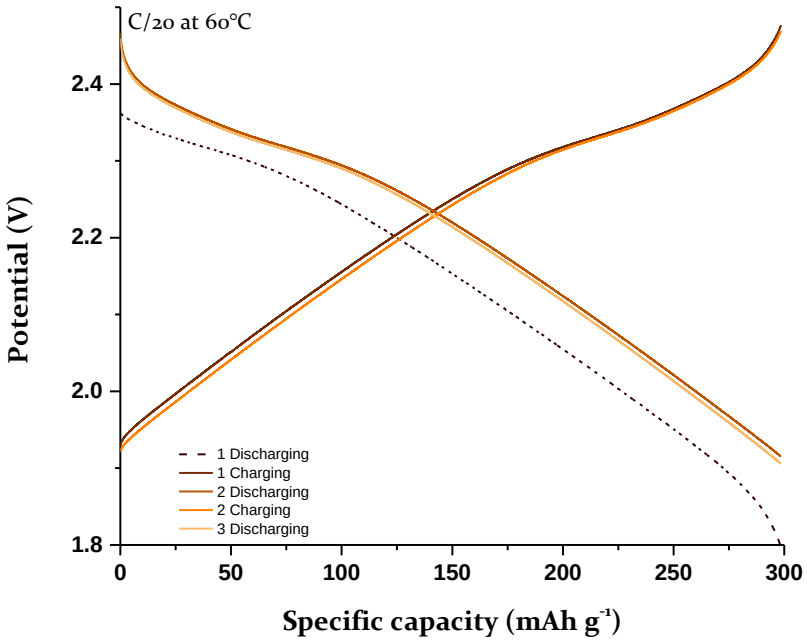

Figure 33. *Voltage profiles of Li* | RC 5 | *TiS_2*: RC 5 *cell for a rate of C/20 (6.09 µA) at 60°C.*

A new Li | RC 5 |TiS_2: RC 5 (maximum current density C = 0.287 mAh) cell under a current density of 6.09 µA at 60°C was cycled to provide insight on the temperature effect on the self-diffusion caused by the $LiBH_4$ - TiS_2 interface. **Figure 33** shows the Galvanostatic Cycling with Potential Limitation of the cell under a temperature of 60°C. Here it can be concluded that the C value was underestimated / miscalculated and therefore the maximum capacity could not be reached during Charging and Discharging. The self-discharge effect was also noticed in this high temperature study. The lower specific capacity during discharge cycle one compared to discharge cycles two was present. The experiment was shut down at the third discharge due to the too low estimated C value. Future experiments should show whether the higher temperature can lead to better kinetics in the cell resulting in a longer cycle life.

6. Conclusion

In this thesis, solid-state electrolytes have been synthetized via mechanochemical treatment of $LiBH_4$ with MgO and ZrO_2. Adding both MgO and ZrO_2 to $LiBH_4$ significantly improved Li-ion conductivity up to five orders of magnitude, due to the formation of a highly conductive interface. The solid-state electrolyte compositions that achieved the most enhanced Li-ion conductivity had an 80 till 100% pore filling of the oxide with $LiBH_4$. Showing that the pore filling model described in literature works for $LiBH_4$ – oxide composites.

The effect of assembly pressure on the Li-ion conductivity performance has been studied. An increased trend of the Li-ion conductivity was observed for $LiBH_4$ when the assembly pressure is increased during cold pressing of the solid-state electrolyte pellet. After adding the oxides, this trend was not seen until an oxide v/v% of 30% or higher was reached.

The composition $LiBH_4$ - MgO (2.3 V vs. Li^+/Li) shows no effect on the electrochemical stability window of $LiBH_4$ and was similar to pure $LiBH_4$ (2.2 V vs. Li^+/Li). The composition $LiBH_4$ - ZrO_2 (2.4 V vs. Li^+/Li). EIS shows a finite diffusion behaviour at low frequencies in ZrO_2 samples with a lithium interface and showed that there was indeed an effect of ZrO_2 on the electrochemical stability compared to MgO not possessing this finite diffusion behaviour.

At room temperature, different stack pressures were applied on symmetrical cells. With this stack pressure, the ranges to introduce a mechanically induced short-circuit were determined of the samples MgO 26 v/v% (78 - 88 MPa), MgO 53 v/v% (111 - 140 MPa), and MgO 76 v/v% (5 - 10 MPa). Here it was shown that mixtures of $LiBH_4$ - MgO can handle high stack pressures, but too high oxide concentrations make the pellet brittle and result in a rapid mechanical short-circuit. With stack pressure, it was also shown that the contact between $LiBH_4$ - oxide and lithium could be significantly improved (example from RC 5 sample: 84265 Ω cm^2 to 840 Ω cm^2 at 25 MPa). By improving the contact in advance, subsequent galvanostatic stripping and plating measurements at room temperature under different stack pressures were performed. This concluded that for the $LiBH_4$ - oxide solid-state electrolytes, a stack pressure between 5 and 10 MPa will result in the longest cycling life for all-solid-state batteries.

At last, it was demonstrated that $LiBH_4$-ZrO_2 were used in an all-solid-state batteries when a low current is applied to the system. Here it was found that self-discharging occurs due to the interaction between $LiBH_4$ and TiS_2 cathode.

In conclusion, complex hydride - oxide compositions can achieve high Li-ion conductivity and are a promising solid-electrolyte for the search in all-solid-state batteries. However, ZrO_2 seems to have an effect on the electrochemical stability of the system and is therefore not recommended. Stack pressure enable improved contact between the lithium and solid-state electrolyte and can keep this interface constant during cycling and may be the solution in longer cycling life in all-solid-state batteries.

7. Outlook

This research has shown that mixing oxides with a complex hydride such as $LiBH_4$ can significantly enhance Li-ion conductivity. Additionally, it can also make the solid-electrolyte harder or more ductile improving the mechanical properties. A suggestion for future research is to search for the optimal Li-ion conductivity within the range of 80 to 100% pore filling with other complex hydrides and oxides exploring all possibilities.

The effect of assembly pressure also appears to have a significant impact on Li-ion conductivity, and further research with assembly pressures above 250 MPa is needed to better understand this trend and find the maximum Li-ion conductivity. However, it should be noted that RVS 304 (material of the sample holder) has a yield strength of 454 to 584 MPa, which means going beyond this pressure will damage the cell.[71]

The effect of stack pressure seems to make a big difference on the contact between the interface of the SSE and lithium metal. However, the method of adding the lithium metal electrodes during the sample preparation creates differences in the symmetry of the cells, and a way must be found to manufacture cells in a similar manner to always obtain the same symmetrical cell. Through many experiments with different constant stack pressures and applied currents, the optimal stack pressure and critical current density can be found for improved cycling-life.

When the cycling life is improved this can also be applied to ASSBs. With the use of stack pressure, cycling of complex hydride ASSBs without high temperatures may be possible. As known, stack pressure has an effect on the anode (lithium metal) indicating that there may also be an effect on the cathode and needs to be studied.

The findings in this thesis provide perspective, but much more needs to be done to bring the energy transition to the next stage with these next-generation ASSBs.

Acknowledgement

First, I would like to thank Dr Valerio Gulino for his friendly guidance during this thesis. I enjoyed the feedback and help I received during our discussions and hope to take it with me in my future career. Henrik Rodeburg I would like to thank for the tools he created for data processing and help provided on the laboratory. I would like to thank the rest of the Battery team for the informal meetings. For making this thesis possible I would like to thank Prof. Dr. Petra De Jongh and Dr. Peter Ngene and providing a great working environment within the MCC group. Finally, I would like to thank all MCC members for the good time and my friends and family for their support during the thesis.

References

1. Armaroli N, Balzani V. The future of energy supply: Challenges and opportunities. *Angew Chemie - Int Ed*. 2007;46(1-2):52-66. doi:10.1002/anie.200602373

2. Global Battery Alliance. A Vision for a Sustainable Battery Value Chain in 2030. 2019;(September):1-52. www.weforum.org

3. Azevedo M, Campagnol N, Hagenbruch T, Hoffman K, Lala A, Ramsbottom O. Lithium and cobalt-a tale of two commodities. *McKinsey&Company Met Min*. 2018;(June):p1-25. https://www.mckinsey.com/~/media/mckinsey/industries/metals and mining/our insights/lithium and cobalt a tale of two commodities/lithium-and-cobalt-a-tale-of-two-commodities.ashx

4. Zubi G, Dufo-López R, Carvalho M, Pasaoglu G. The lithium-ion battery: State of the art and future perspectives. *Renew Sustain Energy Rev*. 2018;89:292-308. doi:10.1016/J.RSER.2018.03.002

5. Goodenough JB, Park KS. The Li-ion rechargeable battery: A perspective. *J Am Chem Soc*. 2013;135(4):1167-1176. doi:10.1021/ja3091438

6. Xu K. Nonaqueous liquid electrolytes for lithium-based rechargeable batteries. *Chem Rev*. 2004;104(10):4303-4417. doi:10.1021/CR030203G/ASSET/CR030203G.FP.PNG_V03

7. Xu W, Wang J, Ding F, et al. Lithium metal anodes for rechargeable batteries. *Energy Environ Sci*. 2014;7(2):513-537. doi:10.1039/c3ee40795k

8. Albertus P, Babinec S, Litzelman S, Newman A. Status and challenges in enabling the lithium metal electrode for high-energy and low-cost rechargeable batteries. *Nat Energy*. 2018;3(1):16-21. doi:10.1038/s41560-017-0047-2

9. Manthiram A, Yu X, Wang S. Lithium battery chemistries enabled by solid-state electrolytes. *Nat Rev Mater*. 2017;2(4):1-16. doi:10.1038/natrevmats.2016.103

10. Duchêne L, Remhof A, Hagemann H, Battaglia C. Status and prospects of hydroborate electrolytes for all-solid-state batteries. *Energy Storage Mater*. 2020;25(August):782-794. doi:10.1016/j.ensm.2019.08.032

11. Gulino V, Barberis L, Ngene P, Baricco M, De Jongh PE. Enhancing Li-Ion Conductivity in LiBH4-Based Solid Electrolytes by Adding Various Nanosized Oxides. *ACS Appl Energy Mater*. 2020;3(5):4941-4948. doi:10.1021/acsaem.9b02268

12. Kim S, Oguchi H, Toyama N, et al. A complex hydride lithium superionic conductor for high-energy-density all-solid-state lithium metal batteries. *Nat Commun 2019 101*. 2019;10(1):1-9. doi:10.1038/s41467-019-09061-9

13. El Kharbachi A, Pinatel E, Nuta I, Baricco M. A thermodynamic assessment of LiBH4. *Calphad Comput Coupling Phase Diagrams Thermochem*. 2012;39:80-90. doi:10.1016/j.calphad.2012.08.005

14. Hazrati E, Brocks G, De Wijs GA. First-principles study of LiBH 4 nanoclusters and their hydrogen storage properties. *J Phys Chem C*. 2012;116(34):18038-18047. doi:10.1021/jp303720v

15. Matsuo M, Nakamori Y, Orimo SI, Maekawa H, Takamura H. Lithium superionic conduction in lithium borohydride accompanied by structural transition. *Appl Phys Lett*. 2007;91(22):5-8. doi:10.1063/1.2817934

16. Ikeshoji T, Tsuchida E, Morishita T, et al. Fast-ionic conductivity of Li+ in LiBH4. *Phys Rev B - Condens Matter Mater Phys*. 2011;83(14):1-5. doi:10.1103/PhysRevB.83.144301

17. Martelli P, Remhof A, Borgschulte A, et al. Rotational motion in LiBH4/LiI solid solutions. *J Phys Chem A*. 2011;115(21):5329-5334. doi:10.1021/jp201372b

18. Matsuo M, Remhof A, Martelli P, et al. Complex Hydrides with (BH 4) – and (NH 2) – Anions as New Lithium Fast-Ion Conductors. *J Am Chem Soc*. 2009;131(45):16389-16391. doi:10.1021/ja907249p

19. Cascallana-Matias I, Keen DA, Cussen EJ, Gregory DH. Phase Behavior in the LiBH4-LiBr System and Structure of the Anion-Stabilized Fast Ionic, High Temperature Phase. *Chem Mater*. 2015;27(22):7780-7787. doi:10.1021/acs.chemmater.5b03642

20. de Kort LM, Gulino V, Blanchard D, Ngene P. Effects of LiBF4 Addition on the Lithium-Ion Conductivity of LiBH4. *Mol 2022, Vol 27, Page 2187*. 2022;27(7):2187. doi:10.3390/MOLECULES27072187

21. Blanchard D, Nale A, Sveinbjörnsson D, et al. Nanoconfined LiBH 4 as a Fast Lithium Ion Conductor. *Adv Funct Mater*. 2015;25(2):184-192. doi:10.1002/adfm.201402538

22. Choi YS, Lee YS, Oh KH, Cho YW. Interface-enhanced Li ion conduction in a LiBH4-SiO2 solid electrolyte. *Phys Chem Chem Phys*. 2016;18(32):22540-22547. doi:10.1039/c6cp03563a

23. Choi YS, Lee YS, Choi DJ, Chae KH, Oh KH, Cho YW. Enhanced Li Ion Conductivity in LiBH4-Al2O3 Mixture via Interface Engineering. *J Phys Chem C*. 2017;121(47):26209-26215. doi:10.1021/acs.jpcc.7b08862

24. Gulino V, Brighi M, Murgia F, et al. Room-Temperature Solid-State Lithium-Ion Battery Using a LiBH4-MgO Composite Electrolyte. *ACS Appl Energy Mater*. 2021;4(2):1228-1236. doi:10.1021/acsaem.0c02525

25. Unemoto A, Ikeshoji T, Yasaku S, et al. Stable Interface Formation between TiS2 and LiBH4 in Bulk-Type All-Solid-State Lithium Batteries. *Chem Mater*. 2015;27(15):5407-5416. doi:10.1021/acs.chemmater.5b02110

26. Unemoto A, Yasaku S, Nogami G, et al. Development of bulk-type all-solid-state lithium-sulfur battery using LiBH4 electrolyte. *Appl Phys Lett*. 2014;105(8). doi:10.1063/1.4893666

27. Krauskopf T, Hartmann H, Zeier WG, Janek J. Toward a Fundamental Understanding of the Lithium Metal Anode in Solid-State Batteries-An Electrochemo-Mechanical Study on the Garnet-Type Solid Electrolyte Li 6.25 Al 0.25 La 3 Zr 2 O 12. *ACS Appl Mater Interfaces*. 2019;11(15):14463-14477. doi:10.1021/ACSAMI.9B02537

28. Spencer Jolly D, Ning Z, Hartley GO, et al. Temperature Dependence of Lithium Anode Voiding in Argyrodite Solid-State Batteries. *ACS Appl Mater Interfaces*. 2021;13(19):22708-22716. doi:10.1021/ACSAMI.1C06706/ASSET/IMAGES/LARGE/AM1C06706_0007.JPEG

29. Jiang FN, Yang SJ, Liu H, et al. Mechanism understanding for stripping electrochemistry of Li metal anode. *SusMat*. 2021;1(4):506-536. doi:10.1002/SUS2.37

30. Kasemchainan J, Zekoll S, Spencer Jolly D, et al. Critical stripping current leads to dendrite formation on plating in lithium anode solid electrolyte cells. *Nat Mater*. 2019;18(10):1105-1111. doi:10.1038/s41563-019-0438-9

31. Yonemoto F, Nishimura A, Motoyama M, Tsuchimine N, Kobayashi S, Iriyama Y. Temperature effects on cycling stability of Li plating/stripping on Ta-doped Li7La3Zr2O12. *J Power Sources*. 2017;343:207-215. doi:10.1016/j.jpowsour.2017.01.009

32. Koerver R, Zhang W, De Biasi L, et al. Chemo-mechanical expansion of lithium electrode materials-on the route to mechanically optimized all-solid-state batteries. *Energy Environ Sci*. 2018;11(8):2142-2158. doi:10.1039/c8ee00907d

33. Wang M, Wolfenstine JB, Sakamoto J. Temperature dependent flux balance of the Li/Li7La3Zr2O12 interface. *Electrochim Acta*. 2019;296:842-847. doi:10.1016/j.electacta.2018.11.034

34. Jow TR, Liang CC. Interface between solid anode and solid electrolyte-effect of pressure on Li/LiI(Al2O3) interface. *Solid State Ionics*. 1983;9-10(PART 1):695-698. doi:10.1016/0167-2738(83)90316-8

35. Sakamoto J. More pressure needed. *Nat Energy*. 2019;4(10):827-828. doi:10.1038/s41560-019-0478-z

36. Wang MJ, Choudhury R, Sakamoto J. Characterizing the Li-Solid-Electrolyte Interface Dynamics as a Function of Stack Pressure and Current Density. *Joule*. 2019;3(9):2165-2178. doi:10.1016/j.joule.2019.06.017

37. Koshikawa H, Matsuda S, Kamiya K, et al. Electrochemical impedance analysis of the Li/Au-Li 7 La 3 Zr 2 O 12 interface during Li dissolution/deposition cycles: Effect of pre-coating Li 7 La 3 Zr 2 O 12 with Au. *J Electroanal Chem*. 2019;835(January):143-149. doi:10.1016/j.jelechem.2019.01.025

38. Lewis JA, Cortes FJQ, Liu Y, et al. Linking void and interphase evolution to electrochemistry in solid-state batteries using operando X-ray tomography. *Nat Mater 2021 204*. 2021;20(4):503-510. doi:10.1038/s41563-020-00903-2

39. Doux JM, Nguyen H, Tan DHS, et al. Stack Pressure Considerations for Room-Temperature All-Solid-State Lithium Metal Batteries. *Adv Energy Mater*. 2020;10(1):1903253. doi:10.1002/aenm.201903253

40. Wang Y, Liu T, Kumar J. Effect of pressure on lithium metal deposition and stripping against sulfide-based solid electrolytes. *ACS Appl Mater Interfaces*. 2020;12(31):34771-34776. doi:10.1021/acsami.0c06201

41. Barai P, Higa K, Srinivasan V. Lithium dendrite growth mechanisms in polymer electrolytes and prevention strategies. *Phys Chem Chem Phys*. 2017;19(31):20493-20505. doi:10.1039/c7cp03304d

42. Doux JM, Yang Y, Tan DHS, et al. Pressure effects on sulfide electrolytes for all solid-state batteries. *J Mater Chem A*. 2020;8(10):5049-5055. doi:10.1039/C9TA12889A

43. Sakuda A, Hayashi A, Tatsumisago M. Sulfide Solid Electrolyte with Favorable Mechanical Property for All-Solid-State Lithium Battery. *Sci Reports 2013 31*. 2013;3(1):1-5. doi:10.1038/srep02261

44. Richards R, Li W, Decker S, et al. Consolidation of Metal Oxide Nanocrystals. Reactive Pellets with Controllable Pore Structure That Represent a New Family of Porous, Inorganic Materials. Published online 2000. doi:10.1021/ja994383g

45. Talyzin A V., Andersson O, Sundqvist B, Kurnosov A, Dubrovinsky L. High-pressure phase transition in LiBH4. *J Solid State Chem*. 2007;180(2):510-517. doi:10.1016/j.jssc.2006.10.032

46. Mal'Tseva NN, Generalova NB, Masanov AY, Zhizhin KY, Kuznetsov NT. Mechanochemical synthesis of complex hydrides. *Russ J Inorg Chem*. 2012;57(13):1631-1652. doi:10.1134/S0036023612130049/METRICS

47. Oldenburger M, Bedürftig B, Gruhle A, et al. Investigation of the low frequency Warburg impedance of Li-ion cells by frequency domain measurements. *J Energy Storage*. 2019;21(November 2018):272-280. doi:10.1016/j.est.2018.11.029

48. Pastor-Fernandez C, Dhammika Widanage W, Marco J, Gama-Valdez MA, Chouchelamane GH. Identification and quantification of ageing mechanisms in Lithium-ion batteries using the EIS technique. *2016 IEEE Transp Electrif Conf Expo, ITEC 2016*. Published online 2016. doi:10.1109/ITEC.2016.7520198

49. Vadhva P, Hu J, Johnson MJ, et al. Electrochemical Impedance Spectroscopy for All-Solid-State Batteries: Theory, Methods and Future Outlook. *ChemElectroChem*. 2021;8(11):1930-1947. doi:10.1002/celc.202100108

50. Rogers JA, Maznev AA, Banet MJ, Nelson KA. Optical Generation and Characterization of Acoustic Waves in Thin Films: Fundamentals and Applications. *Annu Rev Mater Sci*. 2000;30(1):117-157. doi:10.1146/annurev.matsci.30.1.117

51. Elgrishi N, Rountree KJ, McCarthy BD, Rountree ES, Eisenhart TT, Dempsey JL. A Practical Beginner's Guide to Cyclic Voltammetry. *J Chem Educ*. 2018;95(2):197-206. doi:10.1021/acs.jchemed.7b00361

52. Han F, Zhu Y, He X, Mo Y, Wang C. Electrochemical Stability of Li10GeP2S12 and Li7La3Zr2O12 Solid Electrolytes. *Adv Energy Mater*. 2016;6(8):1-9. doi:10.1002/aenm.201501590

53. Xie J, Yang P, Wang Y, Qi T, Lei Y, Li CM. Puzzles and confusions in supercapacitor and battery: Theory and solutions. *J Power Sources*. 2018;401(December 2017):213-223. doi:10.1016/j.jpowsour.2018.08.090

54. Goriparti S, Miele E, De Angelis F, Di Fabrizio E, Proietti Zaccaria R, Capiglia C. Review on recent progress of nanostructured anode materials for Li-ion batteries. *J Power Sources*. 2014;257:421-443. doi:10.1016/J.JPOWSOUR.2013.11.103

55. Lambregts SFH, Van Eck ERH, Suwarno, Ngene P, De Jongh PE, Kentgens APM. Phase Behavior and Ion Dynamics of Nanoconfined LiBH4 in Silica. *J Phys Chem C*. 2019;123(42):25559-25569. doi:10.1021/ACS.JPCC.9B06477/ASSET/IMAGES/LARGE/JP9B06477_0007.JPEG

56. Lefevr J, Cervini L, Griffin JM, Blanchard D. Lithium Conductivity and Ions Dynamics in LiBH4/SiO2 Solid Electrolytes Studied by Solid-State NMR and Quasi-Elastic Neutron Scattering and Applied in Lithium-Sulfur Batteries. *J Phys Chem C*. 2018;122(27):15264-15275. doi:10.1021/acs.jpcc.8b01507

57. Tian W, Deng Z, Wang H, et al. Negative adsorption in the isotherm adsorption experiments of low-adsorption coal and shale. *Nat Gas Ind B*. 2019;6(1):44-50. doi:10.1016/j.ngib.2019.01.006

58. Jong JAW, Guo Y, Veenhoven C, et al. Phenylglyoxaldehyde-Functionalized Polymeric Sorbents for Urea Removal from Aqueous Solutions. *ACS Appl Polym Mater*. 2020;2(2):515-527. doi:10.1021/acsapm.9b00948

59. Brunauer S, Emmett PH, Teller E. Adsorption of Gases in Multimolecular Layers. *J Am Chem Soc*. 1938;60(2):309-319. doi:10.1021/JA01269A023/ASSET/JA01269A023.FP.PNG_V03

60. Gulino V, Wolczyk A, Golov AA, et al. Combined DFT and geometrical–topological analysis of Li-ion conductivity in complex hydrides. *Inorg Chem Front*. 2020;7(17):3115-3125. doi:10.1039/D0QI00577K

61. Lee YS, Cho YW. Fast Lithium Ion Migration in Room Temperature LiBH4. *J Phys Chem C*. 2017;121(33):17773-17779. doi:10.1021/acs.jpcc.7b06328

62. Nose M, Kato A, Sakuda A, Hayashi A, Tatsumisago M. Evaluation of mechanical properties of Na2S-P2S5 sulfide glass electrolytes. *J Mater Chem A*. 2015;3(44):22061-22065. doi:10.1039/c5ta05590c

63. Bouhadda Y, Djellab S, Bououdina M, Fenineche N, Boudouma Y. Structural and elastic properties of LiBH 4 for hydrogen storage applications. *J Alloys Compd*. 2012;534:20-24. doi:10.1016/j.jallcom.2012.04.060

64. Zhao JZ, Lu LY, Chen XR, Bai YL. First-principles calculations for elastic properties of the rocksalt structure MgO. *Phys B Condens Matter*. 2007;387(1-2):245-249. doi:10.1016/j.physb.2006.04.013

65. Zhao XS, Shang SL, Liu ZK, Shen JY. Elastic properties of cubic, tetragonal and monoclinic ZrO2 from first-principles calculations. *J Nucl Mater*. 2011;415(1):13-17. doi:10.1016/J.JNUCMAT.2011.05.016

66. Zhang XD, Hou ZF, Jiang ZY, Hou YQ. Elastic properties of MBH4 (M=Na, K, Rb, Cs). *Phys B Condens Matter*. 2011;406(11):2196-2199. doi:10.1016/j.physb.2011.03.029

67. Gallas MR, Piermarini GJ. Bulk Modulus and Young's Modulus of Nanocrystalline γ-Alumina. *J Am Ceram Soc*. 1994;77(11):2917-2920. doi:10.1111/j.1151-2916.1994.tb04524.x

68. Wang W, Liang Z, Han X, Chen J, Xue C, Zhao H. Mechanical and thermodynamic properties of ZrO2 under high-pressure phase transition: A first-principles study. *J Alloys Compd*. 2015;622:504-512. doi:10.1016/j.jallcom.2014.08.114

69. Asakura R, Duchêne L, Kühnel RS, Remhof A, Hagemann H, Battaglia C. Electrochemical Oxidative Stability of Hydroborate-Based Solid-State Electrolytes. *ACS Appl Energy Mater*. 2019;2(9):6924-6930. doi:10.1021/acsaem.9b01487

70. Deyab MA, Keera ST. Cyclic voltammetric studies of carbon steel corrosion in chloride-formation water solution and effect of some inorganic salts. *Egypt J Pet*. 2012;21(1):31-36. doi:10.1016/J.EJPE.2012.02.005

71. Zhu P, Gastol D, Marshall J, Sommerville R, Goodship V, Kendrick E. A review of current collectors for lithium-ion batteries. *J Power Sources*. 2021;485(November 2020):229321. doi:10.1016/j.jpowsour.2020.229321

72. Lamiri L, Nessark B. Electrochemical behavior, characterization and corrosion protection properties of poly(bithiophene+2-methylfuran) copolymer coatings on A304 stainless steel. *E-Polymers*. 2018;18(2):143-151. doi:10.1515/EPOLY-2017-0057/ASSET/GRAPHIC/J_EPOLY-2017-0057_FIG_008.JPG

73. Chena Y, Feng Z, Zhang W. Effect of MgO content on mechanical properties of directionally solidified pure magnesium. *Mater Res*. 2021;24(2). doi:10.1590/1980-5373-MR-2020-0469

74. Goodenough JB, Kim Y. Challenges for rechargeable Li batteries. *Chem Mater*. 2010;22(3):587-603. doi:10.1021/cm901452z

Appendix

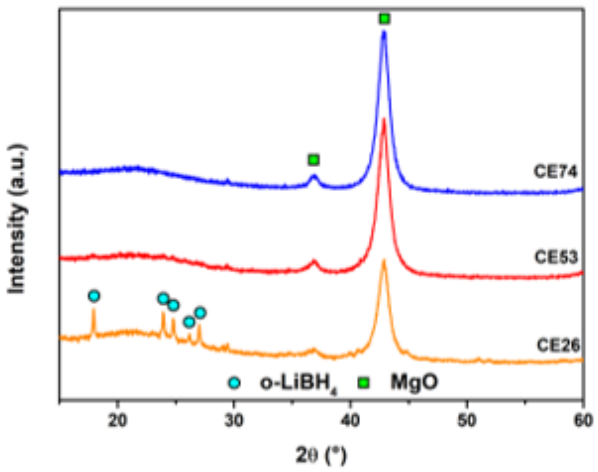

Figure A1. *XRD patterns of different $LiBH_4$- MgO volume fraction composites (In this thesis the same MgO samples from Gulino et al. (2021)[24] are used). Circles: orthorhombic $LiBH_4$, Squares: MgO. Taken from Gulino et al. (2021)[24].*

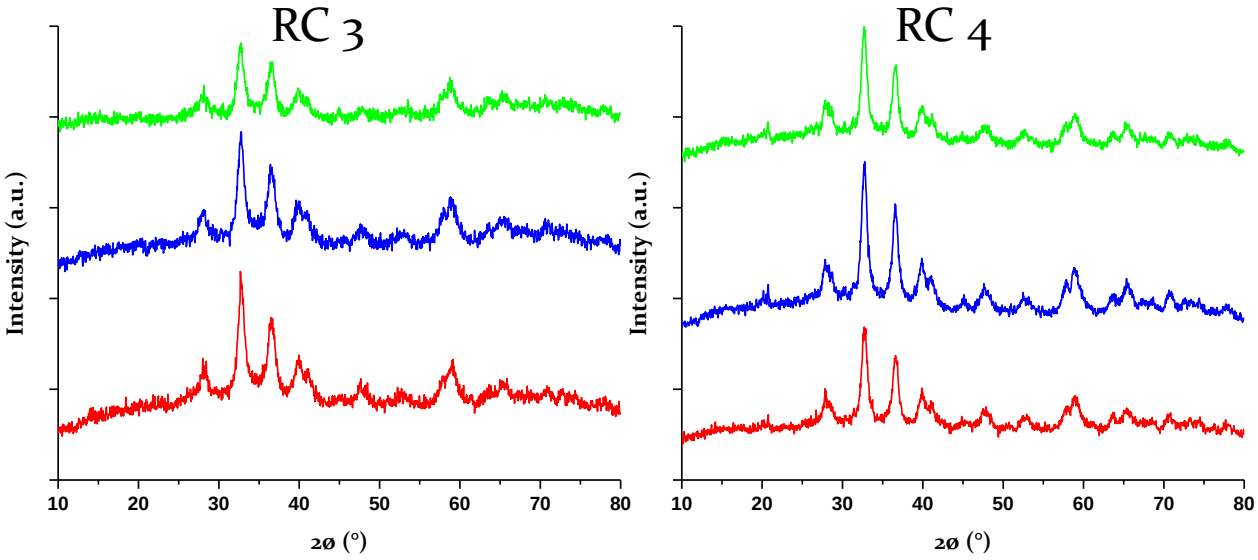

Figure A2*. XRD patterns of $LiBH_4$- ZRO_2 SSE pellet composites with increasing assembly pressure Red 63 MPa, blue 162 MPa, and green 250 MPa .*

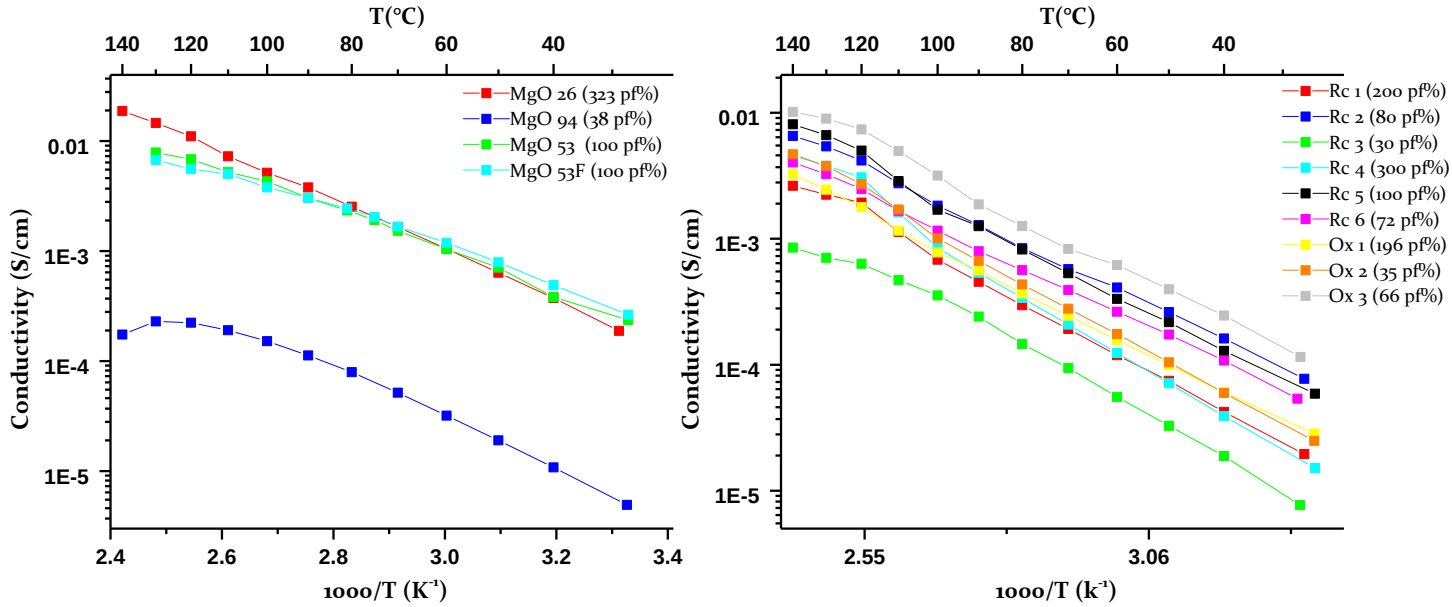

Figure A3. *Li-ion conductivity of the first heating temperature-dependent EIS cycle of all $LiBH_4$ – oxide composites.*

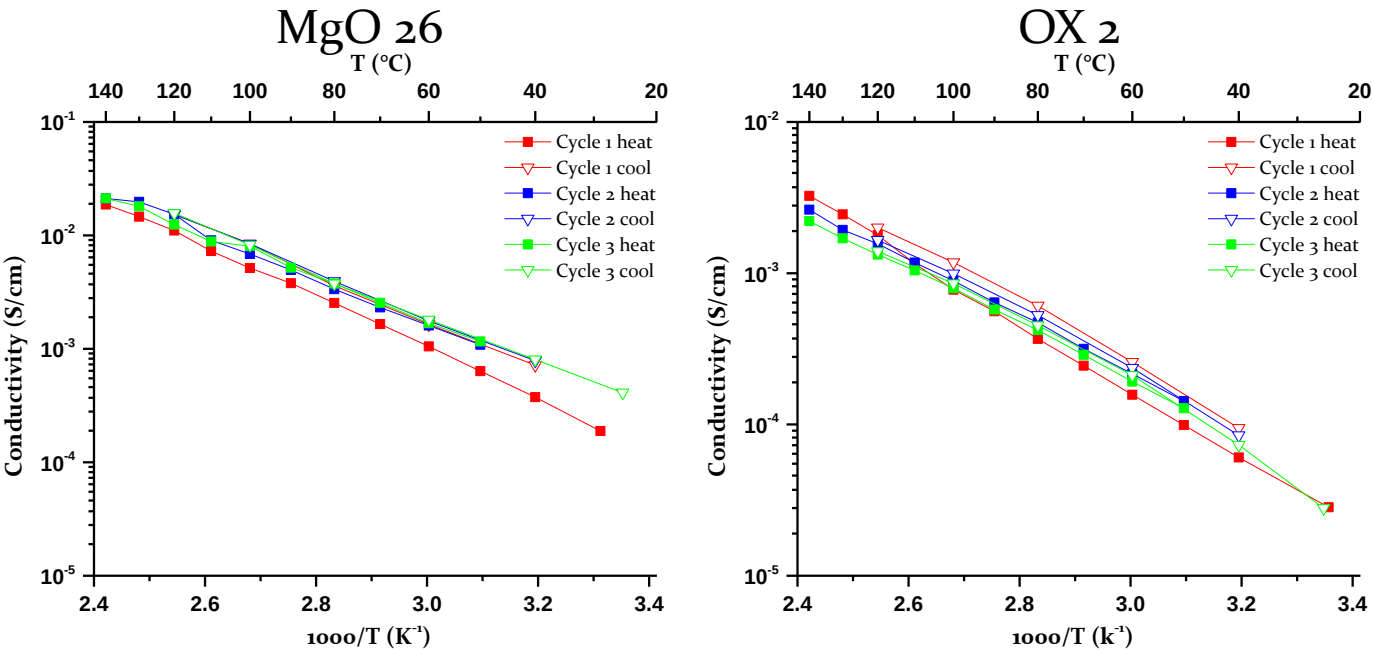

Figure A4. *Li-ion conductivity of the three heating and cooling temperature-dependent EIS cycle of $LiBH_4$ – oxide composites with on the left an MgO sample and right ZrO_2 sample, showing good stability.*

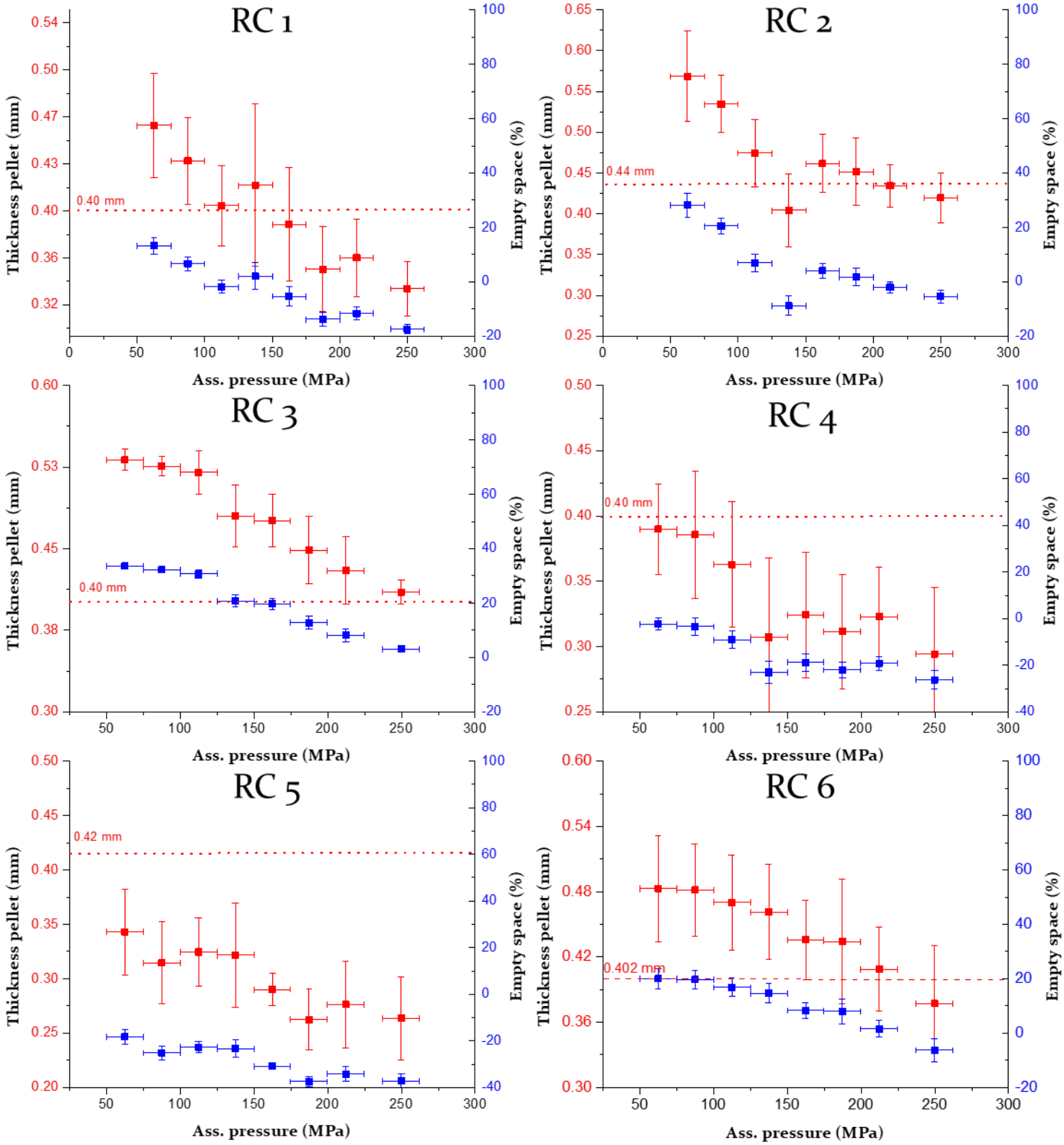

Figure A5. *Thickness and empty space as a function of assembly pressure with of different SSE. The dashed line is the theoretical thickness of the SSE pellet.*

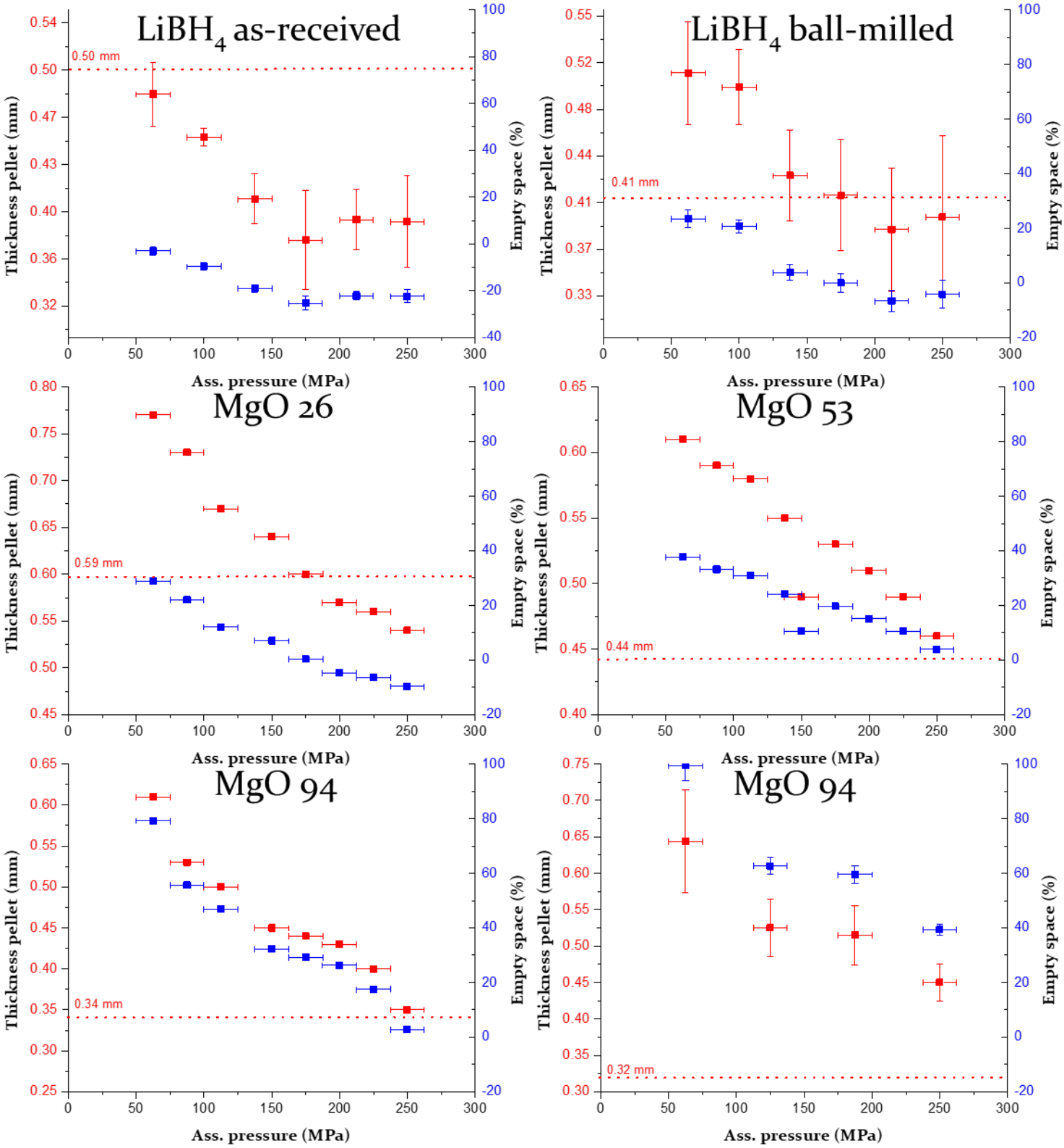

Figure A6. *Thickness and empty space as a function of assembly pressure with of different SSE. The dashed line is the theoretical thickness of the SSE pellet.*

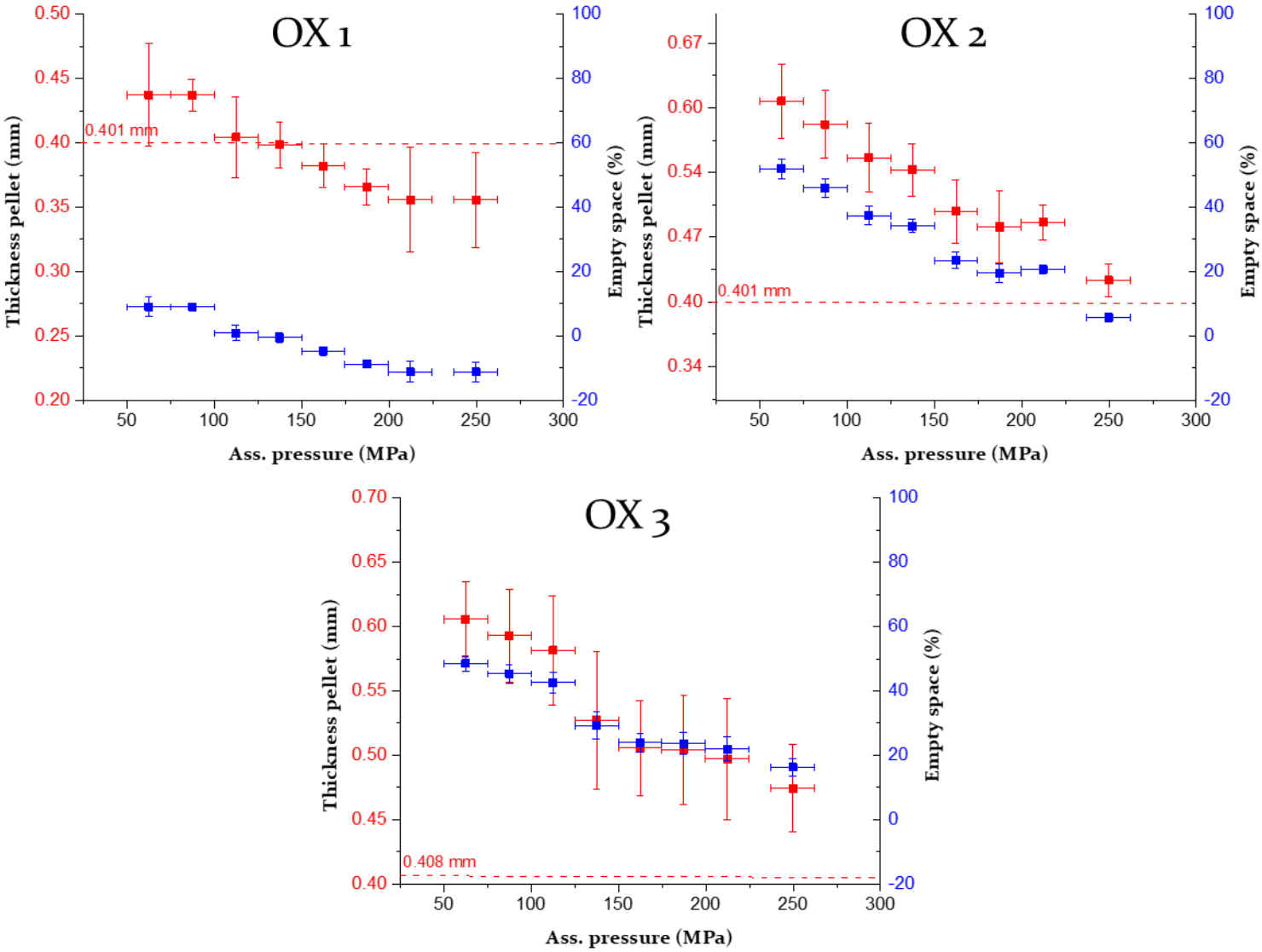

Figure A7. *Thickness and empty space as a function of assembly pressure with of different SSE. The dashed line is the theoretical thickness of the SSE pellet.*

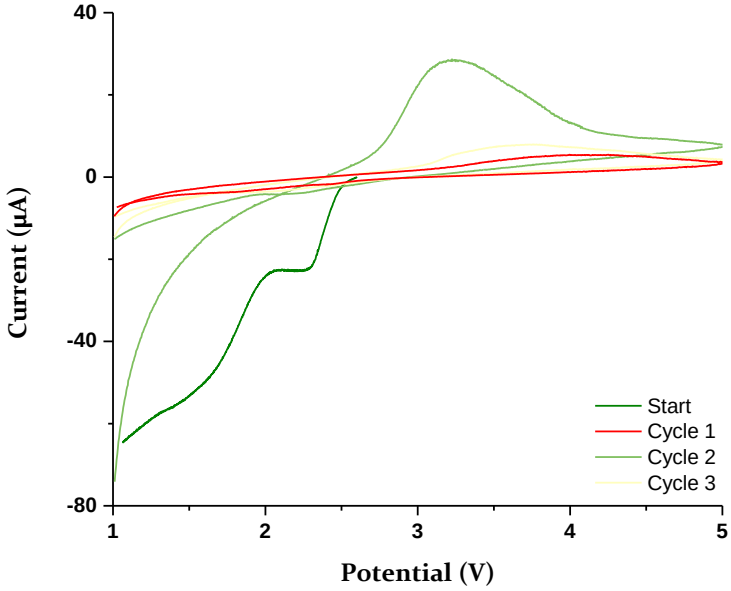

Figure A8. *Linear sweep voltammograms of cycle 2 till 8 with Li (no Cu disk) | RC 5 | MgO : KJB-600 | stainless steel at scan rates of 100 µV s^{-1} from 1 to 5 V vs. Li^+/Li at RT.*

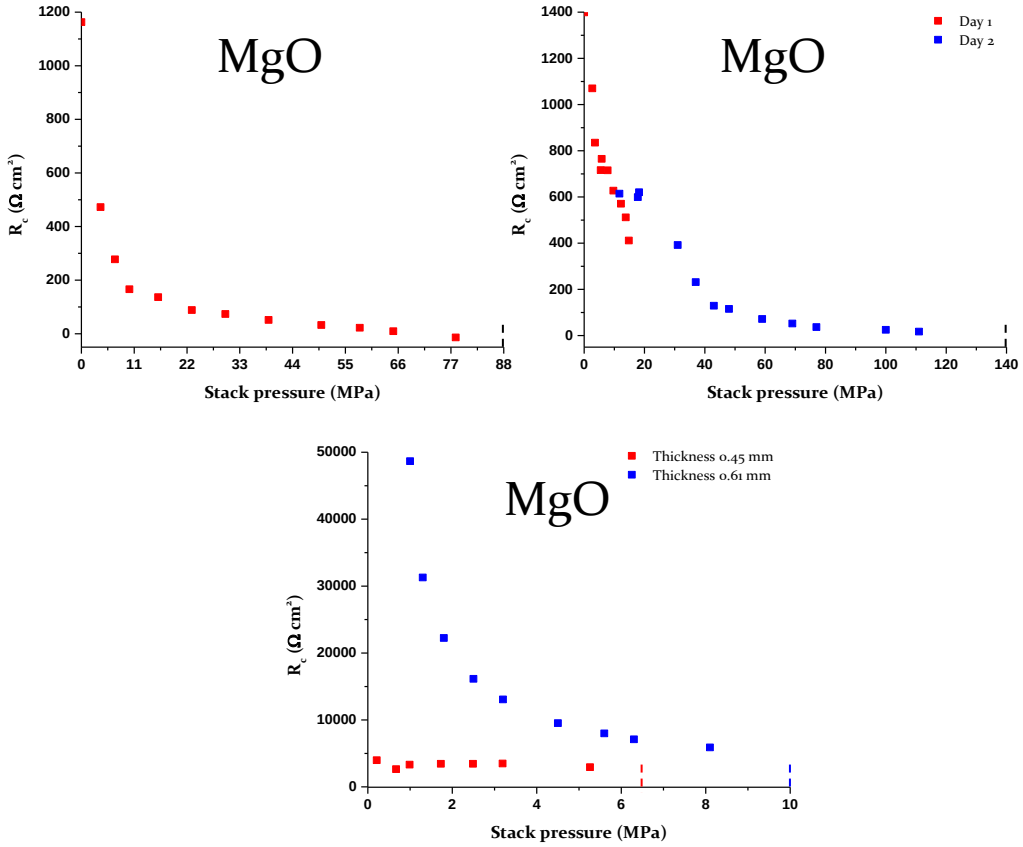

Figure A9. *Contact resistance as a function of stack pressure for Li | SSE | Li at RT. for the mechanical induces short-circuit measurements.*

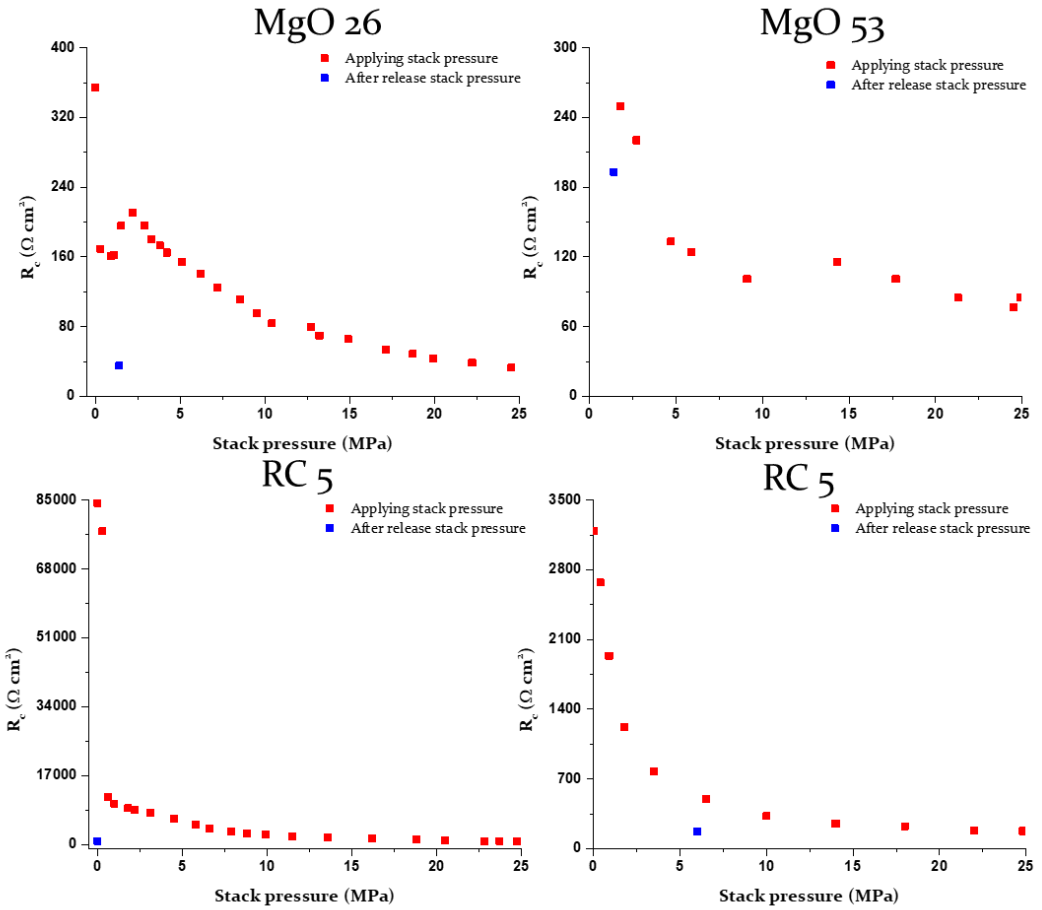

Figure A8. *Contact resistance as a function of stack pressure for Li | SSE | Li at RT.*

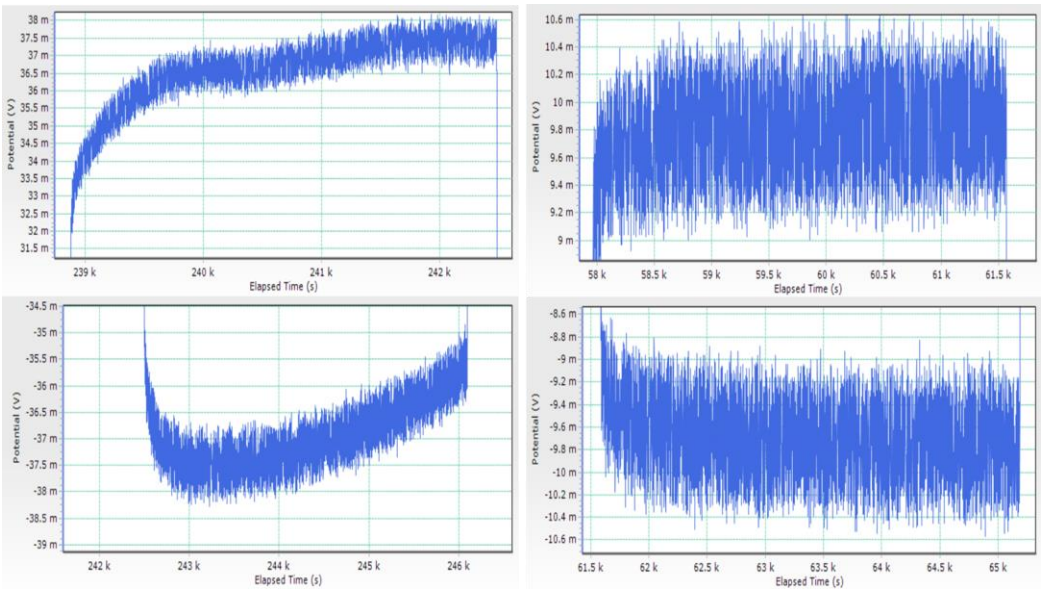

Figure A9. *(top left) Pointy profile positive current, (bottom left) pointy profile negative current,(top right) stable profile positive current, and (bottom right) stable profile negative current. During a galvanostatic cycling profiles of a symmetric Li | SSE | Li cell at RT.*